Remote Sensing Chlorophyll-a in the Strait of Georgia

by

Nicholas M. Komick
BSc, University of Victoria, 2005

A Thesis Submitted in Partial Fulfillment of the
Requirements for the Degree of

Master of Science

in the Department of Geography

Remote Sensing Chlorophyll-a in the Strait of Georgia

by

Nicholas M. Komick
BSc, University of Victoria, 2005

Supervisory Committee

Dr. M. Costa, Supervisor (Department of Geography)

Dr. J. Gower, Member

(Department of Geography, Adjunct)

(Institute of Ocean Sciences, Department of Fisheries and Oceans)

Dr. J. Dower, Member (Department of Biology)

Dr. S. Johannessen, External Member

(Institute of Ocean Sciences, Department of Fisheries and Oceans)

Supervisory Committee

Dr. M. Costa, Supervisor (Department of Geography)

Dr. J. Gower, Member

(Department of Geography, Adjunct)

(Institute of Ocean Sciences, Department of Fisheries and Oceans)

Dr. J. Dower, Member (Department of Biology)

Dr. S. Johannessen, External Member

(Institute of Ocean Sciences, Department of Fisheries and Oceans)

Abstract

The main objective of this thesis was to evaluate the use of Moderate Resolution Imaging Spectroradiometer (MODIS) Aqua imagery to estimate chlorophyll-a (*chl*) concentrations in the surface waters of the Strait of Georgia, located off the southwest coast of Canada. To meet this objective two components were addressed: (1) evaluate *chl* algorithms using ship-based radiometric and biophysical measurements, (2) evaluate atmospheric correction methods in conjunction with *chl* algorithms using MODIS Aqua imagery.

In Chapter 2, biophysical and above-water reflectance measurements collected in 2006 were used to evaluate the OC3M, standard Garver-Siegel-Maritorena version 1 (GSM01), and a modified version of the GSM01 algorithms for estimating *chl* concentrations in the Strait. The Strait was generally classified as a case 2 water body,

transitioning from chromophoric dissolved organic matter (CDOM) dominant in the central region to possibly particulate dominant in the Fraser River plume region. From these biophysical measurements, results showed that the OC3M algorithm was somewhat effective (r^2=0.552) outside the most turbid areas of the Fraser River plume. However, a systematic overestimation of lower *chl* concentrations was found, which may have been related to the higher CDOM absorption observed throughout the Strait. The standard GSM01 algorithm had moderately good agreement with measured CDOM absorption ($r^2 = 0.584$) and total suspended solids (TSS) concentrations ($r^2 = 0.866$), but was ineffective at estimating *chl* concentrations. Localized characterization of the CDOM absorption, through a hyperbolic CDOM model, improved the modified GSM01 results by providing better agreement with measured CDOM absorption ($r^2 = 0.620$) and TSS concentrations ($r^2 = 0.935$). By limiting the GSM01 algorithm to regions with lower combined CDOM and non-algal particulate absorption, the statistical relationship between measured and estimated *chl* improved ($r^2 = 0.690$). The further re-interpretation of phytoplankton absorption from the modified GSM01 algorithm with a two-component phytoplankton model resulted in a *chl* relationship with an $R^2 = 0.702$ and a linear slope closer to one. However, due to the nature of the GSM01 algorithm, its effectiveness is dependent the accurate characterization of the absorption and backscattering of the optically significant water constituents, which is not always available. Furthermore, the GSM01 algorithm effectiveness is contingent upon the accurate atmospheric correction of the shorter blue wavelengths within satellite imagery.

Using unattended fluorometric *chl* measurements, different atmospheric correction approaches in conjunction with the standard OC3M *chl* algorithm and modified GSM01 algorithm from Chapter 2 were evaluated in Chapter 3. Atmospheric correction methods that were evaluated included: the standard near infrared (NIR) correction, a shortwave infrared (SWIR) correction, and an adapted version of the

correction developed at the Management Unit of the North Sea Mathematical Models (MUMM). The NIR correction with the OC3M algorithm was statistically significant with an adjusted $R^2 = 0.759$ outside the most turbid portions of the Strait, but had a relatively large $RMSE$ of 0.523, was limited to $chl < 21$ mg m^{-3}, and only estimated concentrations for 63% of the pixels. Effectiveness of the SWIR correction was limited with the OC3M algorithm because of the low percentage of estimated *chl* concentrations (21% of the pixels) and a lower adjusted $R^2 = 0.572$ outside the more turbid portion of the Strait. The adapted MUMM correction was the most effective, using the spatially averaged aerosol properties from the SWIR correction with the fixed NIR water-reflectance ratio defined by the MUMM method. The MUMM correction with the OC3M algorithm, when limited to pixels outside the Fraser River influence, had an adjusted $R^2 = 0.720$ and provided *chl* estimates for 84% of the pixels. The modified GSM01 algorithm was ineffective with all three atmospheric corrections due to the overcorrection of the 412 nm band. Several possible reasons for this overcorrection were identified, including the presence of absorbing aerosols and absorption from atmospheric NO_2. When comparing spatial-temporal patterns in the MUMM corrected OC3M image with *chl* measurements, general spatial patterns and temporal trends match, with some explainable exceptions. Firstly, turbidity typically found near Fraser River plume makes the OC3M algorithm ineffective. Secondly, under lower aerosol reflectance conditions, the signal-to-noise ratio of the SWIR bands can make the spatial identification of the aerosol properties difficult.

Table of Contents

List of Tables

List of Figures

List of Symbols

Symbol	Name	Units
λ	wavelength	nm
λ_0	reference wavelength	nm
a	absorption coefficient	m^{-1}
A	absorbance	
a^*	specific absorption coefficient	
b	scattering coefficient	m^{-1}
b_b	backscattering coefficient	m^{-1}
$\tilde{b}_b$	scatter:backscattering ratio	
β	volume scattering function	$\mathrm{sr}^{-1}\mathrm{m}^{-1}$
$\tilde{\beta}$	scattering phase function	sr^{-1}
ϖ	single-scatter albedo	
ϖ_a	aerosol single-scatter albedo	
θ_0	solar zenith angle	
θ_v	view zenith angle	
$\Delta\phi$	azimuth difference between solar and view	
ψ	scattering angle	
a_w, a_{NAP}	absorption from water and non-algal particulate, respectively	m^{-1}

Symbol	Name	Units
a_{cdom}, a_{ph}	absorption from CDOM and phytoplankton, respectively	m^{-1}
a_{dg}	combined absorption from CDOM and non-algal particulate	m^{-1}
b_{bw}, b_{bp}	backscatter from water and particulate, respectively	m^{-1}
L	radiance	$\mu W\ cm^{-2} sr^{-1} nm^{-1}$
L_u	upwelling radiance below the air-water interface	$\mu W\ cm^{-2} sr^{-1} nm^{-1}$
L_s	sky radiance	$\mu W\ cm^{-2} sr^{-1} nm^{-1}$
L_t	total water-surface radiance	$\mu W\ cm^{-2} sr^{-1} nm^{-1}$
L_w	water-leaving radiance	$\mu W\ cm^{-2} sr^{-1} nm^{-1}$
L_{wn}	normalized water-leaving radiance	$\mu W\ cm^{-2} sr^{-1} nm^{-1}$
L_{wn}^{ex}	exact normalized water-leaving radiance	$\mu W\ cm^{-2} sr^{-1} nm^{-1}$
E	plane irradiance	$\mu W\ cm^{-2} nm^{-1}$
$E_u,\ E_d$	upwelling, downwelling irradiance below the air-water interface	$\mu W\ cm^{-2} nm^{-1}$
E_s	downwelling sky irradiance	$\mu W\ cm^{-2} nm^{-1}$
R_{rs}	remote sensing reflectance	sr^{-1}
r_{rs}	remote sensing reflectance below the air-water interface	sr^{-1}
ρ	extraterrestrial reflectance	
ρ_t, ρ_r, ρ_w	top-of-atmosphere, Rayleigh, and water extraterrestrial reflectance, respectively	
ρ_{as}	aerosol extraterrestrial reflectance	

Symbol	Name	Units
ρ_{ra}	aerosol-Rayleigh multiple scatterings extraterrestrial reflectance	
ρ_A	combined aerosol and aerosol-Rayleigh multiple scatterings extraterrestrial reflectance	
R	irradiance reflectance	
m	refractive index of water	
$\mathfrak{R}$	air-water interface term	
$\mathfrak{R}_0$	air-water interface term (nadir solar/view angle)	
$t_f, \bar{t}_f$	transmittance from air-to-water and from water-to-air	
$\bar{r}$	reflectance of upwelling water irradiance by air-water interface	
$\bar{F}_0$	extraterrestrial solar irradiance	
$d,\ d_0$	actual, mean earth-sun distance	AU
Q	coefficient relating radiance to upwelling irradiance	sr
Q_0	coefficient relating radiance to upwelling irradiance (nadir solar/view angle)	sr
f'	bio-optical modelling coefficient	
f'_0	bio-optical modelling coefficient (nadir solar/view angle)	
τ	atmospheric optical thickness	
ε	aerosol reflectance ratio	
t	atmospheric diffuse transmittance	
α	fixed water reflectance ratio	

Symbol	Name	Units
γ	atmospheric transmittance ratio	
Chl	chlorophyll-a concentration	mg m^{-3}
ℓ	path length	m
χ^{model}	model estimated biophysical variable	
χ^{true}	measured biophysical variable	
n	number of samples	
S_{cdom}	exponential CDOM absorption slope	nm^{-1}
S_{ph}	exponential two-component phytoplankton slope	
C_1^m	chlorophyll-a maximum for background phytoplankton population	mg m^{-3}
$RMSE$	root mean squared error	
RPD	relative percent difference	
AD	absolute difference	

Acknowledgements

There are several people I need to thank for their assistance, without whom I would not have survived. The first person I would like to thank is my supervisor, Maycira Costa, for giving me the opportunity to undertake this research and her patience, feedback, and encouragement. Maycira provided considerable encouragement and time to clarify the structure and communication of this thesis. I would hate to know how this thesis would sound without her guidance. I would also like to thank Jim Gower for his feedback on Chapter 2, without which the results would not be as complete.

I also thank the various members of the Spectral Lab, including Eduardo Loos and Jennifer O'Neill for their participation in the ship sampling, and Thiago Silva for reviewing components of this thesis. Their overall presence in the lab has definitely made the writing process easier. Thank you, also, to Ricardo Rossin, for assistance with HPLC method development and pigment sample processing and to Sophia Johannessen for assistance with CDOM absorption methods.

For the ferry based measurements, I would like to thank Mark Halverson and the STRATOGEM project for all the hard work in maintaining the instrument and freely providing such a valuable data source.

Thank to my family and friends. Without my parents' encouragement, I would never have persuade such an undertaking. I would also like to thank my wife, Ann, who has been an abundant source of patience and encouragement. I don't know if I would have persevered without her. Finally, I would like to thank Renée Elliott for providing perspective and a constant source of amusement.

Funding for this research was provided by NSERC from an Individual Discov-

ery Grant and ship-time grant to Maycira Costa. Field and lab equipment funding was provided by the Canadian Foundation for Innovation and the British Columbia Knowledge Development Fund.

Chapter 1

Introduction

Since 1978 with the Coastal Zone Color Scanner, a number of satellites capture ocean-colour imagery at various spatial and temporal scales (IOCCG 2007) providing information difficult to attain with ship-based measurements. This information is currently being used in a number of applications including understanding how physical processes influence bio-optical processes (Sathyendranath and Platt 2007), estimation of light penetration into the water column (Lee et al. 2005), and primary productivity (Behrenfeld and Falkowski 1997).

Specifically, oceanographic remote sensing has historically estimated chlorophyll-a (chl) concentrations in open ocean waters where it is the dominant optical variable (Gordon and Morel 1983). However, with the advent of improved ocean-colour satellite sensors, such as the Moderate Resolution Imaging Spectroradiometer (MODIS) and Medium Resolution Imaging Spectrometer (MERIS) instruments, and the increased sophistication of bio-optical algorithms, research has moved from the open-waters to the more optically complex waters in coastal environments (Gordon and Morel 1983, IOCCG 2000).

Coastal zones, defined as 200 m above and 200 m below mean sea level, are an important resource with 60% of the human population living and 90% of world fish caught in these zones (Pernetta and Milliman 1995). With this substantial an-

thropogenic influence, there is a growing need to monitor coastal zones and their associated turbidity (Li et al. 2003b, Hu et al. 2004, Warrick et al. 2004), dissolved organic matter (Doxaran et al. 2005, Kowalczuk et al. 2005, Siegel et al. 2005, Coble 2007), harmful algal blooms (Stumpf 2001, Gower et al. 2005), and primary productivity (Muller-Karger et al. 2005). Primary productivity and its proxy, chlorophyll-a concentration, is a particularly important biophysical variable in the marine food web and consequently for higher trophic levels, such as economically important fisheries. A better understanding of natural variability in primary productivity and how it is influenced by anthropogenic forces and climatic events, such as El Niño and the Pacific Decadal Oscillation, may be achieved through larger spatial and temporal scale measurements of dynamic coastal waters.

As identified in biological oceanographic studies of the Strait of Georgia (Harrison et al. 1983, Li et al. 2000), located off the southwest coast of British Columbia, the larger spatial and longer temporal scales of satellite imagery may provide an additional data source to ship-based measurements for studying primary productivity dynamics in these waters. According to the above authors, only with a higher degree of sampling can the interdependencies between physical and biological processes be better understood.

The general objective of this research was to evaluate remote-sensing techniques to estimate chlorophyll-a (*chl*) concentrations in the Strait of Georgia. To meet this objective, two components were addressed. Firstly, several *chl* algorithms and bio-optical models were evaluated using spectral ship-based measurements modified to MODIS bands, as covered in Chapter 2. Secondly, several atmospheric correction methods were evaluated for estimating *chl* concentrations from MODIS imagery, which is covered in Chapter 3. Chapter 4 summarizes the findings and presents the conclusions of this research. The remainder of this chapter provides a review of the biological and physical processes in the Strait (Section 1.1), theoretical background

for oceanographic remote sensing (Section 1.2), and the optical properties of water column constituents (Section 1.4).

1.1 Strait of Georgia

The Strait of Georgia is a large estuary-like coastal basin between the mainland of British Columbia and Vancouver Island. Several tributaries, bays, inlets, and sounds are connected to the Strait, with tributaries providing both freshwater and sediment. The largest source of these inputs is the Fraser River, which introduces 73 % of the freshwater and 64 % of the particles into the Strait (Johannessen et al. 2003). Pacific Ocean tidal activity also influences the Strait, resulting in a mainly semi-diurnal tide with approximately 4 m of range (LeBlond 1983).

Connectivity to the Pacific Ocean is provided through Johnstone Strait at the north end and through Haro and Juan de Fuca Strait at the south end (Fig. 1.1). Based on calculations by Li et al. (2000), the Strait of Georgia is the most productive of these water bodies, with an annual primary productivity of 377 g C m^{-2} $year^{-1}$, with Juan de Fuca Strait producing 303 g C m^{-2} $year^{-1}$, and Haro Strait producing 238 g C m^{-2} $year^{-1}$. The average productivity of these three straits is higher than the open North Pacific Ocean, which has primary productivity generally varying from 60 to 100 g C m^{-2} $year^{-1}$ (Harrison et al. 1983). A more detailed discussion on the Strait's biology is provided in Section 1.1.2.

An important component to primary productivity in the Strait of Georgia is the influx of intermediate and deep water from the Pacific Ocean into the Strait, which is generally colder and nutrient rich (Masson 2006). This deep-water renewal from the Juan de Fuca Strait shelf is mixed with surface waters in the strong tidal currents through passages around Haro Strait and introduced as a subsurface intrusion into the Strait. This subsurface renewal is strongest in summer, when the Fraser River discharge is highest and estuary circulation is strongest. Similarly, a possible interme-

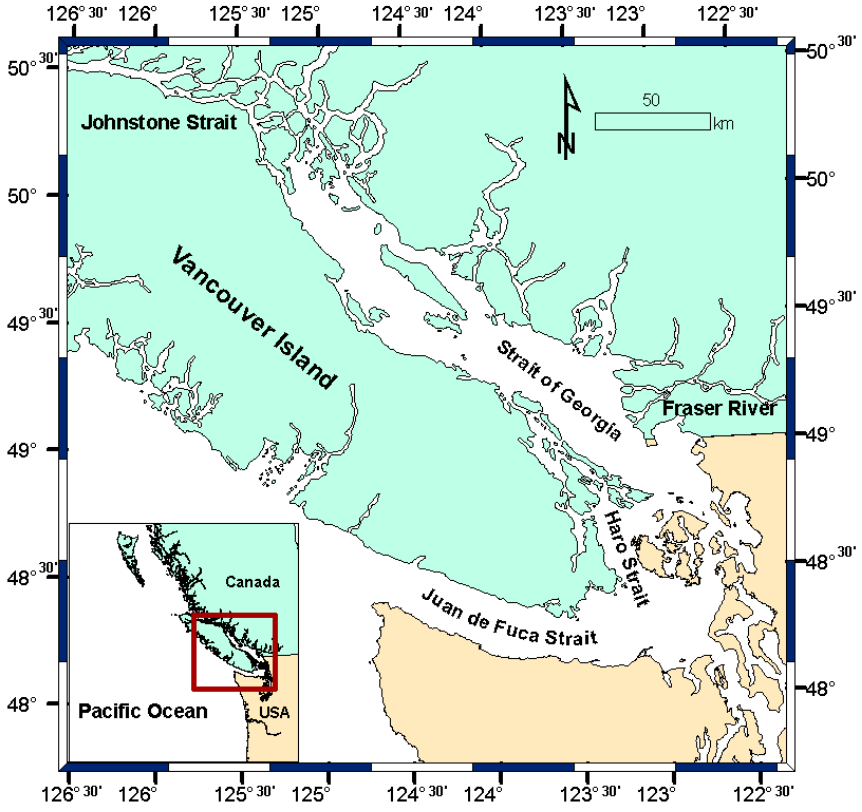

Figure 1.1: Map of the study area.

diate depth renewal may occur through Johnstone Strait into the northern portion of the Strait. In addition to these renewals, Masson (2006) also noted remineralisation of nutrients in the deeper waters of the Strait.

1.1.1 Fraser River

The Fraser River is exceeded only by the Columbia and Yukon Rivers for discharge into the Pacific Ocean from North America (Johannessen et al. 2003). With a drainage basin of $250,000$ km^2 and a mean annual discharge of 3400 m^{3}s^{-1}, the Fraser River is the most significant source of freshwater and suspended sediment into the Strait (Milliman 1980, Waldichuk 1983).

Of particular interest is the Fraser River freshet and its possible ecological effects on phytoplankton bloom dynamics. As identified in several studies ((Milliman 1980,

Kostaschuk et al. 1993), the discharge from the Fraser River can reach a peak of approximately 8,000 to 10,000 m^3 s^{-1} with a surge in sediment concentrations at the beginning of the freshet. In the summer, suspended sediment concentrations from the Fraser River decrease at a faster rate than the river discharge relative to spring conditions. Sediment laden water at the beginning of the freshet reduces light penetration through the water column, reducing phytoplankton growth in waters under the influence of the Fraser River plume (Harrison et al. 1983). As will be discussed in Section 1.1.2, the large volume of freshwater input can increase the stratification of the euphotic zone and influence phytoplankton bloom dynamics. Although primary productivity is nutrient limited in the Fraser River discharge during the summer, the possible entrainment of nutrient-rich deeper waters may increase phytoplankton growth in the outer portions of the Fraser River plume (Harrison et al. 1991).

1.1.2 Strait of Georgia Biology

Phytoplankton is an integral component of productivity in aquatic environments by providing a base for the food web through photosynthesis. An indirect indicator of productivity within a water body is the concentration of photosynthetic pigments, which have a direct impact on water colour. Within phytoplankton, the dominant photosynthetic pigment is commonly chlorophyll-a (*chl*) with other pigments present in lesser quantities (IOCCG 2000).

In the Strait of Georgia, *chl* concentrations have been found to range from $<$ 1 mg m^{-3} in the winter and reaching 10 to 50 mg m^{-3} during early spring (Harrison et al. 1983, Li et al. 2000). Peak *chl* concentrations are associated with the spring bloom usually during late March to early April (Harrison et al. 1983, Haigh and Taylor 1991) with noted fluctuations possibly related to El Niño conditions (Yin 1997).

Growth of phytoplankton is commonly limited by one of two factors, either light

or macronutrient deficiency. In warmer equatorial waters, around Oregon and California, the limiting factor is usually macronutrients and in northern waters around Alaska the major limiting factor is usually the amount of available solar energy (Gargett 1997). The Strait of Georgia is in the transitional region between these two types of environments with summers leading to nutrient deficiencies and winter leading to light deficiencies (Li et al. 2000). With the transition from nutrient rich conditions in winter to light rich conditions in summer, the spring conditions are advantageous to phytoplankton growth. This transitional period is possibly important to higher marine trophic levels that migrate during this time by providing a larger food source for zooplankton, which the higher trophic levels feed on during migration along North American coastal waters (Gargett 1997).

An important aspect to the pelagic food web of the Strait is the factors limiting phytoplankton growth and how these factors are possibly linked to cycles of other organisms in the marine food web (Harrison et al. 1983, Haigh and Taylor 1991). For instance, changes in the dominant phytoplankton bloom community composition may influence the structure of the food web. As shown in Fig. 1.2, higher trophic levels, such as herring and salmon, generally favour macrozooplankton that feed on larger centric diatoms (Harrison et al. 1983). Possible shifts in diatom bloom timing may affect the success rate of macrozooplankton and hence the success of salmon spawning runs (Parsons and Kessler 1987).

In addition to the two major limiting factors to phytoplankton growth identified previously, stability and stratification of the upper water column may impact phytoplankton growth (Mann 1993). Winter conditions in the Strait usually involve higher wind speeds, creating instability and mixing in surface waters. This is not conducive to phytoplankton growth because they are continuously moved in and out of the euphotic zone. Contrarily, in the spring, winds are generally calmer and larger influxes of freshwater create abrupt temperature and salinity gradients that provides

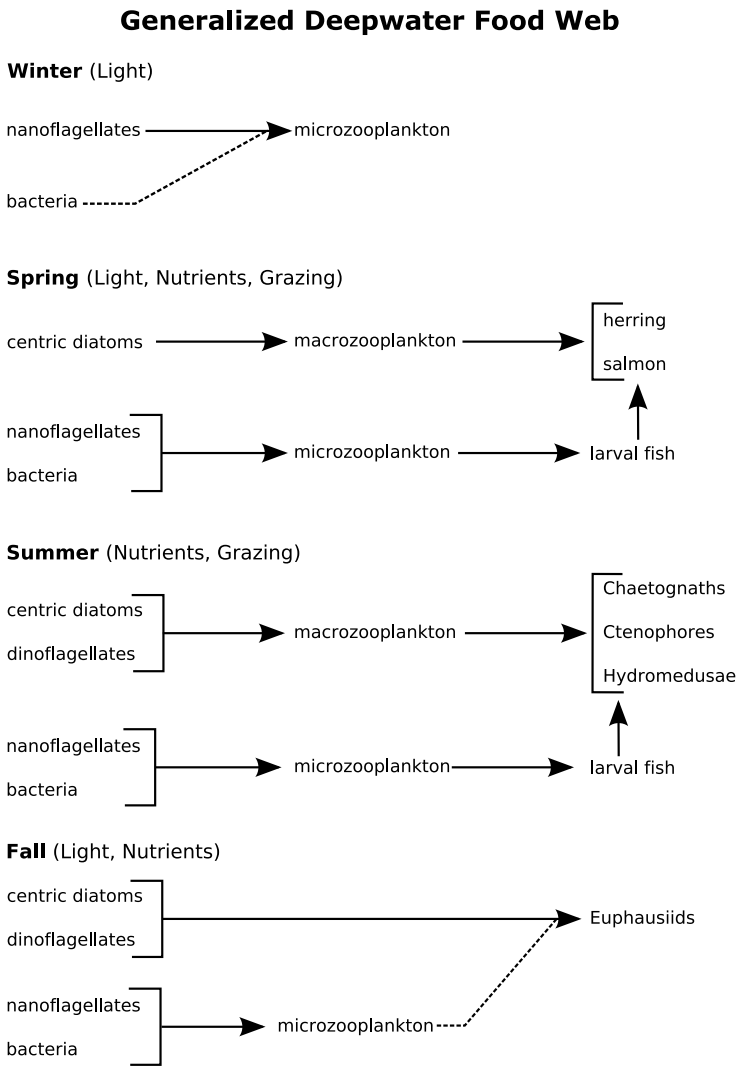

Figure 1.2: A generalized food web for deepwaters in the Strait of Georgia (modified from Harrison et al. 1983). Of particular interest are the limiting factors for phytoplankton growth during each season, which are shown in parenthesis beside each season.

a greater degree of stratification in the upper water column. With this increased stratification, there is limited mixing with the nutrient-rich deeper waters and phytoplankton consumes all the nutrients within the euphotic stratified layer (Gargett 1997). Transition between the nutrient-rich well-mixed water column to stratified nutrient limited water column can create an "optimal window" for phytoplankton blooms to occur (Mann 1993). According to Collins (2005), wind was found to explain 75% of variance in the arrival time of the spring bloom. In other words, the water column stratification in early spring and therefore the spring bloom is dominantly triggered by the decrease in wind. This is contrary to previous studies (Yin et al. 1997) that identified that the dominant trigger was the influx of freshwater from the Fraser River.

Furthermore, phytoplankton community composition has been found to vary between different regions of the Strait. Past sampling campaigns of phytoplankton community structure have been carried out for the central (Harrison et al. 1983) and northern (Haigh and Taylor 1991) portions of the Strait. As identified by Harrison et al. (1983), centric diatoms dominated the phytoplankton community during the summer of 1975 in the central portion of the Strait. In the northern portion, phytoplankton communities were dominated by non-loricate oligotrichs and dinoflagellates during the spring bloom of 1986 (Haigh and Taylor 1991). The spring bloom in the northern portion transitioned to flagellates except for a few pockets of diatoms near the central portion of the Strait. According to the authors, these differences in phytoplankton community composition in the northern portion of the Strait may have been related to increased wind activity in the region. Harrison et al. (1983) noted that diatoms were of particular abundance around the Fraser River plume and entrances to inlets. The trend was further supported through data collected by Haigh and Taylor (1991) were it was found that diatom populations were abundant near the entrance to Sutil Channel and by Cape Lazo. As shown by these studies, the

phytoplankton community composition can vary both spatially and temporally.

1.2 Remote Sensing Theory

The main objective behind optical remote sensing is to use electromagnetic radiation, or light, to retrieve information about a target without coming into physical contact with it (Martin 2004). When analysing ocean-colour imagery acquired by satellites, many environmental variables influence the amount of light that is reflected back to the satellite sensor. As electromagnetic radiation travels through Earth's atmosphere and possibly interacts with the water column, the radiation can interact with several substances and travel in different paths. Fig. 1.3 depicts several of the more common environmental variables, such as atmospheric and water column constituents, that light may interact with when traveling from the sun to the satellite sensor. A detailed discussion of atmospheric optical constituents is provided in Section 1.3 and in Section 1.4 the influence of water column constituents on light attenuation is discussed. In the remainder of this section, the basic optical units and how they relate to light or radiometric measurements are discussed.

To evaluate biophysical variables, such as chlorophyll-a (*chl*) concentrations, and their associated influence on measured electromagnetic radiation above the water surface, the inherent optical properties of these variables must be differentiated from their influence on the apparent optical properties of the water body. It is important to note that the following discussion of inherent optical properties focuses on elastic scattering for which the wavelength of the incident light does not change. Inelastic scattering or transpectral scattering, which changes the wavelength of the incident light, is not discussed. Inelastic scattering processes in aquatic environments include *chl* fluorescence (Gower et al. 1999, 2004) and Raman scattering (Bartlett et al. 1998). Although effects of light polarization are also not discussed, the analysis of polarization influence on remote-sensing reflectance is provided by other authors

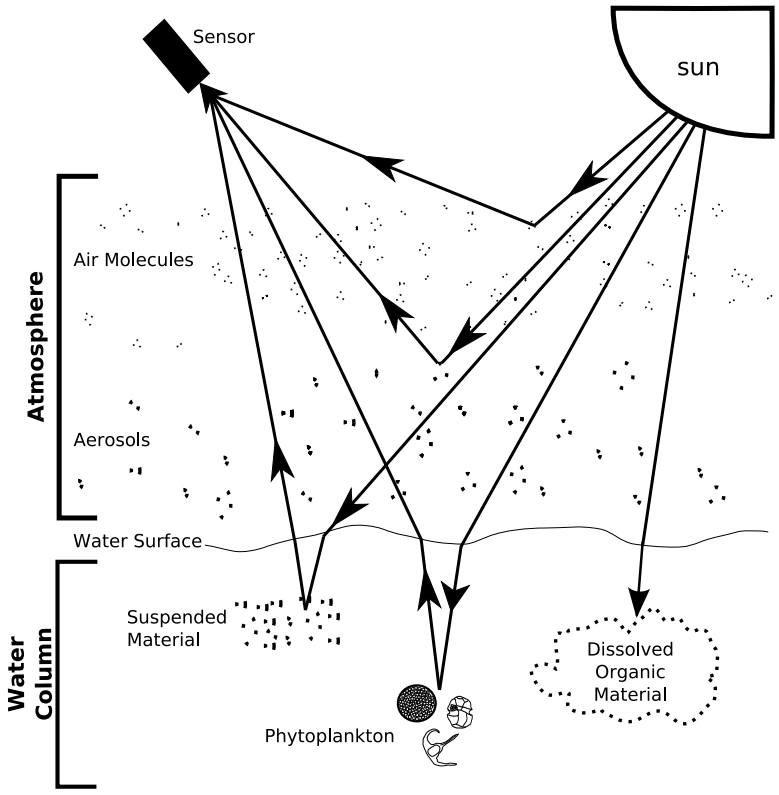

Figure 1.3: Typical interactions encountered by photons measured in an ocean-colour image. While not presented on the graphic, interactions between and within each component, through multiple scattering, do occur.

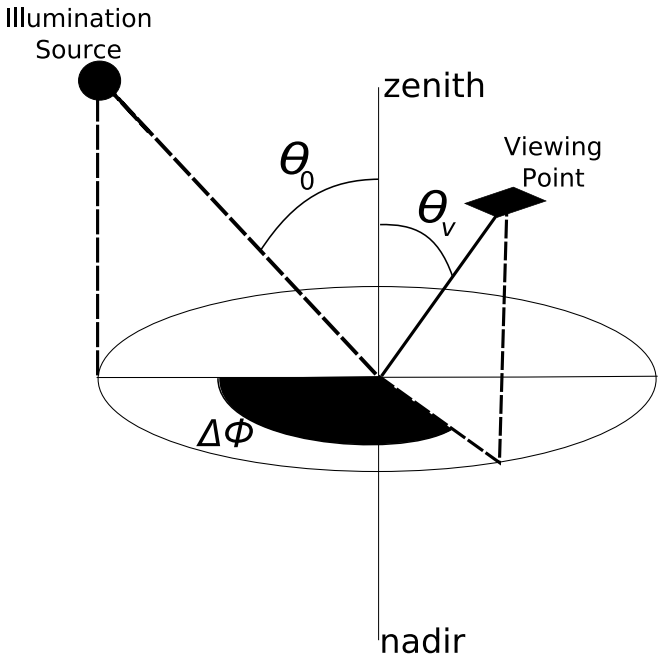

Figure 1.4: The geometric definitions used in this study. The graphic is reproduced based on a similar image by Loisel and Morel (2001).

(Chami and Platel 2007, Chami 2007).

Geometry of the radiometric measurements is an important component in relating apparent optical properties of a water body to its inherent optical properties. For this study, the geometry defined by Loisel and Morel (2001) and shown in Fig. 1.4 was used.

The solar zenith angle, θ_0, is the angle formed by a vector perpendicular or normal to the medium surface and a vector in the illumination direction. The view zenith angle, θ_v, is formed by the vector normal to the medium surface and the vector in the sensor direction. $\Delta\phi$ is the azimuth angle difference between the illumination and view vector on the plane parallel to the medium surface. The combination of the solar zenith, view zenith, and azimuth difference angles are used to form the scattering angle, ψ, from the cosine law of spherical geometry (Mueller et al. 2003a). ψ is defined as

$$\cos\psi = -\cos\theta_0\cos\theta_v - \sin\theta_0\sin\theta_v\cos\Delta\phi \tag{1.1}$$

1.2.1 Inherent Optical Properties

To characterize the inherent optical properties (IOPs) of a medium, the absorption, $a(\lambda)$, and scattering, $b(\lambda)$, coefficients are generally used (Mueller et al. 2003a). The angular distribution of the scattering is described through the scattering phase function, $\tilde{\beta}(\lambda, \psi)$ (Mobley et al. 2002).

The absorption coefficient of a medium describes the portion of monochromatic light that is removed from the optical path for a given path length (m^{-1}). The energy that is removed from the optical path is converted to another form of energy, such as heat. For some mediums, such as pure water, the absorption coefficient is commonly defined using a constant. However, the absorption coefficient can be dependent upon the properties of the medium. For example, the absorption properties of water can vary at certain wavelengths in relation to temperature and salinity differences (Pegau et al. 1997).

The scattering coefficient, $b(\lambda)$, defines the portion of the incident light beam that is sent in a direction other than the incident beam. To relate the probability of light scattering at a particular angle, the scattering phase function must be identified. Identifying the scattering phase function is usually done in one of two approaches. One approach is to derive it theoretically, assuming spherical particles using Mie theory with the refractive index and size distribution of the particles. This approach has been carried out for a range of particles types (Ulloa et al. 1994, Woźniak and Stramski 2004) and several predefined models exist, such as one defined by Fournier and Forand (1994). The second is to measure the volume scattering function, $\beta(\lambda, \psi)$, which is related to the scattering phase function using Eq. (1.2) (Mobley et al. 2002).

$$\tilde{\beta}(\lambda, \psi) = \beta(\lambda, \psi)/b(\lambda) \tag{1.2}$$

The volume scattering function defines the portion of incident light scattered at a particular angle, ψ. The selection of the scattering phase function can have significant influence on the modelling of the reflectance properties for a water body (Mobley et al. 2002). Nevertheless, it is one of the least measured and most difficult to measure IOPs. The most commonly used measurements are a set of 8 volume scattering functions measured for several different water bodies provided by Petzold (1972). While not looking at the full phase function, several studies have measured particulate scattering in relation to different particulate types and their wavelength dependences (Babin et al. 2003a, Bowers and Binding 2006).

The sum of the scattering in the upper portion of the volume scattering coefficient or in the opposite direction of the incident light is described by the backscattering coefficient, $b_b(\lambda)$. To model remote-sensing reflectance above the water surface, the backscattering coefficient is commonly used (Gordon et al. 1988b) and is derived from the volume scattering function based on the following.

$$b_b(\lambda) = 2\pi \int_{\frac{\pi}{2}}^{\pi} \beta(\lambda, \psi) \sin\psi \; d\psi, \; \mathrm{m}^{-1} \tag{1.3}$$

The scattering to backscattering ratio, $\tilde{b}_b$, is commonly used to estimate backscattering from the more readily measured scattering coefficient. The most commonly used backscatter ratios are derived from the volume scattering functions measured by Petzold (1972) and range from 0.044 for clear ocean water to 0.013 for coastal waters (Mobley 1994). The reason for the higher $\tilde{b}_b$ in clear water is because the scattering is more isotropic, while for turbid waters the scattering is dominated by forward scattering.

Relating an IOP to a biophysical variable, such as *chl*, is typically done using a

specific optical property. The specific optical property defines how the IOP varies with the biophysical variable. For example, the specific absorption coefficient for a given biophysical variable, $a^*(\lambda)$, can be described using the linear relationship in Eq. (1.4) with $a(\lambda)$ representing the absorption coefficient of the biophysical variable at a given concentration, n.

$$a^*(\lambda) = a(\lambda)/n \tag{1.4}$$

A similar relationship is commonly used to define the specific backscatter coefficient of a biophysical variable (Gallie and Murtha 1992, Maritorena et al. 2002). In addition to the linear form of Eq. (1.4), non-linear relationships are also used (Morel and Maritorena 2001, Devred et al. 2006).

To describe the optical properties of a medium, as well as the combined influence from scattering and absorption, the single-scatter albedo, $\varpi(\lambda)$, is commonly used. The single-scatter albedo (Eq. (1.5)) describes the probability of a photon's survival upon interaction with the medium.

$$\varpi(\lambda) = \frac{b(\lambda)}{b(\lambda) + a(\lambda)} \tag{1.5}$$

For optical constituents that are weakly or nonabsorbing, the single-scatter albedo will approach one, while for strongly absorbing constituents, the albedo will approach zero. For example, water is generally considered a strongly absorbing medium with a $\varpi(550) = 0.033$ (Mueller 2003) and Maritime aerosols are a weakly absorbing medium with $\varpi(550) = 0.996$ at 90% humidity (Shettle and Fenn 1979).

1.2.2 Apparent Optical Properties

To associate the inherent optical properties with the apparent optical properties (AOP), measured radiometric quantities and their geometric dependences must be related to the optical properties of the medium (the water column) (Mobley 1994).

In optical oceanography the two most common measured radiometric quantities are radiance, $L(\lambda, \theta_0, \theta_v, \Delta\phi)$, and irradiance, $E(\lambda, \theta_0)$. Radiance measurements are dependent upon a solid angle identified by a view zenith angle, θ_v, a solar zenith angle, θ_0, and an azimuth angle difference between the illumination (commonly the sun) and viewing vector, $\Delta\phi$, as shown in Fig. (1.4). Irradiance measurements do not have a view or azimuth angle and are a measure of total energy from a plane surface. Radiance can be related to irradiance using Eq. (1.6), in which irradiance is defined as the sum of radiance measurements for all view and azimuth angles within a hemisphere.

$$E(\lambda, \theta_0) = \int_0^{2\pi} \int_0^{\frac{\pi}{2}} L(\lambda, \theta_0, \theta_v, \phi) \cos\theta_v \sin\theta_v \; d\theta_v d\phi, \;\; \mu\text{W cm}^{-2}\text{nm}^{-1} \tag{1.6}$$

Based on the irradiance definition, the irradiance reflectance from a plane surface is defined as

$$R(\lambda, \theta_0) = E_u(\lambda, \theta_0)/E_d(\lambda, \theta_0) \tag{1.7}$$

where $E_d(\lambda, \theta_0)$ is the downwelling irradiance at a particular wavelength that is received by the plane surface and $E_u(\lambda, \theta_0)$ is the upwelling irradiance that is reflected by the plane. In the case of an aquatic environment, the downwelling irradiance is the irradiance that passes through the atmosphere and is measured below the air-water interface. Upwelling irradiance, on the other hand, is the irradiance that is being returned to the atmosphere from the water column and is also measured below the air-water interface.

The variability of downwelling radiance, $L_u(\lambda, \theta_0, \theta_v, \Delta\phi)$, in relation to $E_u(\lambda, \theta_0)$ is commonly summarized as a function $Q(\theta_0, \theta_v, \Delta\phi)$ and defined as (Loisel and Morel 2001)

$$Q(\theta_0, \theta_v, \Delta\phi) = \frac{E_u(\lambda, \theta_0)}{L_u(\lambda, \theta_0, \theta_v, \Delta\phi)}, \text{ sr} \tag{1.8}$$

The form of the $Q(\theta_0, \theta_v, \Delta\phi)$ function is dependent upon the total volume scattering function, which is the sum of the volume scattering functions for each optical constituent (Mueller et al. 2003a). The value of Q has found to range from 0.3 to 6.5 sr (Morel and Gentili 1993). However, Q values estimated by Sathyendranath et al. (2004a) off Vancouver Island ranged from about 2 to 8 sr.

A important component to measuring radiance from a water body is the air-water interface and its influence on downwelling and upwelling radiance. Due to the difference in refractive index of water in relation to air, Snell's law dictates that a component of the upwelling radiance, L_u, is internally reflected back into the water column. The resulting measured energy that leaves the water column, passing through the air-water interface, is referred to as the water-leaving radiance. The relationship between water-leaving radiance, L_w, and L_u, while varying with windspeed (Gordon 2005) and weakly with atmospheric properties (Wang 2006b), is defined as

$$L_w(\lambda, \theta_0, \theta_v, \Delta\phi) = \mathfrak{R}(\lambda, \theta_0, \theta_v) L_u(\lambda, \theta_0, \theta_v, \Delta\phi), \ \mu\text{W cm}^{-2}\text{nm}^{-1}\text{sr}^{-1} \tag{1.9}$$

where

$$\mathfrak{R}(\lambda, \theta_0, \theta_v) = \left\{ \frac{t_f(\theta_0)\bar{t}_f(\theta_v)}{m^2[1 - \bar{r}R(\lambda, \theta_0)]} \right\} \tag{1.10}$$

$t_f(\theta_0)$ represents the transmittance of the solar energy into the water and $\bar{t}_f(\theta_0)$ the transmittance from the water into the air. Both of these variables vary with wind speed, solar, and viewing geometry. However, $\mathfrak{R}$ can be replaced by the Fresnel Reflectance function representing a flat-water surface for a range of conditions to

within 0.01 (Gordon 2005). For Eq. (1.10), $R(\lambda, \theta_0)$ is defined in Eq. (1.7), m is the refractive index of water, and $\bar{r}$ is the reflectance of upward irradiance by the interface. As noted by Gordon (2005), $R(\lambda, \theta_0)$ is relatively low in open-ocean waters and $\bar{r}$ is approximately 0.48. Thus, the influence of $\bar{r}R(\lambda, \theta_0)$ and the associated influence of water column IOPs on the value of $\mathfrak{R}(\lambda, \theta_0, \theta_v)$ in more open waters is limited. An $\mathfrak{R} = 0.529$ is appropriate for a range of illumination, view geometries, and wind speeds. In more turbid waters, the $R(\lambda, \theta_0)$ value may not be as low and the relationship between above- and below-water reflectance defined by Lee et al. (1999) and used later in Chapter 2 (Section 2.2.2) may be more appropriate under a greater range of conditions.

In addition to influence from the air-water interface, radiance measurements have a strong dependence on illumination conditions. Slight variations in atmospheric properties or solar zenith angles can cause variations in the downwelling irradiance and the resulting upwelling radiance measurement. To minimize these variations, radiance measurements are normalized to illumination conditions, resulting in remote-sensing reflectance, $R_{rs}(\lambda)$, (Eq. (1.11)) and normalized water-leaving radiance, $L_{wn}(\lambda)$, (Eq. (1.12)) (Morel and Gentili 1996, Mueller et al. 2003a).

$$R_{rs} = \frac{L_w(\lambda, \theta_v, \theta_0, \Delta\phi)}{E_s(\lambda, \theta_0)},\ \mathrm{sr}^{-1} \tag{1.11}$$

$$L_{wn} = L_w(\lambda, \theta_v, \theta_0, \Delta\phi)\frac{\bar{F}_o(\lambda)}{E_s(\lambda, \theta_0)},\ \mu\mathrm{W\ cm}^{-2}\mathrm{nm}^{-1}\mathrm{sr}^{-1} \tag{1.12}$$

$\bar{F}_o(\lambda)$ is the extraterrestrial solar spectral irradiance based on a mean earth-sun distance (Thuillier et al. 2003) and $E_s(\lambda)$ is the downwelling sky irradiance measured above the water surface. For radiometric field measurements, $R_{rs}(\lambda)$, is commonly used and extraterrestrial remote sensing reflectance, $\rho(\lambda)$, is frequently used with satellite imagery (Morel and Gentili 1996, Gordon 1997), which is defined as

$$\rho(\lambda) = \frac{\pi L(\lambda)}{\bar{F}_0(\lambda)\cos\theta_0\left(\frac{d_0}{d}\right)^2} \tag{1.13}$$

where d and d_0 are the actual and mean earth-sun distance, respectively. Extraterrestrial water reflectance, $\rho_w(\lambda)$, can be related to field remote-sensing reflectance using Eq. (1.14) with $t(\lambda, \theta_0)$ representing the diffuse transmittance of the atmosphere (Mueller et al. 2003c). The difference between R_{rs} and ρ is that $E_s(\lambda, \theta_0)$ in Eq. (1.11) is replaced with the total irradiance from the sun before entering the atmosphere (Gordon and Wang 1994, Mueller et al. 2003c). The $R_{rs}(\lambda)$ variable has the unit sr^{-1} to represent the solid angle nature of the measurement and $\rho(\lambda)$ is unitless.

$$R_{rs}(\lambda) = \frac{\rho_w(\lambda)}{\pi t(\theta_0, \lambda)} \tag{1.14}$$

1.2.3 Relating Inherent and Apparent Optical Properties

The relationship between inherent and apparent optical properties is more accurately done using numerical simulations (Mobley et al. 1993), such as Monte Carlo simulations. Nevertheless, the use of quasi-single-scattering approximation (Gordon et al. 1988b) provides agreement with simulations of $\sim 2\%$ to $\sim 10\%$ for sea surface reflectance (Lee et al. 2002). The quasi-single-scattering model is defined as

$$R_{rs}(\lambda) = \mathfrak{R}(\theta_0, \theta_v)\frac{f'(\theta_0, \theta_v, \Delta\phi, IOP)}{Q(\theta_0, \theta_v, \Delta\phi, IOP)}\frac{b_b(\lambda)}{b_b(\lambda) + a(\lambda)} \tag{1.15}$$

with $f'(\theta_0, \theta_v, \Delta\phi, IOP)$ representing a unitless factor that is dependent on geometry and water column IOPs, $Q(\theta_0, \theta_v, \Delta\phi, IOP)$ is previously defined in Eq. (1.8), and $\mathfrak{R}(\theta_0, \theta_v)$ represents the air-water interface, as previously defined in Eq. (1.10). The $b_b(\lambda)$ and $a(\lambda)$ are IOPs and represent the sum of the backscattering and absorption coefficients of the optical constituents within the water column, respectively.

Although normalizing the radiance measurements with the downwelling irradi-

ance in Eq. (1.11) reduces the influence from varying solar zenith angle and atmospheric properties, the geometric dependence of the radiance measurement is still present. This geometric dependence, represented in the $f'(\theta_0, \theta_v, \Delta\phi, IOP)$ and $Q(\theta_0, \theta_v, \Delta\phi, IOP)$, is associated with the scattering phase function of the medium. Variability in reflectance related to geometry is commonly referred to as the bi-directional reflectance properties of the water and can be modelled into the bi-directional reflectance distribution function (BRDF) of the water body (Loisel and Morel 2001).

Using a BRDF model, radiometric measurements captured under different illumination and viewing geometries can be adjusted from normalized water-leaving radiance, L_{wn}, to exact normalized water-leaving radiance, L_{wn}^{ex}, which has a predefined consistent geometry. The commonly used geometry for L_{wn}^{ex} is to have the solar and viewing zenith angles equal to zero, so that they are both at nadir with an undefined azimuth. This is also the common geometry used to set the f'/Q variables in semi-analytical ocean-colour algorithms (Carder et al. 1999, Maritorena et al. 2002). The adjustment of L_{wn} to L_{wn}^{ex} is done through (Morel and Gentili 1996)

$$L_{wn}^{ex}(\lambda) = L_{wn}(\lambda, \theta_v, \theta_0, \Delta\phi)\frac{\mathfrak{R}_0}{\mathfrak{R}(\theta_0, \theta_v)}\frac{f'_0(IOP)}{Q_0(IOP)} \times \left(\frac{f'(\theta_0, \theta_v, \Delta\phi, IOP)}{Q(\theta_0, \theta_v, \Delta\phi, IOP)}\right)^{-1} \quad (1.16)$$

which requires a model of f'/Q over a range of geometric configurations and IOPs. The $f'_0(IOP)$, $Q_0(IOP)$, and $\mathfrak{R}_0$ terms have their view and solar angle dependences removed because they are the values for a solar and view zenith angle of zero with an undefined azimuth.

A model of f'/Q provided by Morel et al. (2002) has shown to compare well with measurements (Voss and Morel 2005). However, the model is based on case 1 waters and was compared against equatorial waters. As will be discussed in Section 1.4,

both of these criteria are not applicable in the Strait of Georgia. A comparison of a f'/Q for different geometries using a sediment dominant and chromophoric dissolved organic matter (CDOM) dominant water body found that the coefficients can vary significantly, particularly as the solar and viewing zenith angles deviate from nadir (Loisel and Morel 2001). This divergence is related to the single-scattering albedo (Eq. (1.5)) of each water body. For water bodies with higher absorption from CDOM, single scattering events dominate and the BRDF are more closely related to the volume scattering functions of the particles. Conversely, for sediment dominated waters, the BRDF of the water body is not as closely tied to the particulate volume scattering and the reflectance distribution is more diffuse.

1.3 Atmospheric Optical Properties

When measuring energy reflected by Earth's surface, it is important to account for how that energy is influenced by passing through the Earth's atmosphere. Similar to aquatic environments, it is crucial to define the inherent optical properties of the medium, in this case the optical constituents in the air column above the water surface. By defining atmospheric IOPs, the influence of atmospheric constituents on ocean-colour imagery can be described.

In the next two sections, the inherent optical properties of the atmosphere are defined and the associated influence on ocean-colour imagery is discussed.

1.3.1 Atmospheric Inherent Optical Properties

The absorption, $a(\lambda)$, and scattering, $b(\lambda)$, coefficients, in conjunction with the scattering phase function discussed in Section 1.2.1, are used to describe optical constituents within the atmosphere. In addition to the absorption and scattering coefficients, the extinction coefficient, $c(\lambda)$, (Eq. (1.17)) is commonly used to describe the influence of an optical constituent (Gordon and Wang 1994).

$$c(\lambda) = a(\lambda) + b(\lambda) \tag{1.17}$$

When the extinction coefficient is integrated over entire height of the atmosphere, z, the atmospheric optical thickness, $\tau(\lambda)$ can be defined as

$$\tau(\lambda) = \int_0^z c(\lambda)\ dz \tag{1.18}$$

The optical thickness defines the amount of influence the atmospheric constituents have on electromagnetic radiation passing through the atmosphere at a particular wavelength.

1.3.2 Atmospheric Influence on Ocean-Colour Imagery

Using the definitions of inherent optical properties, the atmospheric influence on ocean colour can be estimated. To describe this influence, the extraterrestrial reflectance (Eq. (1.13)) is used to approximate the total reflectance measured at the top of the atmosphere, $\rho_t(\lambda)$, as (Gordon and Wang 1994, Gordon 1997)

$$\rho_t(\lambda) = \rho_r(\lambda) + \rho_{as}(\lambda) + \rho_{ra}(\lambda) + t(\lambda)\rho_w(\lambda) \tag{1.19}$$

where $\rho_r(\lambda)$ is the reflectance from air molecules (Rayleigh scattering), $\rho_{as}(\lambda)$ the scattering from aerosols, and $\rho_{ra}(\lambda)$ the multiple scattering between air molecules and aerosols. The isolation of $\rho_w(\lambda)$ is critical to ocean-colour remote sensing, thus, it is important to characterize the other components in Eq. (1.19). The contribution of $\rho_r(\lambda)$ is well characterized based on geometry and atmospheric pressure (Gordon et al. 1988a, Wang 2005). $\rho_{ra}(\lambda)$ is dependent upon the aerosol type, aerosol reflectance and Rayleigh optical depth. $\rho_{as}(\lambda)$ is provided by (Gordon and Wang 1994)

$$\rho_{as}(\lambda) = \varpi_a(\lambda)\tau_a(\lambda)p_a(\lambda, \theta_0, \theta_v, \Delta\phi)/4\cos\theta_v\theta_0,$$
$$p_a(\lambda, \theta_0, \theta_v, \Delta\phi) = P_a(\psi_-, \lambda) + (r(\theta_v) + r(\theta_0))\, P_a(\psi_+, \lambda), \tag{1.20}$$
$$\cos\psi_\pm = \pm\cos\theta_0\cos\theta_v - \sin\theta_0\sin\theta_v\cos\Delta\phi$$

where ϖ_a is the aerosol single-scatter albedo represented by Eq. (1.5), $\tau_a(\lambda)$ is the aerosol optical thickness from Eq. (1.18), $P_a(\psi, \lambda)$ is the aerosol scattering phase function, and $r(\theta)$ is the Fresnel reflectance of the interface at an incident angle θ. The component relating to the scattering angles $\psi_\pm$ is an extension of Eq. (1.1) and accounts for the aerosol scattering geometry from the sun to the surface and from the surface to the sensor.

The modelling of the aerosol scattering phase function, $P_a(\psi, \lambda)$, in Eq. (1.20) requires the inherent optical properties of the aerosol types typically found in marine environments. The aerosol IOPs commonly used are defined by Shettle and Fenn (1979) and include oceanic, marine, and tropospheric aerosols with varying relative humidities and an addition coastal model defined by Wang and Gordon (1994). The aerosol model refractive index and particle size distribution are used with Mie theory to produce a theoretical scattering phase function assuming spherical particles.

Characterization of atmospheric aerosols is an important component to atmospherically correcting ocean-colour imagery and the isolation of ρ_w in Eq. (1.19). The approaches to aerosol characterization and atmospheric correction are discussed further in Chapter 3.

1.4 Water Column Optical Properties

Initial forays into oceanographic remote sensing began with the estimation of chlorophyll-a (*chl*) concentrations in open-ocean waters. To accomplish this task, two major assumptions were made. The first was that *chl* is the dominant optical constituent and the second assumption was that all other constituents, such as chromophoric dis-

solved organic matter (CDOM) and suspended particulate, are absent or correlated with *chl* concentration (Gordon and Morel 1983, Morel and Maritorena 2001). These water types are typically classified as case 1.

The more general water classification, referred to as case 2, assumes that all major constituents vary independently (Gordon and Morel 1983). This is usually the situation in coastal waters with significant terrestrial influence, such as the Strait of Georgia. In case 2 waters, the major optical constituents typically considered are: pure water, photosynthetic pigments, suspended particulate and CDOM (IOCCG 2000). Each of these major constituents and their inherent optical properties will be discussed in the context of ocean colour for the Strait of Georgia in the following sections.

1.4.1 Pure Water

The optical properties of water have been reviewed by both the International Ocean Colour Coordination Group (IOCCG 2000) and Mueller et al. (2003b). Accordingly, a key optical characteristic of pure water is the strong absorption of the red and near-infrared (NIR) wavelengths (Fig. 1.5). This characteristic limits the usable portion of the spectrum for ocean-colour remote sensing to the visible wavelengths and in turbid waters, the shorter NIR wavelengths up to approximately 800 nm (Ruddick et al. 2001). The backscattering coefficients of water are generally lower than the absorption coefficients in the visible wavelengths and are highest in the blue wavelengths (Fig. 1.5), giving large clear water bodies a blue colour. Optical properties of water also have a dependence on temperature and salinity at certain wavelengths > 550 nm (Sullivan et al. 2006).

1.4.2 Photosynthetic Pigments

Photosynthetic pigments are crucial to phytoplankton for the photosynthetic process, which creates organic compounds from solar energy (Martin 2004). While all

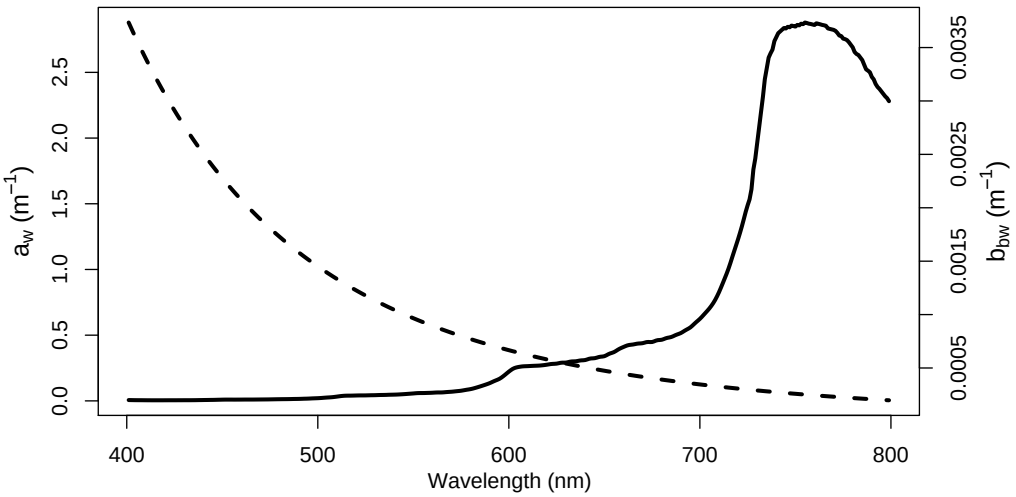

Figure 1.5: Water absorption, a_w, (solid) and backscatter, b_{bw}, (dashed) in the visible and NIR wavelengths. Values are taken from Mueller (2003). Note the difference in scale between the absorption (left hand scale) and backscatter (right hand scale) coefficients.

photosynthetic pigments impact ocean colour, *chl* is typically the dominant pigment. Concentrations of *chl* within aquatic environments have historically been used in ocean-colour remote sensing as a proxy for phytoplankton biomass because of its distinctive absorption features in the blue and red portions of the spectrum (Fig. 1.6) and its common dominance in relation to other pigments. An important note is that surface estimated *chl* concentrations may not necessarily be directly related to primary productivity because primary productivity is a time/depth integrated variable and the relationship between *chl* concentrations and biomass is phytoplankton community dependent. Relationships between *chl* and primary productivity have been modelled through several studies and a review is provided by Behrenfeld and Falkowski (1997).

The development of algorithms to estimate *chl* concentrations have historically been based on the absorption properties of *chl* fitted to empirically derived formulas. To develop these algorithms, a data set of *in situ* radiometric and *chl* concentration measurements in a diverse set of conditions are needed to model *chl* concentrations to satellite band configurations. These measurements are than used to develop empirical

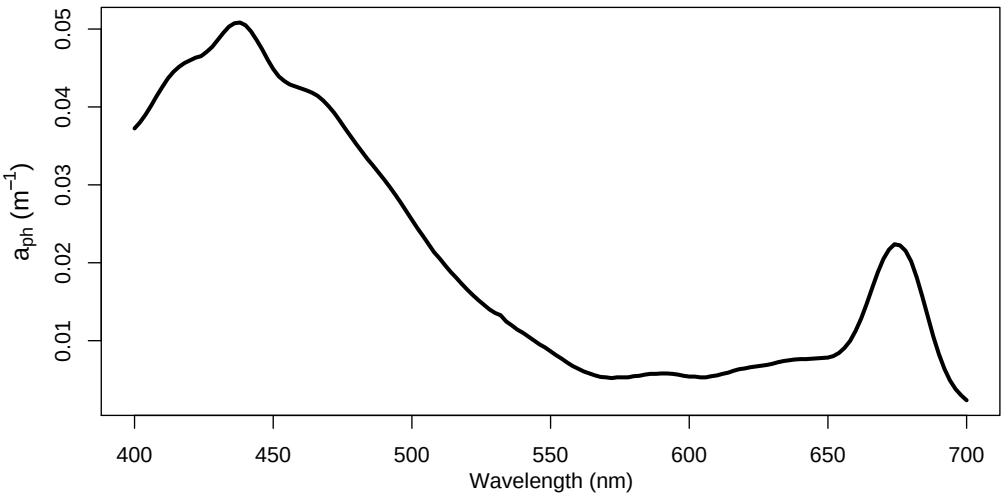

Figure 1.6: Phytoplankton absorption, a_{ph}, for 1 mg m^{-3} of chlorophyll-a based on the Devred et al. (2006) general two-component phytoplankton absorption model.

algorithms for estimating *chl* concentrations based on reflectance ratios at various wavelengths (O'Reilly et al. 1998).

To improve the accuracy of *chl* algorithms, NASA has developed a data set known as SeaWiFS Bio-optical Archive and Storage System (SeaBASS) (O'Reilly et al. 1998, Bailey and Werdell 2006). SeaBASS includes a total of 2,853 sets of multispectral ocean-colour and *chl* concentrations measurements, ranging from 0.008 to 90 mg m^{-3} with the majority of measurements representing 0.08 to 3 mg m^{-3} (O'Reilly et al. 2000).

Historically, *chl* algorithms developed from equatorial measurements, such as the OC3M algorithm, have underestimated *chl* concentrations above $\sim 50^{\circ}$ latitude (IOCCG 2000). In these regions, phytoplankton community composition has an impact on phytoplankton absorption coefficients, with larger diatoms absorbing less light in the blue wavelengths compared to phytoplankton communities found at lower latitudes with the same *chl* concentration (Sathyendranath et al. 2001). As pointed out in Section 1.1.2 and Fig. (1.2), diatom phytoplankton blooms are common during certain periods in the Strait and may have distinctive influence on standard *chl*

algorithms.

The lower absorption characteristics of *chl* associated with larger phytoplankton cells, such as diatoms, compared to smaller cells, such as prymnesiophytes, is due to the packaging effect, which causes *chl* to form discrete packets instead of being continuously dispersed within the phytoplankton cellular structure (Kirk 1994). This packaging of pigments results in lower specific absorption coefficients at blue wavelengths and an underestimation of *chl* concentrations from generalized algorithms based on phytoplankton communities with limited packaging effect. While the packaging effect significantly influences the blue wavelengths, *chl* absorption properties at wavelengths > 623 nm are not significantly influenced (Stuart et al. 1998).

1.4.3 Suspended Particles

Suspended particles in aquatic environments consist of two main groups, organic and inorganic. Organic particles can originate *in situ* from detritus and the cellular structure of phytoplankton, as well as from terrestrial sources through land runoff. Inorganic particles are usually from terrestrial mineralogic sources and, while they can be found far from continental shelves, they is generally limited to coastal waters (Woźniak and Stramski 2004, Loisel et al. 2006).

Inherent optical properties of suspended particles are typically described as the absorption from non-algal particles, a_{NAP}, which includes absorption from particles excluding photosynthetic pigments (Babin et al. 2003a,b), and particulate backscatter, b_{bp}. Particulate backscatter corresponds to scattering from the phytoplankton cellular structure, mineralogic, and colloidal particles (Babin et al. 2003a, Stramski et al. 2004, Stramski and Woźniak 2005), which is the total backscatter minus the backscatter from the water.

Based on the assumption of spherical particles, particulate backscatter properties are dependent upon the particle size distribution and their refractive index (Ulloa et al. 1994, Babin et al. 2003a). As the particle size distribution shifts from one

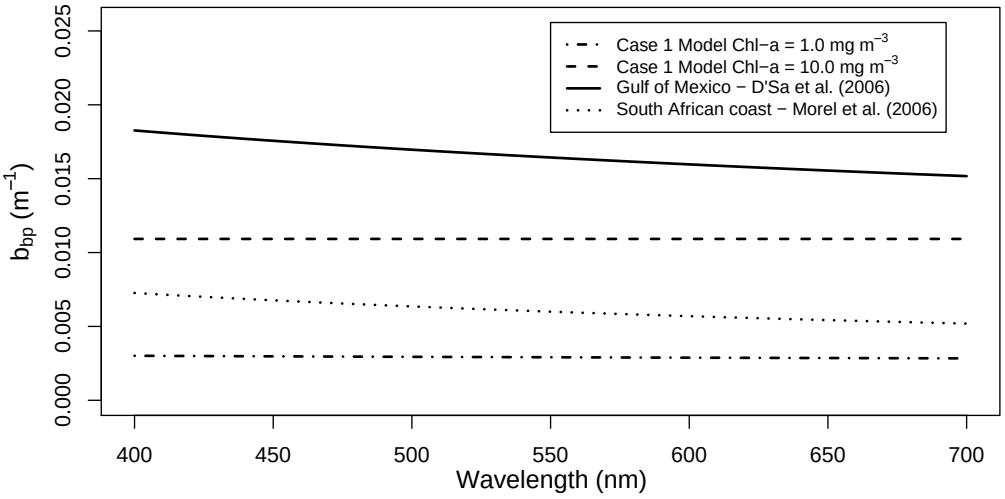

Figure 1.7: Particulate backscattering, b_{bp}, models and measurements based on case 1 water model (Morel and Maritorena 2001) at $chl = 1$ and 10 mg m^{-3} (dot-dashed and dashed, respectively), measured by D'Sa et al. (2006) (solid), and approximated from Morel et al. (2006) for CDOM dominant case 2 waters (dotted).

dominated by 0.45 - 200 μm particles to one dominated by 0.02 - 0.45 μm particles, scattering increases in the shorter blue wavelengths and decreases in the longer red wavelengths. Also, with increases in the particulate refractive index there is an increase in total scattering (Babin et al. 2003a). To illustrate these variables, several examples of both measured and modelled particulate backscattering spectra are provided in Fig. (1.7), including backscatter measured in the coastal waters of the Gulf of Mexico with $chl = 4.40$ mg m^{-3} (3.15 mg l^{-1} of suspended particulate) (D'Sa et al. 2006), CDOM dominated South African coastal waters with $chl \approx 4.0$ mg m^{-3} ($\sim$ 0.85 mg l^{-1} of suspended particulate) (Morel et al. 2006), and case 1 particulate backscatter models at *chl* concentrations of 1.0 and 10.0 mg m^{-3} (Morel and Maritorena 2001). As the coastal waters of the Gulf of Mexico have higher suspended particulate concentrations, higher particulate backscattering was measured. The CDOM dominant South African waters, on the other hand, had lower particulate concentrations for similar *chl* concentrations to the Gulf of Mexico and had particulate backscatter coefficients more consistent with the case 1 water models.

The relationship between particulate backscatter and particulate scattering can be important in modelling the apparent optical properties of a water body. While in certain situations the particulate backscattering to scattering ratio, $\tilde{b}_{bp}$, can have a wavelength dependence, Whitmore et al. (2007) noted that spectral variability was limited in most circumstances and $\tilde{b}_{bp}$ was found to be 0.013. A statistical relationship was found by D'Sa et al. (2006) between b_{bp} and b_p, suggesting that $\tilde{b}_{bp}$ varies with b_p. Although the relationship between b_p and $\tilde{b}_{bp}$ is generally independent of wavelength, it is likely dependent upon b_p.

Similar to the scattering properties of particles, their absorption properties can be significant in optically complex waters. Absorption related to particles with photosynthetic pigments removed is commonly referred to as non-algal particle absorption, $a_{NAP}(\lambda)$, and consists of the combined absorption from organic and inorganic particulate. In open ocean waters, such as the Atlantic Ocean, a_{NAP} is limited. However, in river influenced coastal waters, non-algal particulate absorption can be as high as absorption from CDOM (Fig. 1.8) (Babin et al. 2003b). In Fig. 1.8, the a_{NAP} in the North Sea is likely higher because of higher TSS concentrations ($0.4 \sim 80$ g m^{-3}) compared to the Baltic Sea ($1 \sim 6$ g m^{-3}) and the Altantic Ocean ($0.02 \sim 0.4$ g m^{-3}). The spectral shape of non-algal particle absorption typically follows an exponential curve similar to CDOM; except, with a different slope value. Due to this spectral similarity, non-algal particulate absorption is commonly grouped with CDOM absorption in semi-analytical algorithms (Carder et al. 1999, Maritorena et al. 2002, Lee et al. 2002)

In relation to the Strait of Georgia, suspended particles can be an optically significant constituent. As shown through airborne multispectral video by Liedtk et al. (1995), the suspended particulate concentrations in the Fraser River plume were highly correlated ($r^2 = 0.945$) with reflectance in the red portion of the spectrum. The spatial and seasonal patterns of the particles were also studied by Johannessen

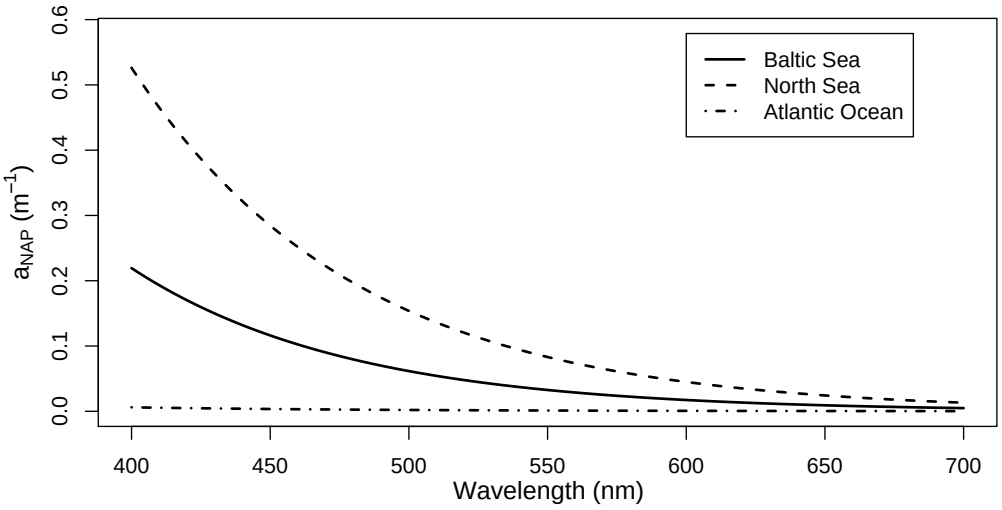

Figure 1.8: Non-algal particle absorption, a_{NAP}, curves fitted to sample measurements by Babin et al. (2003b) for the Baltic Sea (solid), North Sea (dash), and Atlantic Ocean (dot-dash).

et al. (2006) using a transmissometer measuring at 660 nm. In that study, it was found that surface waters of the Strait were turbid during late summer and early autumn with the waters becoming clearer during the winter. During autumn conditions, it was found that particulate concentrations were more dispersed throughout the Strait and not as well associated with the Fraser River plume. These higher particulate concentrations can have a significant impact on *chl* and near-infrared (NIR) atmospheric correction used to produce standard *chl* images, as will be discussed in Chapter 2 and 3, respectively.

1.4.4 Chromophoric Dissolved Organic Matter

Chromophoric dissolved organic matter, or CDOM, results from the breakdown of organic matter into humic and fluvic acids and is measured as the absorption from the component in the water $< 0.2\mu$m (Bricaud et al. 1981, Carder et al. 1989). In case 1 waters, CDOM is assumed to result from *in situ* primary productivity, so absorption from CDOM should vary proportionally with *chl* concentrations (Carder et al. 1989, Twardowski and Donaghay 2001). In case 2 waters, CDOM is not assumed

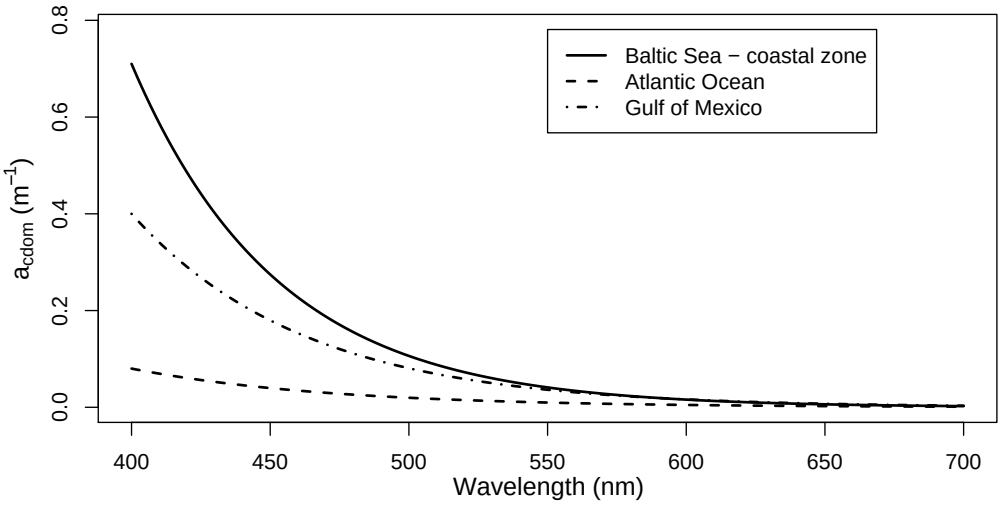

Figure 1.9: CDOM absorption curves measured by Kowalczuk et al. (2005) in the Baltic Sea coastal zone (solid), Babin et al. (2003b) in the Atlantic Ocean (dashed), and D'Sa et al. (2006) in the Mississippi River influenced Gulf of Mexico (dot-dashed).

to vary linearly with *chl* concentrations because of inputs from terrestrial sources (Twardowski and Donaghay 2001).

CDOM absorption has a consistent spectral shape, the properties of which have been reviewed in several studies (Bricaud et al. 1981, Carder et al. 1989, Twardowski et al. 2004). Examples of CDOM absorption characteristics in several water bodies are provided in Fig. (1.9), include coastal waters (Baltic Sea and Gulf of Mexico) and open ocean (Atlantic). CDOM absorption is greater in the blue wavelengths compared to green, increasing the blue-green ratio commonly used with empirical *chl* algorithms (Sathyendranath et al. 2001).

In the Strait of Georgia, higher CDOM absorption is expected due to terrestrial runoff, the relative shallowness of the Strait around the shores, the decomposition of phytoplankton cells, and the limited exchange with open ocean waters (Twardowski and Donaghay 2001).

1.5 Thesis Methods

Methods related to the bio-optical algorithm evaluations are provided in Chapter 2 (Section 2.3), while the atmospheric correction evaluation methods are presented in Chapter 3 (Section 3.3). Coordinates for sampling stations used in the bio-optical algorithm evaluation are provided in Appendix B.

At several stations listed in Appendix B, multiple above-water reflectance measurements were taken and the individual measurements are plotted for each station in Appendix C. For the bio-optical algorithm study in Chapter 2, the average of all the spectra at a station was used to represent the station.

Chl measurements used to evaluate the algorithms were collected using the method described in Chapter 2 and are provided in Appendix E. On each day of the cruise, three blank filters were collected with filtered deionized water and are represented by Station Names as 'BlankXXXX' with XXXX representing the month and day of collection. At several stations, multiple samples were collected and are provided in columns 'Samples 1 - 3' with the mean and standard deviation of the samples provided in the 'Mean' and 'Std.' column, respectively. Lab duplicates were also processed, which are station samples that were measured a second time by the High Performance Liquid Chromatography (HPLC) instrument. Lab duplicates are identified by the station name with the suffix '(Lab Dup.)' and provide estimate of replicability of the instrument. In addition to replicates from a single cast, at a few stations a second cast was collected and are identified as '(Cast 2)'.

CDOM absorption was measured from the filtrate of a sample that sequentially passes through a 0.7 μm and 0.2 μm filter. Unlike *chl* samples, triplicate CDOM samples were only collected during the April cruise and only single samples were collected during the July cruise due to logistic and time constraints (Appendix D). Single blank samples were collected each day and are represented by the station names

'BlankXXXX' with XXXX representing the month and day of collection. Absorption measurements associated with the July samples are more accurate than those collected in April. This is related to increasing the integration time of measurements with the spectrophotometer and increasing the precision of the output from the spectrophotometer software package.

Total suspended solid (TSS) measurements are provided in Appendix F and includes multiple samples at each station. Similar to the *chl* samples, multiple casts were collected and these additional casts are identified as '(Cast 2)'.

At several stations, such as the July TSS concentration at station 'S2-3', large variability was observed between replicates. This large variability may be related to the configuration of sample bottles during collection. To collect the three litres of water for a given sample, two 5 l Niskin bottles need to be deployed in close succession to collect three samples in a single cast. With the bottles having an approximate length of 70 cm, there can be nearly 1 m between bottle centres that would represent the surface water sample. The close grouping of two samples and a single sample with a drastically different value could be explained by two samples usually collected from one Niskin bottle and a single sample collected from the second bottle. With no way to identify samples with the appropriate Niskin bottle, the mean of all the samples at a station were taken.

Chapter 2

Bio-optical algorithm evaluation for MODIS for western Canada coastal waters: an exploratory approach using *in situ* reflectance

2.1 Introduction

The use of satellite imagery has proven effective for deriving biophysical variables in optically deep waters dominated by phytoplankton at temporal and spatial scales difficult to attain with direct field measurements (Sathyendranath et al. 2004b). Chlorophyll-a (*chl*) concentrations have typically been the main biophysical variable derived from ocean-colour imagery. When estimating *chl* concentrations, algorithms are commonly empirical or semi-analytical based. Empirical approaches rely on a specific spectral feature, such as a spectral ratio modelled to biophysical measurements using statistical regression. Semi-analytical algorithms rely on greater knowledge of the optical properties of the water column and try to isolate the spectral influence of several optical variables (IOCCG 2006).

Historically, research has focused on developing *chl* algorithms for ocean-colour

imagery of open-ocean waters, typically referred to as case 1 waters (IOCCG 2000). With case 1 waters, *chl* is assumed to be the dominant optical constituent and all other optical constituents are limited or co-vary with *chl* concentrations. In coastal terrestrially influenced water bodies, all major optical constituents, including suspended particles and chromophoric dissolved organic matter, can vary independently. These regions are more commonly classified as case 2 waters (Gordon and Morel 1983). Algorithms developed for open-ocean waters typically do not perform well in these optically complex case 2 waters. To accommodate coastal environments, algorithms based on case 1 waters need to be evaluated and possibly modified (IOCCG 2000, Darecki and Stramski 2004, Gower et al. 2005, Garcia et al. 2005).

In addition to the optical complexity of case 2 water, ocean-colour *chl* algorithms have shown reduced performance in open water conditions with latitudes above $\sim 50^{\circ}$ (IOCCG 2000). In these regions, phytoplankton community composition impacts the specific absorption properties with varying accessory pigments and pigment packaging effects. Phytoplankton typically found at higher latitudes, such as diatoms, have lower specific absorption properties in the blue portion of the spectrum compared to phytoplankton at lower latitudes (Sathyendranath et al. 2001).

The Strait of Georgia, located between Vancouver Island and the mainland of British Columbia, is an area of environmental and economic importance to the west coast of Canada. The Strait is a large estuary-like coastal basin with several tributaries, bays, inlets, and sounds. The tributaries provide both freshwater and suspended material, the largest source of which is the Fraser River (Johannessen et al. 2003). Terrestrial inputs coupled with nutrient-rich deep water from the Pacific Ocean and mixing forces produce a highly productive seasonal system (Li et al. 2000).

Links between physical and biological dynamics in the Strait have been the focus of current research (Collins 2005, Masson 2006). However, these studies are primarily based on ship measurements. The broad spatial scale and temporal frequency of

ocean-colour sensors, such as the Moderate Resolution Imaging Spectroradiometer (MODIS) instrument on the NASA Aqua satellite, may provide a consistent observational platform to gain insight into the relationship between physical and biological processes (Harrison et al. 1983, Li et al. 2000).

With these needs in mind, the focus of this study was the evaluation of ocean-colour algorithms for estimating *chl* concentrations in the Strait of Georgia. The following algorithms were evaluated: the empirical OC3M (O'Reilly et al. 2000), semi-analytical Garver-Siegel-Maritorena version 1 (GSM01) (Maritorena et al. 2002), and a modified GSM01. The OC3M algorithm was selected because of its common use in global *chl* monitoring. The GSM01 algorithm was selected because it can easily be modified for use in other applications, such as for specific coastal waters, by changing the individual bio-optical components (Magnuson et al. 2004, IOCCG 2006). Modifications to the GSM01 algorithm focused on the inherent optical properties used with the algorithm. Biophysical measurements and *in situ* hyperspectral radiometric measurements modelled to MODIS spectral bands were used to evaluate the various algorithms. In addition to evaluating these algorithms, different inherent optical property (IOP) models were evaluated for use with the GSM01 algorithm.

2.2 Bio-optical Algorithm Background

2.2.1 OC3M Algorithm

The empirical OC3M algorithm is extended from the OC4 and OC2 algorithms developed for the SeaWiFS sensor and adapted to the spectral bands of MODIS. The algorithm is statistically derived based on *chl* concentrations ranging from 0.0008 to 90 mg m^{-3}. However, most of the measurements have concentrations between 0.08 and 3 mg m^{-3} (O'Reilly et al. 2000, Bailey and Werdell 2006). Standard *chl* concentration images produced by NASA's Ocean Color Group using MODIS imagery are based on the OC3M algorithm, defined as

$$Chl = 10.0^{\left(0.2830 - 2.753R_{3M} + 1.457R_{3M}^2 + 0.659R_{3M}^3 - 1.403R_{3M}^4\right)} \tag{2.1}$$

$$R_{3M} = log_{10}\left(\frac{max[R_{rs}(443), R_{rs}(488)]}{R_{rs}(551)}\right) \tag{2.2}$$

where max specifies the greater of the two values and R_{3M} is the band ratio that emphasizes the absorption by *chl* in the blue wavelengths in relation to green reflectance.

2.2.2 GSM01 Algorithm

The GSM01 algorithm uses a Levenberg-Marquardt nonlinear least-squares procedure to fit modelled to measured remote-sensing reflectance (Maritorena et al. 2002). To derive modelled remote-sensing reflectance at a particular wavelength, $\hat{R}_{rs}(\lambda)$, a semi-analytical model is used (Gordon et al. 1988b) and is defined as

$$\hat{R}_{rs}(\lambda) = \mathfrak{R}\frac{f'}{Q}\left(\frac{b_b(\lambda)}{b_b(\lambda) + a(\lambda)}\right) \tag{2.3}$$

where the $\mathfrak{R}$, f', and Q represent the air-water interface, the transition from the quasi-single-backscatter albedo to subsurface upwelling irradiance, and the angular distribution of the upwelling irradiance, respectively. The f'/Q term varies with viewing geometry and inherent optical properties (IOPs) properties, such as the volume scattering function (Morel et al. 2002, Loisel and Morel 2001, Park and Ruddick 2005). In the standard GSM01 algorithm, these terms are set to a quadratic formula (Eq. (2.4)) with $g_i = (0.0949, 0.0794)$ and represent the remote-sensing reflectance below the air-water interface, $r_{rs}(\lambda)$, as defined in Eq. (2.5).

$$\frac{f'}{Q}\left(\frac{b_b(\lambda)}{b_b(\lambda) + a(\lambda)}\right) = \sum_{i=1}^{2} g_i \left(\frac{b_b(\lambda)}{b_b(\lambda) + a(\lambda)}\right)^i \tag{2.4}$$

$$r_{rs}(\lambda) = \frac{f'}{Q}\left(\frac{b_b(\lambda)}{b_b(\lambda) + a(\lambda)}\right) \tag{2.5}$$

While the $\mathfrak{R}$ term in Eq. (2.3) varies with wind speed and wavelength at solar zenith angles $> 60°$ (Gordon 2005, Wang 2006b), the relationship described by Lee et al. (1999) and shown in Eq. (2.6) was used to relate above-water remote-sensing reflectance, $R_{rs}(\lambda)$, to remote-sensing reflectance below the air-water interface.

$$R_{rs}(\lambda) = \frac{0.52 r_{rs}(\lambda)}{1 - 1.7 r_{rs}(\lambda)} \tag{2.6}$$

$b_b(\lambda)$ and $a(\lambda)$ in Eq. (2.3) represent the total backscatter and absorption properties of the water column, respectively. Estimation of the influence from each optical constituent is dependent upon the assumption that each constituent maintains consistent spectral characteristics and is vertically homogeneous in the upper portion of the water column. The combined influence of the optical constituents on $\hat{R}_{rs}(\lambda)$ are described through Eq. (2.3), (2.7), and (2.8).

$$b_b(\lambda) = b_{bw}(\lambda) + b_{bp}(\lambda) \tag{2.7}$$

$$a(\lambda) = a_w(\lambda) + a_{ph}(\lambda) + a_{dg}(\lambda) \tag{2.8}$$

In the GSM01 algorithm, the IOPs of phytoplankton absorption, $a_{ph}(\lambda)$, particulate backscatter, $b_{bp}(\lambda)$, and the combined absorption of non-algal particles and chromophoric dissolved organic matter, $a_{dg}(\lambda)$, are defined by Eq. (2.9), (2.10), and (2.11), respectively. The absorption and backscatter of water are represented by $a_w(\lambda)$ and $b_{bw}(\lambda)$, respectively. The coefficients for water absorption are provided by Pope and Fry (1997) and backscatter are provided by Smith and Baker (1981).

$$a_{ph}(\lambda) = Chl\ a^*_{ph}(\lambda) \tag{2.9}$$

$$b_{bp}(\lambda) = b_{bp}(\lambda_0)(\lambda/\lambda_0)^{-\eta} \tag{2.10}$$

$$a_{dg}(\lambda) = a_{dg}(\lambda_0) exp[-S_{cdom}(\lambda - \lambda_0)] \tag{2.11}$$

Table 2.1: Phytoplankton specific absorption coefficients (a^*_{ph}) used in conjunction with Eq. (2.9) to estimate *chl* concentrations (Maritorena et al. 2002). Wavelengths are based on SeaWiFS bands and are linearly interpolated to MODIS band centres.

Wavelength (nm)	412	443	490	510	555	670
$a^*_{ph}(\mathrm{m}^2(\mathrm{Chl\ mg})^{-1})$	0.00665	0.05582	0.02055	0.01910	0.01015	0.01424

The standard GSM01 algorithm defines the values of S_{cdom}, η, and $a^*_{ph}(\lambda)$ as constants, which represent the exponential absorption slope of CDOM and non-algal particles, the power law distribution for particulate backscatter, and the specific absorption properties of phytoplankton, respectively. All of these values were estimated by Maritorena et al. (2002) using a simulated annealing approach from a global data set. To model the optical constituents to remote-sensing reflectance, the standard GSM01 algorithm uses 443 nm as a reference wavelength (λ_0), an S_{cdom} of 0.0206 nm^{-1} and an η of 1.0337. The values for $a^*_{ph}(\lambda)$ based on SeaWiFS bands (Table 2.1) are linearly interpolated to MODIS band centres.

2.3 Methods

Biophysical and radiometric measurements, collected during two research cruises on the *R/V John Strickland*, were used to evaluate the OC3M, standard GSM01, and modified GSM01 algorithms. The two cruises were carried out in late April (early spring) and early July (summer) in 2006, sampling the stations shown in Fig. 2.1. At each station above-water hyperspectral radiometric measurements were acquired and subsurface water samples collected to measure *chl* concentration, CDOM absorption (a_{cdom}), and total suspended solid (TSS) concentrations. Above-water remote-sensing reflectance was derived from spectral measurements and modelled to the spectral bands of MODIS (see below).

2.3.1 Optical Measurements

Above-water radiometric measurements were taken with a Satlantic HyperSAS instrument package, which includes a sea surface radiance ($L_t(\lambda)$), sky radiance ($L_s(\lambda)$),

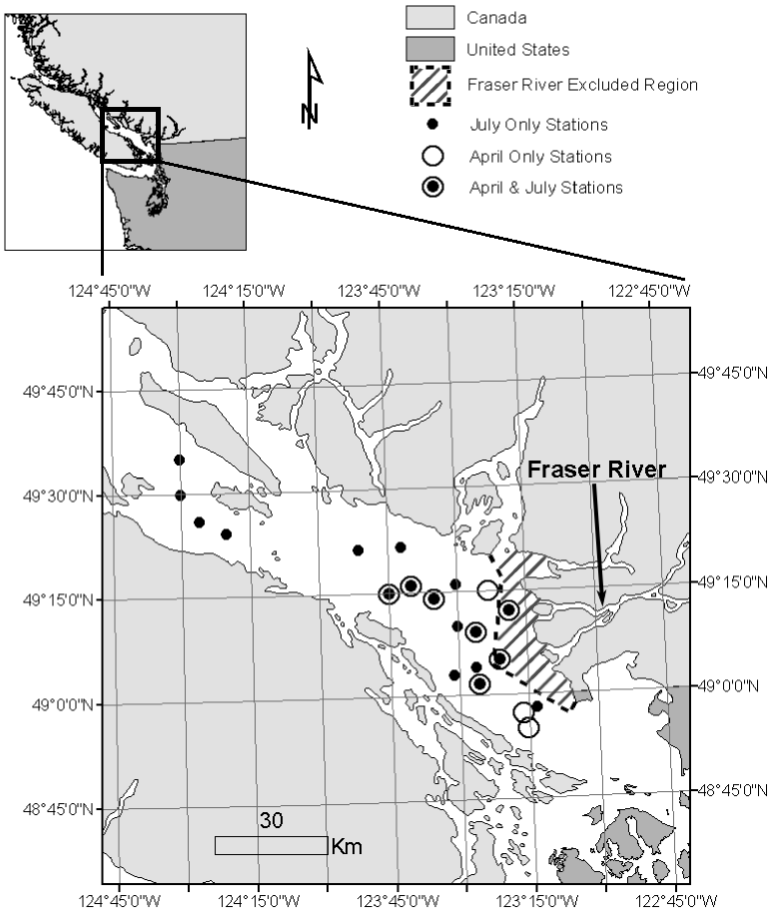

Figure 2.1: Sampling stations in the Strait of Georgia used in this study. The shaded area identifies the Fraser River exclusion region that were excluded when evaluating the Fraser River plume influence.

and sky irradiance ($E_s(\lambda)$) sensor. With each radiometric acquisition, effort was made to maintain a fixed geometry with the vessel bow or stern pointed at the sun, the instrument at a 90° azimuth, and the L_t sensor at a 40° angle from nadir (Mobley 1999). At each station, approximately 2 to 3 minutes of radiometric measurements were acquired and the lowest 5% reflectance in the NIR were used to produce an average reflectance spectrum (Hooker and Morel 2003). Radiometric measurements were converted to above-water remote-sensing reflectance, $R_{rs}(\lambda)$, according to Eq. (2.12), (2.13), and (2.14) (Ruddick et al. 2006).

$$R_{rs}(\lambda) = \frac{L_t(\lambda) - \rho_{sky} L_s(\lambda)}{E_s(\lambda)} \tag{2.12}$$

$$\rho_{sky} = 0.0256 + 0.00039W + 0.000034W^2, \text{when} \frac{L_s(750)}{E_s(750)} < 0.05 \tag{2.13}$$

$$\rho_{sky} = 0.0256, \text{when} \frac{L_s(750)}{E_s(750)} \geq 0.05 \tag{2.14}$$

The ρ_{sky} value represents the proportion of sky radiance that is reflected off the surface of the water and is dependent upon wind speed, W, and the proportion of cloud cover in the sky radiance measurements, as identified by the ratio $L_s(750)/E_s(750)$. Under clear sky conditions, $L_s(750)/E_s(750) < 0.05$, the ρ_{sky} value varies based on the water surface roughness and the associated increase in bright reflections off the water surface. For cloudy conditions, $L_s(750)/E_s(750) \geq 0.05$, the sky is more uniform and there is limited glint, resulting in ρ_{sky} being independent of the wind speed (Mobley 1999, Ruddick et al. 2006).

To limit variability in the water-leaving radiance related to the air-water interface at higher solar zenith angles, radiometric measurements were limited to those taken

with a solar zenith angle less than 60° (Gordon 2005, Wang 2006b). In addition to the solar zenith angle criteria, two stations were excluded from this analysis, one due to an excessively rough water surface and another due to negative reflectance at 700 nm. The negative refletance is likely related to an overestimation of the ρ_{sky} in Eq. (2.12) due to cloud or wind variability at the station. A total of 28 stations were used in this study.

The final hyperspectral remote-sensing reflectance measurements were modelled to the spectral bands of the MODIS Aqua sensor using spectral response functions provided by NASA Ocean Color Group website (http://oceancolor.gsfc.nasa.gov/DOCS/RSR_Tables.html) and a weighted mean approach.

2.3.2 Biophysical Measurements

To measure CDOM absorption, a_{cdom}, samples were filtered with a prepared 0.2 μm Pall© filter and the filtrate frozen in amber bottles for the remainder of the cruise. The 0.2 μm filters were prepared by filtering 250 ml of deionized water and drying the filter at 100°C for an hour. Absorption properties of the filtrate were measured using an Ocean Optics 2000USB spectrophotometer with a 100 mm cuvette and deionized water as a reference sample. CDOM absorption data was processed using the methods defined by Pegau et al. (2003), which included the conversion from absorbance to absorption and the removal of offsets. To remove offsets from the final measurements, the average absorption coefficient from 690 to 710 nm was subtracted from all wavelengths. Absorbance, $A(\lambda)$, measured by the spectrophotometer was converted to absorption, $a(\lambda)$, using Eq. (2.15) with a path length, ℓ, of 100 mm.

$$a(\lambda) = 2.303\ A(\lambda)/\ell \tag{2.15}$$

Determination of total suspended solid (TSS) concentrations was accomplished

using a gravimetric method. Each TSS water sample of 1 to 3 litres was filtered with a prepared 0.7 μm Whatman GF/F filter. After the sample was filtered, 50 ml of deionized water was filtered to remove salts. The filters were then stored for the remainder of the cruise. To prepare filters, 250 ml of deionized water was filtered and the filters were heated to 450°C for an hour to dry and remove any remaining organic matter. Following the cruise, each filter was dried at 60°C for several hours, until the weight stabilized (Clesceri et al. 1998).

Chl samples were collected by filtering 1 to 3 litres of water through a 0.7 μm Whatman GF/F filter. *Chl* samples were filtered on the day of collection and the resulting filters frozen at -20°C until the samples were processed. In the lab, pigments were extracted by macerating the filter in a 90% acetone solution under low light conditions, allowed to sit overnight at -20°C, and centrifuged the following day to remove filter fibres. The samples were processed using High Performance Liquid Chromatography (HPLC) with an eluent gradient defined by Arar (1997) and modified to improve peak separability.

2.3.3 GSM01 Modifications

The GSM01 algorithm implemented in the SeaDAS version 5.0 software package (Baith et al. 2001) was modified for use in this study. Modifications include the use of a different CDOM absorption model and a reinterpretation of phytoplankton absorption for higher latitude waters to estimating *chl* concentrations.

To modify the CDOM absorption characteristics, the spectral model of CDOM in Eq. (2.11) was replaced with the relationship defined by Twardowski et al. (2004), as

$$a_{cdom}(\lambda) = a_{cdom}(\lambda_0)\left(\frac{\lambda}{\lambda_0}\right)^{-6.92} \tag{2.16}$$

Samples from several water bodies, including Fraser River-influenced waters, were

used to develop this CDOM absorption model. While the Twardowski et al. (2004) model is based on a reference wavelength (λ_0) of 412 nm, the reference wavelength was set to 443 nm for comparison with the model defined by the standard GSM01 algorithm. It is important to note that the Twardowski et al. (2004) model is based on only absorption by CDOM and that the GSM01 algorithm uses the model to estimate the combined absorption of CDOM and non-algal particles. However, CDOM absorption typically dominates over non-algal particles in coastal waters with limited turbidity (Darecki et al. 2003, D'Sa et al. 2006).

Prior to implementing the CDOM absorption modification in the GSM01 algorithm, the suitability of the several CDOM models was evaluated. This evaluation compared the following models: (i) the Twardowski et al. (2004), (ii) the standard CDOM absorption exponential curve with $S_{cdom} = 0.0206$ nm^{-1}, (iii) and the exponential absorption curve with a more common S_{cdom} value of 0.015 nm^{-1} (Lee et al. 2002). These CDOM absorption curves were compared to CDOM absorption measurements collected during this study with absorption coefficients selected at MODIS band centres.

In addition to modifying the CDOM model, the estimated phytoplankton absorption, a_{ph}, from the modified GSM01 algorithm was re-evaluated using a two-component phytoplankton absorption model developed by Devred et al. (2006). This model defines the combined absorption of two phytoplankton populations, a background population with higher specific absorption coefficients (a_1^*) and a bloom population with lower coefficients (a_2^*). The transition between the specific absorption properties of the two populations is associated with *chl* concentration using

$$a_{ph}(\lambda) = C_1^m[a_1^*(\lambda) - a_2^*(\lambda)][1 - \exp(-S_{ph}\ Chl)] + a_2^*(\lambda)\ Chl \qquad (2.17)$$

where S_{ph} is a constant that specifies the transition between the two populations using an exponential relationship and C_1^m represents the maximum *chl* concentra-

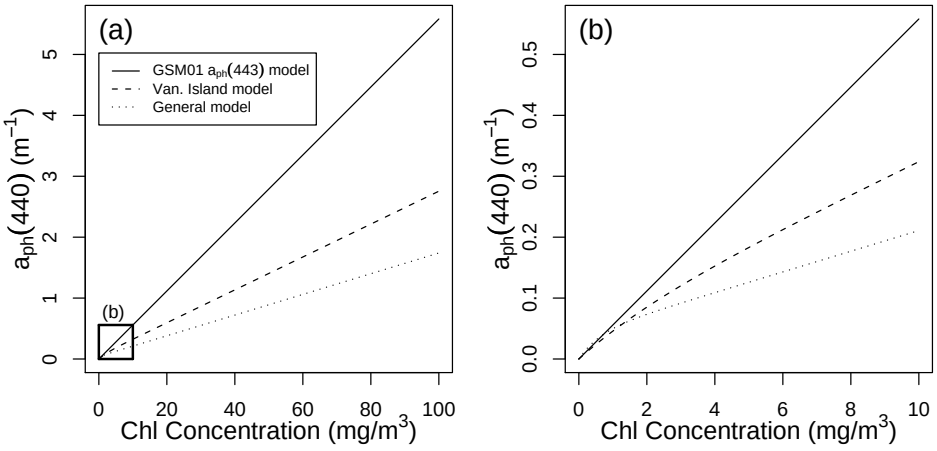

Figure 2.2: Modelled phytoplankton absorption, $a_{ph}(440)$, in relation to *chl* concentrations for the standard GSM01 algorithm (solid line), the Vancouver Island two-component (dashed line), and the general two-component models (dotted line). Two *chl* ranges are provided, (a) from 0 to 100 mg m^{-3} and (b) 0 to 10 mg m^{-3}.

tion of the background smaller cell population. For this study, two versions of this model were evaluated. The first version (henceforth called the Vancouver Island two-component model) was developed using samples collected by Devred et al. (2006) in the waters off Vancouver Island and has the values $C_1^m = 2.38$ mg m^{-3}, $S_{ph} = 0.42$, $a_1^*(440) = 0.050$ $m^2(Chl$ $mg)^{-1}$, and $a_2^*(440) = 0.027$ $m^2(Chl$ $mg)^{-1}$. The second version (henceforth called the general two-component model) is based on *chl* measurements for the Arabian Sea, Northwest Atlantic, Vancouver Island, and Chilean coast with $C_1^m = 0.62$ mg m^{-3}, $S_{ph} = 1.61$, $a_1^*(440) = 0.083$ $m^2(Chl$ $mg)^{-1}$, and $a_2^*(440) = 0.017$ $m^2(Chl$ $mg)^{-1}$ (Devred et al. 2006).

The variability of $a_{ph}(440)$ in relation to *chl* concentrations for the standard GSM01, Vancouver Island two-component, and general two-component models are shown in Fig. 2.2. To apply the two-component models to the modified GSM01 algorithm, $a_{ph}(440)$ of the models was taken as equivalent to $a_{ph}(443)$ from the modified GSM01 algorithm.

The Vancouver Island two-component model has a nonlinear transition in $a_{ph}(440)$ from higher specific absorption coefficients of the background phytoplankton popu-

lation to lower specific absorption of the bloom population (Fig. 2.2(b)). This is contrasted by the linear relationship of $a_{ph}(443)$ in the GSM01 algorithm. The non-linear transition is also observed with the general two-component model, except at a lower range of *chl* concentrations ($0 \sim 2$ mg m^{-3}). The different specific absorption properties associated with the Vancouver Island compared to the general model is due to diatom blooms in the Vancouver Island samples. In other regions sampled by the Devred et al. (2006) study, smaller phytoplankton cells more commonly associated with oligotrophic waters and with lower specific absorption coefficients, compared to the Vancouver Island samples, were found.

To utilize the two-component phytoplankton absorption models, $a_{ph}(443)$ was estimated using Eq. (2.9) and the *chl* concentration from the modified GSM01 algorithm. The $a_{ph}(443)$ was then re-evaluated using a look-up table (LUT) based on the two-component model. A corresponding *chl* concentration was then identified for the $a_{ph}(443)$ value from the modified GSM01 algorithm. The LUT was generated with *chl* values ranging from 0 to 100 mg m^{-3} with 0.1 mg m^{-3} steps and the corresponding $a_{ph}(440)$ calculated from Eq. (2.17) for each of the two previously defined two-component models.

2.3.4 Algorithm Evaluation

To evaluate results of the algorithms in relation to measured biophysical values, the Root-Mean-Square-Error ($RMSE$) defined as Eq. (2.18) was calculated (IOCCG 2006). In addition to $RMSE$, the Relative Percent Difference (RPD) and Absolute Difference (AD) defined in Eq. (2.19) and (2.20), respectively, were used to evaluate IOP models.

$$RMSE = \left(\frac{\sum_{i=1}^{N} [\log_{10}(\chi_i^{model}) - \log_{10}(\chi_i^{true})]^2}{n-2} \right)^{1/2} \tag{2.18}$$

$$RPD = \frac{\chi^{model} - \chi^{true}}{\chi^{true}} \tag{2.19}$$

$$AD = |\chi^{model} - \chi^{true}| \tag{2.20}$$

χ^{model} and χ^{true} represent the modelled and measured biophysical values, respectively, and n is the number of samples. When summarizing a model's fit, the absolute RPD was used for calculating the mean to avoid offsetting positive and negative values from cancelling out errors in the model's fit. For this study, statistical significance is taken as a confidence level greater than 95%.

When evaluating the OC3M and GSM01 algorithms, considerations were made for the influence from the Fraser River plume, because high turbidity was expected to influence *chl* estimates (Woźniak and Stramski 2004). The OC3M algorithm was evaluated with all stations and without stations directly under the influence of the Fraser River. Stations removed are identified in the shaded region on Fig. 2.1, which corresponds to an approximate 4 km buffer from the Fraser River delta tidal banks representing the most turbid region of the plume (Kostaschuk et al. 1993). To limit the Fraser River influence on the modified GSM01 algorithm, the advantage of additional IOP estimates from the algorithm was used and thresholds on estimated $a_{dg}(443)$ and $b_{bp}(443)$ were evaluated. This approach should identify the transition from less turbid conditions of the Strait to Fraser River-influenced regions with greater terrestrial influence.

2.4 Results

2.4.1 Field Data

Results showed a range of conditions in the biophysical properties of the Strait of Georgia, from the central portions of the Strait characterized by lower $a_{cdom}(443)$

Table 2.2: Field measured minimum-maximum(mean) values from cruise data of surface samples used in this study.

Dates	n	TSS (g m^{-3})	Chl (mg m^{-3})	$a_{cdom}(443)$ (m^{-1})
Apr 25 - 28	10	2.65-11.88(5.06)	0.55-5.13(2.61)	0.21-0.79(0.44)
July 12 - 17	18	1.53-15.24(3.77)	0.39-8.46(3.74)	0.22-0.40(0.32)

(0.22 - 0.48 m^{-1}) and TSS concentrations (1.76 - 3.47 g m^{-3}), to significant terrestrial influence closer to the Fraser River plume with relatively higher $a_{cdom}(443)$ (0.21 - 0.79 m^{-1}) and TSS concentrations (1.53 - 15.24 g m^{-3}) (Fig. 2.1). *Chl* concentrations were found to have the greatest variability in the southern portion (0.39 - 8.46 mg m^{-3}) compared to the central portion (1.55 - 6.48 mg m^{-3}). Table 2.2 summarizes these results.

Maximum *chl* concentrations during the cruises were found to be lower than concentrations found in other studies in this region (Harrison et al. 1983, Li et al. 2000), which is likely related to the timing of the cruises missing spring bloom conditions in the surface waters. However, the *chl* concentration range from this study was similar to that found in summer surface waters in other studies of the Strait (1.91 - 6.87 mg m^{-3}) (Radi et al. 2007). During the April 2006 cruise, the highest surface *chl* concentrations were found at the two southern most stations with concentrations of 3.94 and 5.13 mg m^{-3}. In July, the highest *chl* concentrations were west of the Fraser River plume with concentrations ranging from 5.99 to 8.46 mg m^{-3}.

Concentrations of TSS in the central portions of the Strait were higher than those found in more open-ocean waters (0.59 $\sim$ 2.84 g m^{-3}) (Tilstone et al. 2005) and similar to other river influenced regions (0.99 $\sim$ 7.24 g m^{-3}) (D'Sa et al. 2006). At the stations closest to the Fraser River exclusion region, TSS concentrations (6.72 - 15.24 g m^{-3}) were similar to those found in past studies of the Strait (5 $\sim$ 200 g m^{-3}) (Kostaschuk et al. 1993). Central Strait CDOM absorption properties at 443 nm were higher than those found in more open-waters ($<$ 0.01 $\sim$ 0.13 m^{-1}) (Morel et al. 2006) and open-waters under terrestrial influence (0.07 - 0.21 m^{-1}) (D'Sa et al.

2006). The average CDOM absorption in the Strait ($a_{cdom}(443) = 0.36$ m^{-1}) was similar to that found in coastal areas of the Baltic Sea during summer, with a mean $a_{cdom}(443) = 0.31$ m^{-1} (Kowalczuk et al. 2005), and comparable to measurements by Twardowski and Donaghay (2001) in the southern portion of the Strait ($0.16 \sim 0.32$ m^{-1}).

Comparison of absorption properties from individual IOPs is a general approach to classifying the dominant optical constituent and the type of water mass (Prieur and Sathyendranath 1981, IOCCG 2000). Using the Devred et al. (2006) model in Eq. (2.17) with the Vancouver Island two-component model, for an average *chl* concentration of 3.34 mg m^{-3}, the estimated $a_{ph}(440)$ was 0.13 m^{-1}. The average measured $a_{cdom}(443)$ was 0.36 m^{-1}, which indicates that CDOM absorption dominates over phytoplankton absorption, thus classifying the Strait as a case 2 water. Although there was no non-algal particulate absorption measurements, based on the higher TSS concentrations near the Fraser River, waters in the Strait likely transition from CDOM dominant case 2 waters in the central Strait to suspended particulate dominant case 2 waters at the mouth of the Fraser River.

2.4.2 CDOM Model Evaluation

As mentioned in Section 2.3.3, CDOM absorption models were evaluated before implementing the modified GSM01 algorithm. The relative percent difference (RPD) and absolute difference (AD) between measured CDOM absorption and the three CDOM models (Twardowski et al. (2004), standard GSM01, and Lee et al. (2002)) are provide in Table 2.3 and Fig. 2.3.

The CDOM absorption model in the standard GSM01 algorithm does not match measured absorption coefficients with a mean absolute difference of 0.045 m^{-1} and a mean absolute RPD of 27.5% (Table 2.3). The Twardowski model had the best fit to measured a_{cdom} of the three models with a mean absolute RPD of 2.0% and AD of 0.003 m^{-1}, compared to the Lee model with a mean absolute RPD and AD

Table 2.3: Deviation of measured CDOM absorption from several models using MODIS band centres based on the mean Absolute Difference (AD) and the mean absolute Relative Percent Difference (RPD) in the 412 to 551 nm range.

Model	AD (m^{-1})	Absolute RPD (%)
Twardowski Model	0.003	2.0
Lee Model ($S_{cdom} = 0.015$ nm^{-1})	0.009	5.9
Standard GSM01 ($S_{cdom} = 0.0206$ nm^{-1})	0.045	27.5

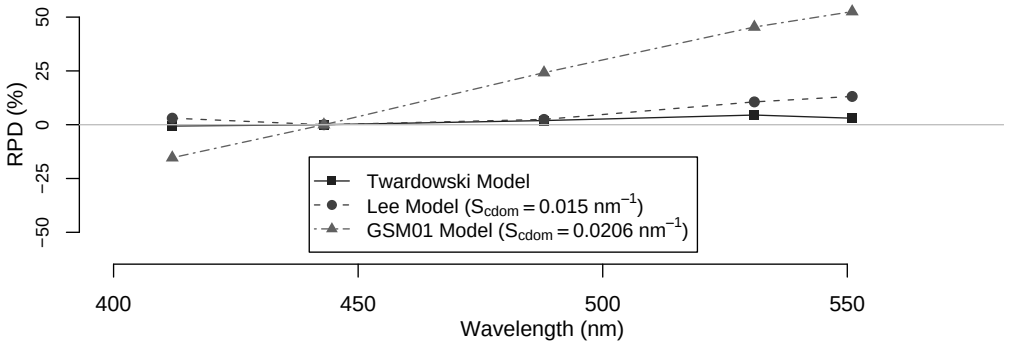

Figure 2.3: Comparison of CDOM models with CDOM absorption measurements based on MODIS Aqua bands. The models are compared to measured values using the Relative Percent Difference (RPD) (Eq. (2.19)).

of 5.9% and 0.009 m^{-1}, respectively.

2.4.3 Algorithm Evaluation

Statistical results of the OC3M, standard GSM01, and modified GSM01 algorithms in relation to biophysical measurements are summarized in Tables (2.4), (2.5), and (2.6), respectively.

The OC3M algorithm provided an $r^2 = 0.345$ when *chl* estimates were compared to measured concentrations (Fig. 2.4 and Table 2.4). Removing stations in the direct vicinity of the Fraser River tidal region (Fig. 2.1) improved *chl* estimates with an $r^2 = 0.552$ and a lower $RMSE$ was observed (Table 2.4). However, overestimation of lower *chl* concentrations was still observed. This overestimation was similarly observed in the Baltic Sea where *chl* concentrations vary from 0.3 to 100 mg m^{-3} (Darecki and Stramski 2004). This may be related to similar mean CDOM absorption

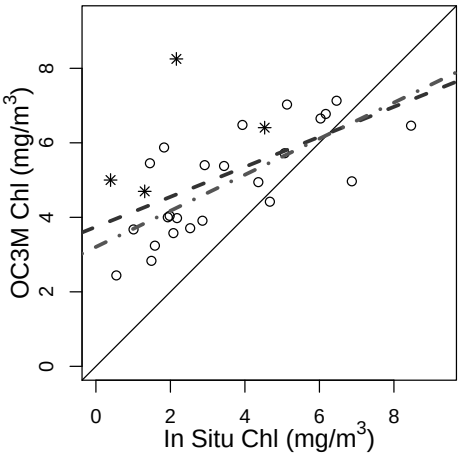

Figure 2.4: Comparison of OC3M algorithm and measured *chl* concentrations. Stars are stations within the Fraser River exclusion region east of the dashed line in Fig. 2.1. The dashed line is the line of best fit for all stations and the dot-dashed line is the best fit with Fraser River points excluded.

Table 2.4: Results of the OC3M algorithm compared with measured *chl* concentrations for all stations and stations in the Fraser River area excluded (Fraser River Exc.).

	n	r^2	p-value	$RMSE$	intercept	slope
OC3M (All Stations)	28	0.345	0.001	0.391	3.744	0.403
OC3M (Fraser River Exc.)	24	0.552	< 0.001	0.308	3.205	0.484

coefficients found in both the Strait ($a_{cdom}(443) = 0.36$ m^{-1}) and in the coastal zone of the Baltic Sea ($a_{cdom}(443) = 0.33$ m^{-1}) (Darecki et al. 2003), which are higher than those found in more open-ocean waters ($< 0.01 \sim 0.13$ m^{-1}) (Morel et al. 2006). CDOM absorbs more in the blue compared to green wavelengths, therefore increasing the blue/green ratio associated with the OC3M algorithm (Eq. 2.2) (Sathyendranath et al. 2001).

Estimation of *chl* concentrations using the standard GSM01 algorithm was not statistically significant with an $r^2 = 0.001$ (Fig. 2.5(a) and Table 2.5). The reduced performance of this algorithm in higher absorption and backscattering environments has also been found in other studies (IOCCG 2006). As identified with the modified GSM01 algorithm (discussed later), this may be related to the limited characterization of particulate optical properties within Fraser River-influenced regions.

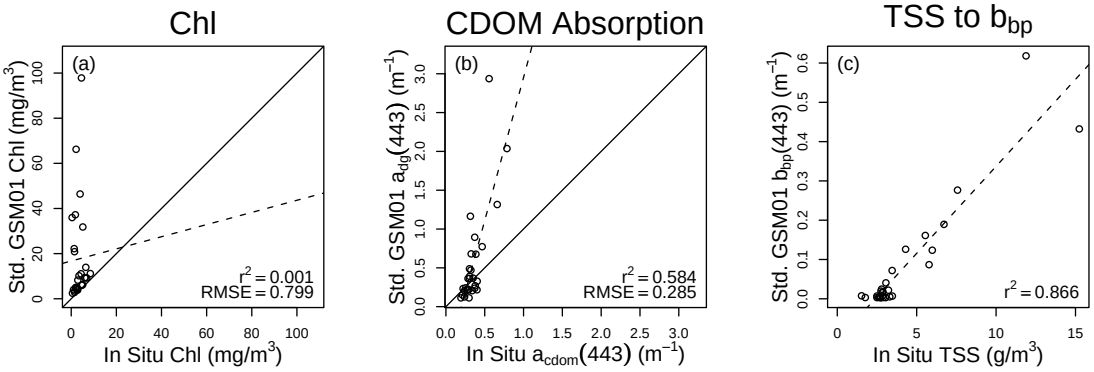

Figure 2.5: Comparison of the standard GSM01 algorithm results with measured (a) *chl* concentrations, (b) CDOM absorption, and (c) TSS. The solid line represents a one-to-one relationship and the dashed line is the linear best fit.

Table 2.5: Results of the standard GSM01 algorithm.

	n	r^2	p-value	$RMSE$	intercept	slope
Chl	28	0.001	0.896	0.799	16.717	0.269
$a_{cdom}(443)$	28	0.584	< 0.001	0.285	-0.734	3.686
TSS	28	0.866	< 0.001	N/A	-0.106	0.044

While the algorithm was not effective at estimating *chl*, it was able to identify higher CDOM absorption and particulate backscatter with statistically significant r^2 values of 0.584 and 0.866, respectively (Fig. 2.5(b) and (c)). The higher $a_{cdom}(443)$ slope of 3.686 may partially be due to the increase absorption related to non-algal particles estimated in the GSM01 $a_{dg}(443)$, which was not reflected in the $a_{cdom}(443)$ measurements. Although absorption from non-algal particles has been found to be as high as CDOM absorption in turbid waters (Doxaran et al. 2006), the relatively high slope and negative intercept suggest poor separation of a_{dg} from the other optical constituents in the more turbid waters of the Strait.

With the inclusion of the Twardowski et al. (2004) CDOM absorption model into the modified GSM01 algorithm, the statistical relationship for *chl* concentrations was slightly improved with a slope closer to one compared to measured *chl* concentrations. However, the relationship was still not statistically significant (Fig. 2.6 and Table 2.6). The improved *chl* relationship is possibly related to better separation between

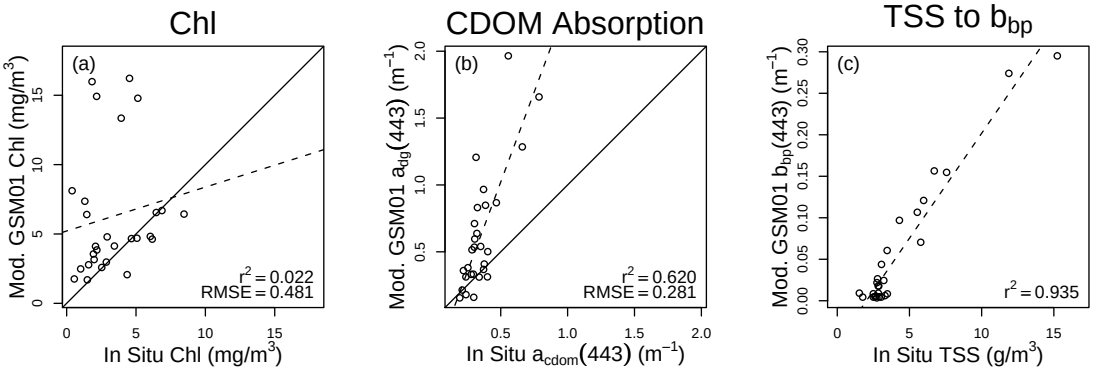

Figure 2.6: Comparison of the modified GSM01 algorithm results with measured (a) *chl* concentrations, (b) CDOM absorption, and (c) TSS. The solid line represents a one-to-one relationship and the dashed line is the linear best fit.

Table 2.6: Results of the modified GSM01 algorithm.

	n	r^2	p-value	$RMSE$	intercept	slope
Chl	28	0.022	0.449	0.481	5.215	0.316
$a_{cdom}(443)$	28	0.620	< 0.001	0.281	-0.322	2.688
TSS	28	0.935	< 0.001	N/A	-0.051	0.025

the optical influence of particulate backscatter and pigment absorption, which is reflected in the general lowering of $b_{bp}(443)$ estimates and a slight improvement in the relationship between TSS and $b_{bp}(443)$ (Fig. 2.6(c)). The relationship between measured $a_{cdom}(443)$ and modified GSM01 estimated $a_{dg}(443)$ improved with a slope value closer to one, an intercept value closer to zero, and a higher r^2. As discussed in relation to the standard GSM01 algorithm, a deviation from a slope of one is expected for higher $a_{cdom}(443)$ values because of increased non-algal particulate absorption in the GSM01 $a_{dg}(443)$ term, which is not represented in the $a_{cdom}(443)$ measurement. With non-algal particulate absorption found to be greater than CDOM absorption in turbid waters (Doxaran et al. 2006), the slope value of 2.688 can be expected in the Fraser River-influenced waters.

The low r^2 value with the modified GSM01 *chl* estimates (Fig. 2.6(a)) is mainly related to approximately 8 stations in the southern Fraser River plume region having overestimated *chl* concentrations. A possible cause for this overestimating is the

limited characterization of particulate optical properties in the Fraser River plume. With particulate scattering being the dominant optical constituent in turbid environments (Morel and Belanger 2006), it is important to have a relatively accurate representation of their optical properties so that the spectral characteristics of other constituents, such as phytoplankton absorption, are not masked by unaccounted for attenuation. In Fig. 2.7 the absolute difference (AD) between estimated and measured *chl* concentrations is compared to the modified GSM01 $b_{bp}(443)$ and $a_{dg}(443)$. The greatest difference in *chl* values is encountered when $a_{dg}(443) > 0.8$ m^{-1} and $b_{bp}(443) > 0.05$ m^{-1}.

The 8 stations with $a_{dg}(443) > 0.8$ m^{-1} and 9 stations with $b_{bp}(443) > 0.05$ m^{-1} are all in the region of the Strait with the greatest influence of the Fraser River plume. By limiting the modified GSM01 algorithm to stations with $a_{dg}(443) <= 0.8$ m^{-1}, the statistical relationship between estimated and measured *chl* is improved ($r^2 = 0.690$) (Fig. 2.8(a)). This suggests that the algorithm performs well in conditions found outside the influence of the Fraser River plume. While most of the stations with $a_{dg}(443) > 0.8$ m^{-1} are during April 2006, it is unclear if algorithm difficulties are related to the limited characterization of particulate absorption, or backscatter, or a combination of both during the initial conditions of the Fraser River freshet.

Limiting *chl* estimates to regions with lower $a_{dg}(443)$ values provides a more consistent relationship with measured *chl* concentrations (Fig. 2.8(a) and Table 2.8). However, the relationship is not one-to-one due to a slight overestimation at lower concentrations and underestimation at higher concentrations. As previously discussed, the overestimation of *chl* at higher concentrations is common for algorithms developed from lower latitude *chl* measurements and applied to higher latitudes due to the lower specific absorption coefficients from the pigment packaging effect (Sathyendranath et al. 2001). Using the two-component absorption model developed by Devred et al. (2006), the difference in packaging effects and accessory pigments for a

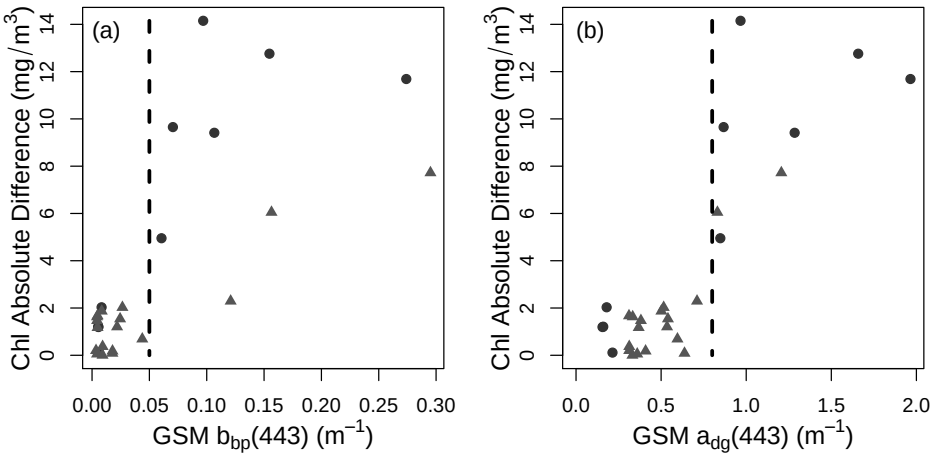

Figure 2.7: Comparison of the modified GSM01 algorithm *chl* absolute differences with measured *chl* against (a) $b_{bp}(443)$ and (b) $a_{dg}(443)$. Stations from April 2006 are identified as circles and July 2006 stations are identified as triangles. The dashed line marks the possible threshold for limiting errors in *chl* estimates associated with particulate variability.

bloom population over a background population can be accommodated.

To accommodate the differences in packaging effect, the $a_{ph}(443)$ values estimated by the modified GSM01 algorithm were re-evaluated using the Devred et al. (2006) phytoplankton model to estimate *chl* concentrations. Results of this re-evaluation are shown in Fig. 2.8(b) and (c) for the general and Vancouver Island two-component phytoplankton models, respectively. Statistical results of the general two-component model did not improve agreement with measured concentrations compared to the modified GSM01 *chl* estimates. The Vancouver Island two-component model showed a slightly higher $RMSE$ value. However, the model did improve agreement with measured *chl* concentrations resulting in a slope closer to one and a slight improvement in the r^2 value to 0.702. There was an unexplained offset between measured and estimated *chl*, which may be associated with the specific phytoplankton absorption properties used by the GSM01 algorithm or residual non-algal particulate absorption uncharacterized by the Twardowski et al. (2004) CDOM model.

The evaluation of the two-component models was only based on the reinterpretation of $a_{ph}(443)$ with the spectral shape of the phytoplankton specific absorption

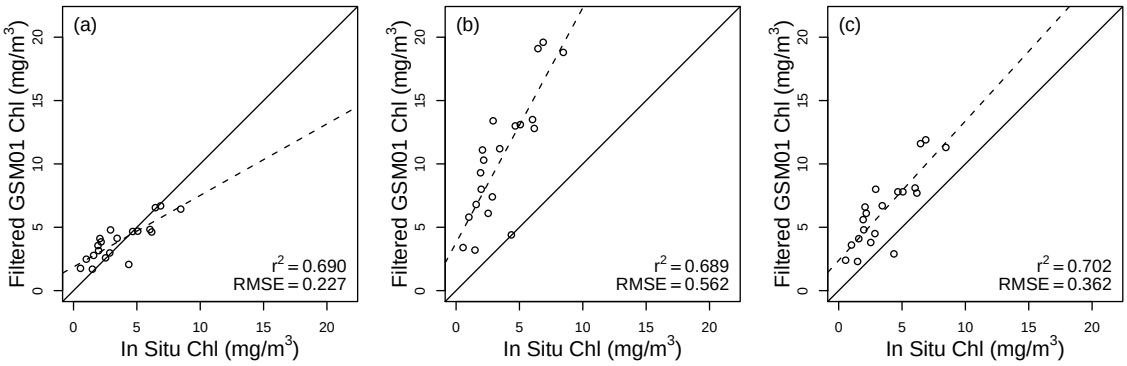

Figure 2.8: Comparison of the modified GSM01 algorithm *chl* with measured concentrations (a) limited to $a_{dg}(443) <= 0.08$ m^{-1}, remodelled *chl* estimates using the Devred et al. (2006) (b) general, and (c) Vancouver Island two-component models.

Table 2.7: Results of the modified GSM01 algorithm with *chl* results filtered to $a_{dg}(443) <= 0.8$ m^{-1} and the filtered $a_{ph}(443)$ values reinterpreted using the Devred et al. (2006) two-component (two-comp.) phytoplankton models.

	n	r^2	p-value	$RMSE$	intercept	slope
Filtered GSM01 Chl	20	0.690	< 0.001	0.227	1.871	0.564
General two-comp. chl	20	0.689	< 0.001	0.562	3.780	1.855
Van. Island two-comp. chl	20	0.702	< 0.001	0.362	2.383	1.100

properties maintained from the standard GSM01 algorithm. With the phytoplankton specific absorption in the standard GSM01 algorithm developed using simulated annealing on a global data set, the spectral shape of the specific absorption coefficients may not accurately reflect the phytoplankton absorption in the Strait and may cause a systematic overestimation in phytoplankton absorption at 443 nm. Further improvements to the IOP characteristics in the Strait may reduce this offset.

2.5 Discussion

The simplicity of the OC3M algorithm is a benefit when used in the diverse waters found in the Strait of Georgia. The OC3M algorithm was effective at estimating *chl* concentrations under the greatest range of water column optical properties measured in this study. With the OC3M algorithm relying only on the ratio of two wavelengths, the spectral characterization of other inherent optical properties is not

needed (IOCCG 2006). Although a fixed region around the Fraser River mouth was used to limit the influence of turbidity on the OC3M algorithm, the region of influence may vary during different Fraser River discharge, tidal, and wind regimes. Typically, a remote-sensing reflectance threshold at 667 nm is applied to identify turbid waters and to mask *chl* estimates in those areas (Patt et al. 2003). Nevertheless, under higher *chl* concentrations, particulate associated with phytoplankton cellular structures may cause a reflectance threshold to mask phytoplankton blooms as turbid waters. To avoid this situation, a more adaptive bio-optical model technique developed by Morel and Belanger (2006) may be more effective at identifying turbid waters.

Compared to the OC3M algorithm, the semi-analytical GSM01 algorithm has the benefits of estimating and compensating for the optical influence from particulate backscatter and combined CDOM and non-algal particulate absorption. However, the characterization of particulate optical properties was a limiting factor in accurately estimating *chl* concentrations in Fraser River-influenced waters, thus requiring the masking of stations with greater particulate optical influence. To mask these stations, thresholds on $a_{dg}(443)$ and $b_{bp}(443)$ estimates were evaluated. A threshold that only considered stations with $a_{dg}(443) < 0.8$ m^{-1} improved the modified GSM01 *chl* r^2 from 0.022 to 0.690 and slope from 0.316 to 0.564. The statistical relationship of *chl* estimates was further improved by using the $a_{ph}(443)$ with a two-component phytoplankton absorption model developed from Vancouver Island samples (Devred et al. 2006), resulting in an r^2 of 0.702 and a slope of 1.100. The phytoplankton absorption model was developed from field measurements (Devred et al. 2006) and defines the transition from a background phytoplankton population with higher specific absorption coefficients to a bloom population dominated by diatoms, which have lower specific coefficients due to packaging effects (Sathyendranath et al. 2001).

Although the Vancouver Island two-component model, which is based on diatom

blooms, improved the *chl* relationship, diatoms do not homogeneously dominate blooms in the Strait. For example, the northern waters of the Strait have shown phytoplankton blooms dominated by non-loricate oligotrichs and dinoflagellates (Haigh and Taylor 1991) instead of diatom blooms found in the southern and central regions (Harrison et al. 1983, Stuart et al. 1998). With differences in the pigment packaging effect and accessory pigments, dinoflagellates are expected to have different specific absorption properties compared to diatoms. These differences in phytoplankton community composition affect the specific absorption properties of phytoplankton in the region and consequently, *chl* estimates (Sathyendranath et al. 2001). Therefore, when the phytoplankton model based on diatom blooms is indiscriminately applied to *chl* estimates throughout the entire Strait, errors in estimates may occur.

The reinterpretation of phytoplankton absorption coefficients with the Vancouver Island two-component model, while improving the linear relationship with measured *chl*, had an increased $RMSE$ of 0.362 compared the GSM01's $RMSE$ of 0.227 (Table 2.7). The increased $RMSE$ may be related to the phytoplankton specific absorption coefficients used in the GSM01 algorithm. Unaccounted for attenuation or transpectral scattering maybe compensated for in the simulated-annealing derived phytoplankton specific absorption coefficients. As noted by Maritorena et al. (2002), the specific absorption coefficients at 412 and 490 nm (Table 2.1) are lower than values typically measured in other studies (Bricaud et al. 1998) and may be related to unaccounted for attenuation from particles or CDOM. As well, the specific absorption coefficient at 670 nm is lower and may account for the fluorescence scattering, which can influence wavelengths near the peak at 685 nm (Gower et al. 1999). To reduce the $RMSE$ associated with the Vancouver Island two-component *chl* estimates, three approaches may be effective. The first is to use simulated annealing with reflectance measurements from the Strait of Georgia to derive the phytoplankton specific absorption coefficients, as done in other studies (Kostadinov et al. 2007). A second

approach is to incorporate fluorescence as an additional optical component that is dependent upon *chl*. The final approach is to use a band that is not as close to the fluorescence peak at 685 nm, such as the 645 nm land band on the MODIS sensor (Franz et al. 2006).

Another limiting factor in using the GSM01 algorithm is the fixed nature of η (Eq. (2.10)), which is characterized by: the particle size distribution, the ratio of organic to inorganic, and the particulate refractive index (Babin et al. 2003a). While semi-analytical algorithms are not sensitive to small differences in η (Lee et al. 2002), errors in particulate backscatter estimates are transferred to the absorption properties (Dall'Olmo and Gitelson 2006). A possible method to overcome a fixed η is to use a regression equation relating a reflectance ratio to η (Lee et al. 2002) and model it to the particulate backscatter properties found in the Strait. This would allow for a transition from less turbid to Fraser River-influenced waters. Spectral variability in particulate backscatter properties in the Strait is not known. However, it is expected to vary spatially and temporally in relation to Fraser River plume dynamics.

In addition to the fixed particulate backscatter properties, the proper definition of non-algal particulate absorption characteristics, compared to CDOM absorption, is important in turbid waters. As identified in coastal environments (Darecki et al. 2003, D'Sa et al. 2006) and within the Fraser River catchment (Gallie and Murtha 1992), the absorption properties of non-algal particles can be significant compared to open-water environments. April 2006 *chl* estimates had the greatest absolute difference (Fig. 2.7), even though TSS concentrations ranges were similar to those found during July 2006 (Table 2.2). This would suggest higher non-algal particulate absorption in Fraser River plume waters during April, before the freshet, and may be related to a higher portion of organic particles typically found during this period (Milliman 1980). The plume would then shift towards inorganic particles at the peak of the freshet. To account for the absorption properties of non-algal particles, it is

important to characterize how the spectral properties differ from CDOM absorption under a range of Fraser River discharge conditions.

Three important factors have to be taken into consideration when interpreting results of this study. First, the sampling extent was spatially limited within the Strait of Georgia. With all the study samples collected in the southern and central regions, biophysical properties of the northern portion of the Strait may not be represented. For instance, optical properties of biophysical variables, such as phytoplankton and CDOM absorption, may differ in the northern region. Second, at least half of the above-water remote-sensing reflectance measurements were collected under cloudy conditions. As identified in past studies (Ruddick et al. 2006), an accurate estimation of the ρ_{sky} value in Eq. (2.12) is difficult under variable cloud conditions. A more precise and adaptive method for estimating ρ_{sky} would allow for more reliable above-water reflectance measurements, particularly under heavy cloud cover conditions. Finally, to apply the evaluated algorithms to MODIS Aqua imagery, atmospheric attenuation process must be accounted for. In consideration of this point, the OC3M algorithm might perform better than GSM01 algorithms because the OC3M algorithm only relies on the ratio of two wavelengths. As shown in bio-optical models (Dall'Olmo and Gitelson 2006) and field measurements (Darecki and Stramski 2004), accurate atmospheric correction of all wavelengths is critical to deriving biophysical measurements from ocean-colour imagery.

Further, as identified by several studies (Bailey and Werdell 2006, Darecki and Stramski 2004), atmospheric correction can be problematic in coastal waters for several reasons, including turbidity related reflectance in the near infrared (Lavender et al. 2005), absorbing aerosols (Bailey and Werdell 2006), and nitrogen dioxide absorption (Ahmad et al. 2007). In particular, the overcorrection of the shorter 412 and 443 nm wavelengths can cause issues with semi-analytical algorithms that are dependent upon accurate correction of these wavelengths.

Inversion of multi-spectral coastal water measurements into the optical influence of biophysical variables is an extremely ambiguous mathematical problem (Defoin-Platel and Chami 2007). With several combinations of biophysical variables resulting in similar remote-sensing reflectance, it is important to limit the possible ranges of biophysical values. To accommodate this, Defoin-Platel and Chami (2007) suggested dividing the global problem-set into more localized versions that better represent bio-optical conditions found in common environments. In the case of the Strait, it may be beneficial to have semi-analytical models for various levels or stages of influence from the Fraser River plume. This would smooth the transition from CDOM dominant conditions found in the central portion of the Strait to the highly turbid conditions found close to the mouth of the Fraser River. As identified in this study, the threshold value for $a_{dg}(443)$ may provide a transition point to an environment influenced by particles from the Fraser River.

2.6 Conclusion

The OC3M, standard GSM01, and modified GSM01 algorithms were evaluated in the case 2 waters of the Strait of Georgia. To evaluate these algorithms, above-water remote-sensing reflectance and biophysical measurements were taken under spring and summer conditions in 2006. Results showed that the OC3M was only effective at estimating *chl* concentrations when limited to areas outside the immediate vicinity of the Fraser River discharge and the associated higher turbidity. Therefore, to effectively use the OC3M algorithm with MODIS Aqua imagery, it is necessary to mask the more turbid regions of the Fraser River plume. With the possible dynamic nature of the Fraser River plume, a technique that accounts for bio-optical characteristics of a phytoplankton bloom over turbid waters, such as that defined by Morel and Belanger (2006), would possibly be more effective than the predefined geographical region used in this study.

Similarly, the modified GSM01 algorithm was only effective at estimating *chl* concentrations at stations with lower combined CDOM and non-algal particulate absorption (a_{dg}), even given the improving CDOM absorption model. This suggests that the optical properties of particles in plume waters needs to be better characterized to improve the modified GSM01 algorithm's accuracy.

In conjunction with the standard and modified GSM01 algorithms, inherent optical property models were evaluated for the Strait of Georgia. First, the Twardowski et al. (2004) hyperbolic CDOM absorption model was found to improve spectral agreement with CDOM absorption measurements in the Strait. Second, a two-component phytoplankton absorption model defined by Devred et al. (2006) was found to better represent the relationship between *chl* and phytoplankton absorption at 443 nm. These modifications to the GSM01 algorithm, in conjunction with the filtering of stations with higher combined absorption from non-algal particles and CDOM, provided the best relationship between measured and estimated *chl* concentrations with an $r^2 = 0.702$ and a slope of 1.1. Although the IOP models in this study were evaluated in the context of the GSM01 algorithm, they are general models that can be incorporated into other semi-analytical algorithms, such as one developed by Lee et al. (2002).

A key element to increasing the effectiveness of the modified GSM01 algorithm in the Strait of Georgia is the characterization of the particulate optical properties. This includes the spectral characterization of absorption and backscatter from non-algal particles. Through the inclusion of the particulate optical properties into the modified GSM01 algorithm, it may be more effective at estimating biophysical variables in Fraser River-influenced waters.

In conclusion, based on simulated MODIS Aqua bands, both the OC3M and modified GSM01 algorithms should be adequate at estimating *chl* concentrations in the Strait of Georgia using MODIS Aqua imagery given effective atmospheric correction

and excluding in the Fraser River plume area. These algorithms, in conjunction with the time series of MODIS Aqua imagery, can provide a broader scale view of *chl* concentrations and associated biophysical processes in the Strait of Georgia surface waters.

Chapter 3

Atmospheric correction of MODIS imagery for western Canada coastal waters

3.1 Introduction

Atmospheric correction of ocean-colour imagery is critical to measuring energy reflected from the water column and to derive biophysical variables (Stamnes et al. 2005). For open-ocean and some coastal waters, the atmospheric correction of ocean-colour imagery has proven to be effective (Zibordi et al. 2006, Wang et al. 2005). However, the standard atmospheric correction for the Moderate Resolution Imaging Spectroradiometer (MODIS) Aqua sensor has been problematic in many coastal areas because of turbidity induced water reflectance in the near infrared, absorbing aerosols, and absorption from nitrogen dioxide (NO_2) (Lavender et al. 2005, Schollaert et al. 2003, Ahmad et al. 2007). Atmospheric correction difficulties have been identified by the poor correlation between *in situ* and satellite estimated water-leaving radiance in the Baltic Sea by Darecki and Stramski (2004). These difficulties are further supported by the identification of a globally consistent overcorrection of shorter blue wavelengths in coastal waters compared to open ocean waters (Bailey and Werdell

2006).

As the standard OC3M chlorophyll-a (*chl*) algorithm is dependent upon the blue wavelengths (O'Reilly et al. 2000), *chl* products produced by NASA's Ocean Color Group are particularly vulnerable to the atmospheric correction difficulties in coastal waters. The standard *chl* products produced by NASA's Ocean Color Group from MODIS imagery uses a near infrared atmospheric correction (Patt et al. 2003) with the OC3M algorithm. The OC3M algorithm is an adaptation of the OC2 and OC4 algorithms developed for the Sea-Viewing Wide Field-of-view Sensor (SeaWiFS) to the spectral bands on the MODIS sensor (O'Reilly et al. 2000). While this algorithm is primarily based on more open-water measurements, it generally works well in coastal waters with limited chromophoric dissolved organic matter absorption and suspended particles (Blondeau-Patissier et al. 2004). Nonetheless, the OC3M algorithm shows limited performance in waters with high CDOM absorption or suspended particles (Darecki and Stramski 2004).

The Strait of Georgia, located off the southwest coast of Canada, is a typical example of a case 2 water body, in which, spatially, light attenuation is dominated by either CDOM absorption or scattering from suspended particles (Johannessen et al. 2006, Loos and Costa submitted). Therefore to effectively estimate *chl* concentrations using MODIS Aqua imagery, it is important to evaluate the performance of the combination of atmospheric correction approaches and *chl* algorithms with imagery of the Strait.

The objective of this study was therefore to evaluate two ocean-colour algorithms designed for MODIS Aqua imagery for identifying spatial and temporal *chl* concentration patterns in the surface waters of the Strait of Georgia. As a key component to this objective, these *chl* algorithms were evaluated in conjunction with three atmospheric correction methods: a near infrared (NIR), a shortwave infrared (SWIR), and a combined spatially averaged correction approach developed by the Manage-

ment Unit of the North Sea Mathematical Models (MUMM) and adapted for this study.

3.2 Atmospheric Correction Background

Reflectance from the water surface is used to estimate the optical influence of biophysical variables, such as *chl* concentrations (Stamnes et al. 2005). Hence, to estimate *chl* concentrations from water reflectance, the attenuation and reflectance related to atmospheric constituents must be removed from the top-of-atmosphere radiance measured by the MODIS Aqua sensor (Gordon and Wang 1994, Gordon 1997). The top-of-atmosphere radiance, measured by the MODIS sensor, was normalized using the extraterrestrial reflectance.

For this study, extraterrestrial reflectance at a particular wavelength, $\rho(\lambda)$, is defined as (Gordon and Wang 1994)

$$\rho(\lambda) = \pi L(\lambda)/\bar{F}_0(\lambda)\cos\theta_0 \tag{3.1}$$

where $L(\lambda)$ is radiance at a given wavelength λ, $\bar{F}_0(\lambda)$ is the extraterrestrial solar irradiance, and θ_0 is the solar zenith angle.

Using the exterrestrial reflectance in Eq. (3.1), the combined exterrestrial reflectance of the atmosphere and water body, ρ_w, on the top-of-atmosphere reflectance, $\rho_t(\lambda)$, is defined as (Gordon and Wang 1994)

$$\rho_t(\lambda) = \rho_r(\lambda) + \rho_A(\lambda) + t(\lambda)\rho_w(\lambda) \tag{3.2}$$

with $\rho_r(\lambda)$ and $\rho_A(\lambda)$ representing the reflectance from air molecules (Rayleigh scattering) and aerosols (including multiple scattering between aerosols-air), respectively. $t(\lambda)$ represent the diffuse transmittance through the atmosphere at a sensor viewing angle. To use ocean-colour algorithms for *chl* estimation, the above-water

reflectance, ρ_w, term must be isolated from ρ_t.

The $\rho_A(\lambda)$ includes both direct scattering from aerosols and multiple scattering between air molecules and aerosols. As identified by Wang (2006a), ρ_A can be related to the single-scattering aerosol reflectance, ρ_{as}, using lookup tables based on viewing geometry and aerosol optical thickness. Past studies have looked at separating the multiple scattering component from direct aerosol scattering (Antoine and Morel 1999). However, Wang (2004) found that separating these components had limited influence on the final atmospheric correction. Thus, $\rho_{as}(\lambda)$ is used in the single scatter epsilon, $\varepsilon(\lambda_s, \lambda_l)$, defined as

$$\varepsilon(\lambda_s, \lambda_l) = \frac{\rho_{as}(\lambda_s)}{\rho_{as}(\lambda_l)} \tag{3.3}$$

The single scatter epsilon characterizes the aerosol type using $\rho_{as}(\lambda)$ at two wavelengths, with λ_s representing a shorter wavelength and λ_l a longer wavelength. The $\varepsilon(\lambda_s, \lambda_l)$ value is used to identify the appropriate aerosol type and, consequently, to correct the visible wavelengths based on optical properties of predefined aerosol models (Shettle and Fenn 1979, Gordon and Wang 1994, Wang 2006a).

In following sections, the theoretical backgrounds and major assumptions associated with the three evaluated atmospheric correction algorithms are discussed.

3.2.1 Near Infrared (NIR) Atmospheric Correction

The near infrared (NIR) atmospheric correction uses NIR wavelengths to characterize aerosol scattering and to correct visible wavelengths. This is the standard atmospheric correction for MODIS imagery used to produce ocean-colour products from NASA's Ocean Color Group (Patt et al. 2003, Bailey and Werdell 2006). This standard correction approach is based on the assumption that $\rho_w(\lambda)$ in Eq. (3.2) is close to zero in the NIR and that any reflectance is associated with atmospheric scattering. This is commonly referred to as the black pixel assumption (Siegel et al. 2000).

Provided that $\rho_r(\lambda)$ is well characterized (Gordon et al. 1988a, Wang 2005), Eq. (3.2) can be re-arranged to calculate Rayleigh-corrected reflectance, $\rho_{rc}(\lambda)$, defined as

$$\rho_{rc}(\lambda) = \rho_t(\lambda) - \rho_r(\lambda) \tag{3.4}$$

As ρ_w is approximately zero at 748 nm and 869 nm, $\rho_{rc} \approx \rho_A$ and the NIR ρ_{rc} can be use to characterize both the aerosol type and reflectance (Gordon and Wang 1994, Wang 2006a).

To identify the aerosol type at a MODIS Aqua image pixel, the $\varepsilon(748, 869)$ is calculated using Eq. (3.3) (Gordon and Wang 1994, Gordon 1997, Siegel et al. 2000) with a typical range of 0.95 to 1.26 (Wang 2007). The identified aerosol type in conjunction with the $\rho_A(869)$ is then used to estimate $\rho_A(\lambda)$ and atmospheric transmittance in the visible wavelengths through predefined lookup tables (Gordon and Wang 1994, Wang 2006a). For standard ocean-colour products from MODIS Aqua imagery, the NIR atmospheric correction relaxes the black pixel assumption by incorporating an iterative fit approach that combines the reflectance from aerosols and possible reflectance from particles correlated to *chl* concentration. By compensating for particulate reflectance associated with *chl* concentrations greater than 2 mg m^{-3}, the NIR atmospheric correction is effective in a broader range of water conditions (Siegel et al. 2000, Patt et al. 2003).

3.2.2 Shortwave Infrared (SWIR) Atmospheric Correction

As 25 g m^{-3} of suspended fine particles can reach $\rho_w(800) \approx 0.05$ (Bale et al. 1994) and known NIR reflectance related to phytoplankton blooms (Siegel et al. 2000), the zero water reflectance assumption in the NIR may not be effective for atmospherically correcting coastal imagery (Darecki and Stramski 2004, Wang et al. 2007). As an alternative, the use of shortwave infrared (SWIR) wavelengths, greater than 1000 nm, has been proposed for the characterization of aerosols in turbid coastal waters (Gao

et al. 2000, Wang 2007). At these wavelengths, water absorption coefficients are an order of magnitude higher compared to 869 nm (Hale and Querry 1973), and therefore the SWIR bands are less influenced by turbid water reflectance. By using the 1240 and 2130 nm bands on the MODIS Aqua satellite to calculate $\varepsilon(1240, 2130)$ in Eq. (3.3), the contribution of ρ_w to ρ_t is avoided in turbid waters (Wang and Shi 2005). The $\varepsilon(1240, 2130)$ typically ranges from 0.98 to 4.76, which is a wider range of values compared to $\varepsilon(748, 869)$. This larger range of values is related to the greater wavelength distance between bands centres (Wang 2007).

Similar to the NIR atmospheric correction, the SWIR atmospheric correction identifies the aerosol properties at each pixel within the image using $\varepsilon(1240, 2130)$ and $\rho_A(2130)$. The aerosol properties in the SWIR bands are then used to estimate $\rho_A(\lambda)$ in the visible wavelengths using lookup tables generated by a radiative transfer model (Wang 2007).

3.2.3 MUMM Atmospheric Correction

Several methods of atmospherically correcting turbid water imagery using the NIR wavelengths have been suggested. A common method is to to apply aerosol properties from non-turbid to turbid waters by assuming spatial homogeneity in atmospheric aerosols (Hu et al. 2000). A variation to this method, defined by Ruddick et al. (2000), assumes that aerosol type variability is spatially limited ($\sim$ 200 km) and particulate backscatter variability is spectrally limited in the NIR (Gould et al. 1999, Zhang et al. 1998).

A consequence to the limited spectral variability of particulate backscatter in the NIR is that variability is generally dominated by water absorption. As identified through bio-optical models (Ruddick et al. 2000, Li 2003), the $\rho_w(\lambda)$ at two NIR wavelengths maintain a consistent ratio, α, in turbid waters (Eq. (3.5)). This ratio was found to equal 1.945 for the MODIS Aqua sensor (Ruddick et al. 2006).

$$\frac{\rho_w(748)}{\rho_w(869)} = \alpha \tag{3.5}$$

The Ruddick et al. (2000) approach uses α and a predefined $\varepsilon(748, 869)$ to isolate the water and aerosols reflectance, respectively, in the Rayleigh-corrected reflectance, $\rho_{rc}(\lambda)$, defined in Eq. (3.4). The Rayleigh-corrected reflectance includes the aerosol reflectance and water reflectance that is transmitted through the atmosphere. Using an estimated value of $\varepsilon(748, 869)$ and α, the following equations can be solved to separate the reflectance from aerosols and water in the Rayleigh-corrected reflectance (Ruddick et al. 2000).

$$\rho_A(869) = \frac{\alpha\rho_{rc}(869) - \rho_{rc}(748)}{\alpha - \varepsilon(748, 869)} \tag{3.6}$$

$$t(869)\rho_w(869) = \frac{\rho_{rc}(748) - \varepsilon(748, 869)\rho_{rc}(869)}{\alpha - \varepsilon(748, 869)} \tag{3.7}$$

$$\rho_A(748) = \varepsilon(748, 869)\left[\frac{\alpha\rho_{rc}(869) - \rho_{rc}(748)}{\alpha - \varepsilon(748, 869)}\right] \tag{3.8}$$

$$t(748)\rho_w(748) = \alpha\left[\frac{\rho_{rc}(748) - \varepsilon(748, 869)\rho_{rc}(869)}{\alpha - \varepsilon(748, 869)}\right] \tag{3.9}$$

To account for the effect of diffuse atmospheric transmittance, $t(\lambda)$, on ρ_w in Eq. (3.7) and (3.9), the α constant is multiplied by γ, which is defined as (Ruddick et al. 2000)

$$\gamma = \frac{t_v(748)t_0(748)}{t_v(869)t_0(869)} \tag{3.10}$$

where $t_v(\lambda)$ is the sensor diffuse transmittance and $t_0(\lambda)$ is the solar diffuse transmittance. Atmospheric transmittance and the resultant γ are dependent upon the

geometry, aerosol optical thickness, and aerosol optical properties (Yang and Gordon 1997).

Following the separation of ρ_w and ρ_A from ρ_{rc}, $\rho_A(748)$ and $\rho_A(869)$ are passed to the standard NIR atmospheric correction discussed in Section 3.2.1. With the iterative fit of the standard NIR atmospheric correction (Patt et al. 2003), some degree of variability in the aerosol type and optical thickness is allowed. This approach is commonly referred to as the Management Unit of the North Sea Mathematical Models (MUMM) atmospheric correction and has effectively been applied to satellite imagery of turbid North Sea waters to monitor biophysical parameters (van der Woerd and Pasterkamp 2004).

An important component to the MUMM atmospheric correction is the definition of $\varepsilon(748, 869)$ for use in Eq. (3.6) through (3.9). The original algorithm was defined for imagery acquired with the SeaWiFS sensor, thus requiring the estimation of the NIR single scattering epsilon from less turbid regions and applying it to turbid waters (Ruddick et al. 2000). In the Strait of Georgia, with *chl* concentrations consistently higher than 3 mg m^{-3} (Harrison et al. 1983, Radi et al. 2007) and significant terrestrial particulate influence (Johannessen et al. 2006), the identification of areas with limited turbidity is difficult or impossible during spring bloom, Fraser River freshet, and even late summer conditions.

To overcome the difficulty with selecting $\varepsilon(748, 869)$ in turbid waters, the SWIR atmospheric correction was used to estimate NIR aerosol reflectance for each image pixel. Using the SWIR atmospheric correction estimated aerosol radiance at 748 and 869 nm, the resulting $\varepsilon(748, 869)$ were calculated using Eq. (3.3) for each pixel in the image. The SWIR estimated $\varepsilon(748, 869)$ in the central and southern portions of the Strait allows a definition of the atmospheric aerosol type that can be averaged for the study area with limited turbid water influence. However, the low signal-to-noise ratio (SNR) of the SWIR MODIS Aqua bands (Wang 2007) and possible

land contamination of the SWIR reflectance can make these bands problematic for atmospheric correction of smaller water bodies, such as the Strait of Georgia. To limit land contamination and reduce noise associated with the SWIR bands, the mean $\varepsilon(748, 869)$ value from the more open portions of the southern and central Strait were used. In conjunction with the mean $\varepsilon(748, 869)$, the sensor and solar diffuse transmittance estimated by the SWIR atmospheric correction were use to calculate the spatial mean γ based Eq. (3.10).

3.3 Methods

3.3.1 Ferry *Chl* Data

To evaluate *chl* estimates from the MODIS Aqua imagery, *chl* measurements from an unattended flow-through fluorometer installed on the BC Ferry central route shown in Fig. 3.1 were used. This fluorometer measures *chl* concentrations in the engine water uptake of the ferry (Halverson et al. 2003). The ferry fluorometer samples at 30-second intervals; as a result, multiple ferry measurements coinciding with a single MODIS pixel were averaged. Although the minimum and maximum number of ferry measurements per image pixel was 1 and 7, respectively, typically only 2 or 3 measurements coincided. Ferry measurements were also spatially limited to between -123.66° and -123.17° longitude to reduce possible land influence. This instrument has been in operation since 2003, but measurements were limited to those taken in 2006. This is the time frame the instrument was most frequently cleaned and had been most recently calibrated (October 2005). Bio-fouling was corrected for by a linear correction between the previously cleaned instrument blank reading and the subsequent pre-cleaned or bio-fouled blank reading. The difference between the cleaned and bio-fouled reading was linearly applied to measurements between cleanings (Halverson, personal communication, May 8, 2007).

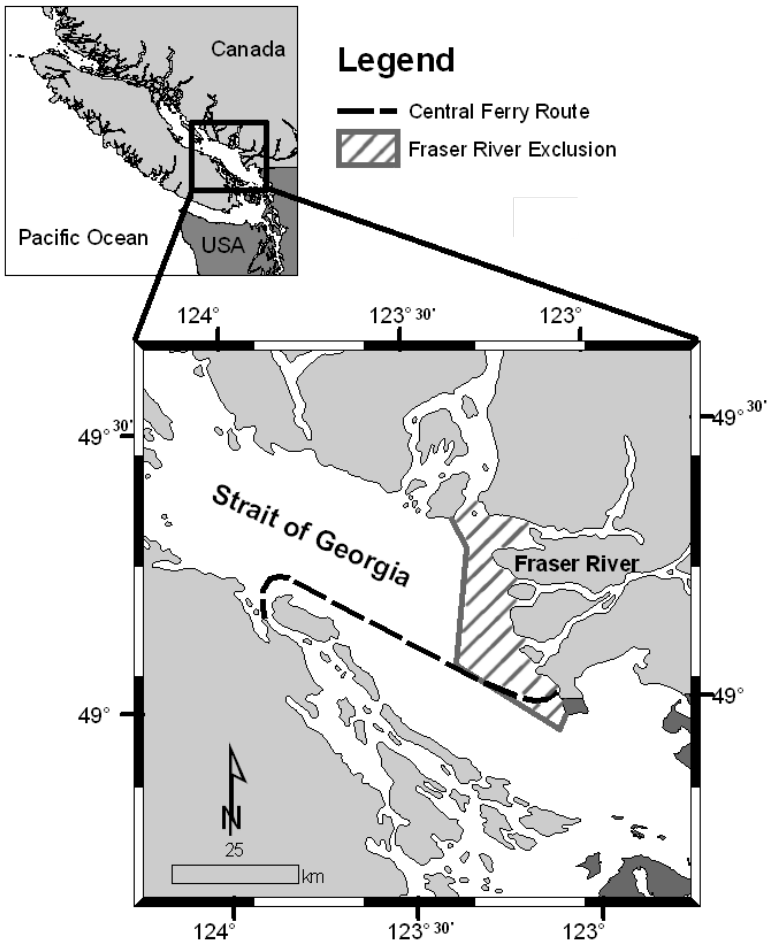

Figure 3.1: Ferry route (dashed line) and Fraser River exclusion region (shaded region) used in this study.

3.3.2 MODIS Aqua Imagery

For this study, ferry measurements were limited to ±1 hour from the satellite pass to limit movement of water masses between ferry measurements and the MODIS Aqua acquisition (Bailey and Werdell 2006). In addition to this temporal limitation, images with visible cloud cover or haze over the central or southern portions of the Strait were eliminated from this analysis. Based on these criteria, a total of 9 images were selected for analysis. MODIS Aqua imagery, including higher resolution bands, were processed from level 1A (L1A) using the SeaDAS version 5.1.3 (Baith et al. 2001). Images were not corrected for bi-directional reflectance variability because the standard bi-directional reflectance distribution function is based on case 1 waters (Morel et al. 2002) and the Strait of Georgia is expected to be a case 2 water body.

When selecting MODIS imagery pixels, many of the flags used with level 3 *chl* mosaics produced by NASA's Ocean Color Group were masked for this study. The masked flags include sun glint, high solar/sensor zenith angles, and atmospheric correction warnings/errors. However, flags more common in coastal waters, such as stray light, turbid waters, and high radiance pixels were not masked. In addition to these masked flags, pixels with negative reflectance in the 443 and 488 nm bands were also masked for the OC3M algorithm and pixels with negative reflectance in the 412, 443, or 488 nm bands were masked for the modified GSM01 algorithm. Differences between the number of pixels used in this study and the number of pixels resulting from each combination of atmospheric correction and *chl* algorithm is because of pixels masked due to difficulty with the atmospheric correction algorithm.

3.3.3 MUMM Correction Modifications

To apply the MUMM correction, the SWIR atmospheric correction was used to estimate the $\varepsilon(748, 869)$ (Section 3.2.3). However, because the SWIR bands are particularly sensitive to atmospheric water vapour (Gao et al. 1993), they were initial

corrected for water-vapour absorption using the implementation in the SeaDAS software package.

In summary, the following steps were used to apply the MUMM atmospheric correction.

- Atmospherically correct the image using the SWIR correction.
- Spatially average $\varepsilon(748, 869)$ from the SWIR estimated NIR aerosol reflectance.
- Spatially average γ using SWIR estimated NIR atmospheric transmittance.
- Atmospherically correct the image using MUMM correction with calculated $\varepsilon(748, 869)$ and γ values.

3.3.4 Atmospheric Correction Evaluation Criteria

To evaluate the effectiveness of the NIR, SWIR, and MUMM atmospheric correction, $\rho_w(\lambda)$ was processed using the OC3M algorithm (O'Reilly et al. 2000) and a modified version of the GSM01 algorithm (Chapter 2). The modified GSM01 algorithm was an adaptation of standard GSM01 algorithm (Maritorena et al. 2002) with the combined chromophoric dissolved organic matter (CDOM) and detrital particulate absorption model replaced with a hyperbolic function identified by Twardowski et al. (2004). Based on *in situ* reflectance measurements, this algorithm more accurately estimated *chl* concentrations in regions of the Strait under limited Fraser River influence, compared to the OC3M algorithm (Chapter 2).

In addition to evaluating the OC3M algorithm with all atmospherically corrected pixels, the influence of the Fraser River plume on the OC3M algorithm was also evaluated. Within a $\sim$ 4 km region around the Fraser River tidal region, particulate concentrations are highest during the freshet, reaching values as high as 400 mg m^{-3} (Kostaschuk et al. 1993) and adversely affecting OC3M algorithm (Chapter 2). Thus, points within a $\sim$ 4 km region around the Fraser River tidal region were removed

for the Fraser River excluded OC3M analysis. The Fraser River exclusion region is identified in Fig. 3.1 as the shaded region.

The modified GSM01 algorithm has also previously shown to be sensitive to Fraser River influence and its associated particulate (Chapter 2). In this case, the modified GSM01 algorithm was used to estimate the combined absorption at 443 nm from chromophoric dissolved organic matter and non-algal particulate, $a_{dg}(443)$. Chapter 2 identified $a_{dg}(443) < 0.8$ m^{-1} as an effective threshold to limit Fraser River influence. However, for this study the threshold was set to 1.2 m^{-1} to allow for possible inaccuracy associated with atmospheric correction of blue wavelengths.

The estimated *chl* concentrations from each algorithm were compared to *chl* measurements from the unattended ferry fluorometer using the Root-Mean-Square-Error ($RMSE$) defined as (IOCCG 2006)

$$RMSE = \left(\frac{\sum_{i=1}^{n} [\log(\chi_i^{model}) - \log(\chi_i^{true})]^2}{n-2} \right)^{1/2} \tag{3.11}$$

where χ^{model} representing the algorithm *chl* estimate, χ^{true} the measured *chl* concentration, and n the number of evaluated measurements. Linear regression and the associated slope and intercept were also used to evaluate the relationship between estimated and measured *chl* concentrations. Due to the differences in population sizes (number of pixels) between combinations of atmospheric correction and *chl* algorithms, the adjusted r^2 value was used to evaluated the fit of linear models.

3.4 Results

A total of 9 MODIS Aqua images, representing spring and summer conditions with diverse Fraser River influence (Fig. 3.2), were used in the analysis. Table 3.1 summarizes the mean *chl* concentrations from the ferry fluorometric measurements that coincide with MODIS image pixels. The average coefficient of variation for measured *chl* within the pixel resolution of MODIS Aqua ocean colour bands was 6.0%. Results

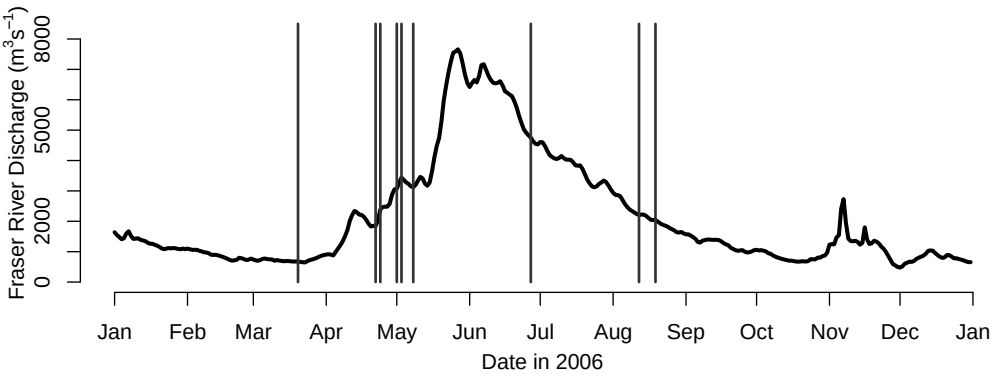

Figure 3.2: Preliminary daily mean Fraser River discharge measurements from Hope, BC, hydrologic station ($\sim$ 150 km from the Strait). Vertical lines signify the dates of the satellite images used in this study. Data was courtesy of the Water Survey of Canada.

show a progression of lower average *chl* concentrations in March (3.5 mg m^{-3}), to higher concentrations in May (11.3 mg m^{-3}), and to lower concentrations in August (1.9 mg m^{-3}). Additionally, Table 3.1 provides ferry summaries for measurements outside of the Fraser River exclusion region (Fig. 3.1). Generally, the observed seasonal *chl* variations are similar to those measured in other studies (Harrison et al. 1983, Haigh and Taylor 1991, Yin et al. 1997).

In the following sections, the NIR, SWIR, and MUMM atmospheric correction algorithms were evaluated for estimating *chl* concentrations using the OC3M and modified GSM01 algorithms.

3.4.1 NIR Atmospheric Correction Results

Results of the NIR atmospheric correction are provided in Fig. 3.3 and Table 3.2. The linear relationship between the ferry and OC3M *chl* concentrations had a statistically significant adjusted r^2 of 0.603 (Fig. 3.3(a)). However, *chl* concentrations were generally overestimated and estimates were limited to concentrations < 21 mg m^{-3} in the May 3rd image (Table 3.1). The consistent overestimation is reflected in the $RMSE$ of 0.545 for all points (Fig 3.3(a)). As shown in Fig. 3.4(a), the largest relative *chl* errors were in the 0 to 5 mg m^{-3} range. Further, the NIR atmospheric correction was only effective for 75% of the image pixels in this study. As will be

Table 3.1: The number of MODIS pixels after previously discussed spatial and temporal subsetting (n) and *chl* minimum-maximum (mean) for each date (YYYYMMDD) from ferry measurements. The Fraser River exclusion columns (Fraser River Exc.) specify the number of pixels and the *chl* concentrations for pixels outside the Fraser River exclusion region (Fig. 3.1).

	All		Fraser River Exc.	
Date	n	*chl* (mg m^{-3})	n	*chl* (mg m^{-3})
20060320	11	2.6-5.0(3.5)	11	2.6-5.0(3.5)
20060422	49	0.2-1.0(0.5)	35	0.2-0.8(0.5)
20060424	36	0.4-12.1(7.3)	17	0.4-9.9(6.8)
20060501	57	2.1-15.7(9.7)	40	7.3-15.7(12.4)
20060503	56	3.3-26.0(14.6)	39	6.5-26.0(16.7)
20060508	55	1.6-20.8(9.7)	38	1.6-20.8(10.4)
20060627	55	0.6-15.3(3.5)	38	0.6-7.2(2.0)
20060812	51	0.8-3.4(1.8)	37	0.8-3.4(1.7)
20060819	50	0.9-4.7(2.0)	30	0.9-1.9(1.3)
Total	420	0.2-26.0(5.8)	285	0.2-26.0(6.1)

Table 3.2: Results of the near infrared (NIR) atmospherically corrected estimated *chl*.

	n	Adj. r^2	p-value	$RMSE$	intercept	slope
OC3M	313	0.603	< 0.001	0.545	4.852	1.019
OC3M (Fraser River Exc.)	180	0.759	< 0.001	0.523	3.630	1.244
Modified GSM01	1	N/A	N/A	N/A	N/A	N/A

identified in Section 3.4.3, this is due to the algorithm's inability to identify the $\varepsilon(748, 869)$ in more turbid and higher *chl* regions of the Strait.

With the removal of points within the Fraser River region, the adjusted r^2 value improved to 0.759 (Fig. 3.4(b) and Table 3.2). However, there was limited improvement to the $RMSE$ and the percentage of total pixel that had *chl* estimates reduced to 63%. Removal of Fraser River plume points reduced the number of points with the largest errors in the 0 to 5 mg m^{-3} range (Fig 3.4(b)), thus increasing the slope and decreasing the intercept (Table 3.2). These changes in the linear regression between ferry and OC3M *chl* suggests that *chl* estimates within the Fraser River area have a larger offset and more variability compared to ferry *chl* measurements, which is possibly related to the spectral influence of high turbidity (Dall'Olmo and Gitelson 2006).

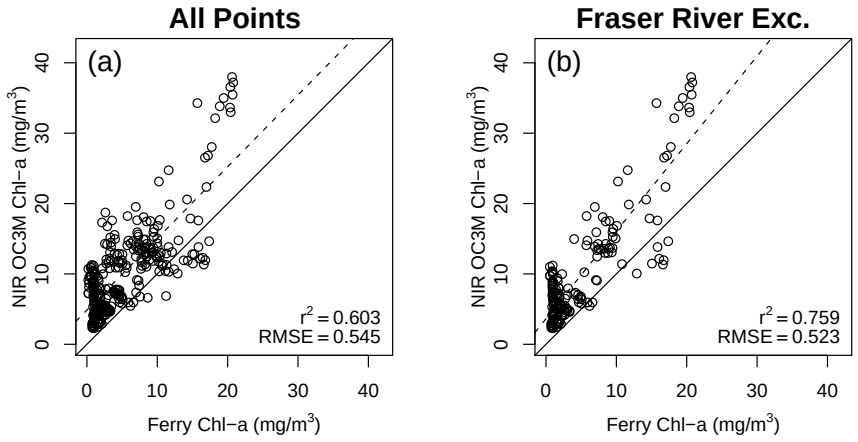

Figure 3.3: Comparison of ferry *chl* measurements with *chl* estimates from MODIS Aqua imagery with the NIR atmospheric correction using (a) the OC3M algorithm and (b) the OC3M algorithm with points in the Fraser River exclusion area identified in Fig. 3.1 removed.

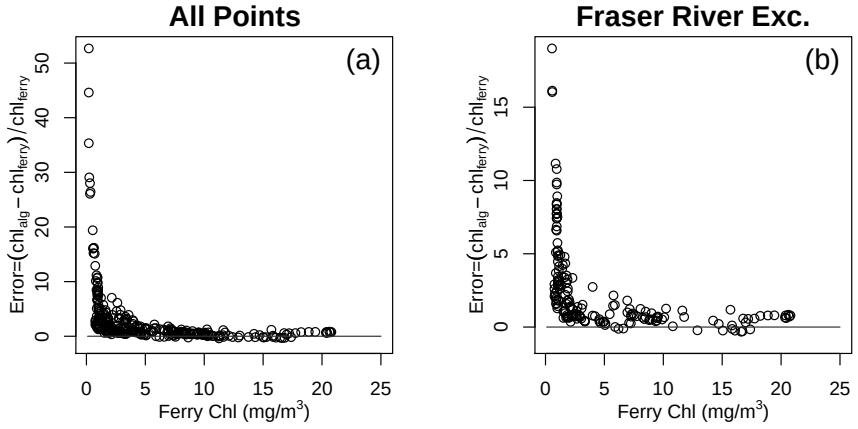

Figure 3.4: Relative error between combined NIR atmospheric correction and OC3M estimates versus ferry measured *chl* concentrations for (a) all measurements and (b) measurements outside the Fraser River exclusion region.

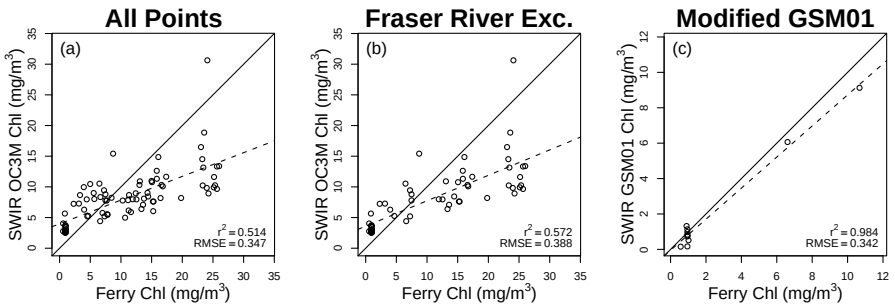

Figure 3.5: Comparison of ferry *chl* measurements with *chl* estimates for MODIS Aqua imagery with the SWIR atmospheric correction using (a) the OC3M algorithm, (b) the OC3M algorithm with the Fraser River region excluded, and (c) the modified GSM01 algorithm.

The modified GSM01 algorithm was not effective at estimating *chl* concentrations with the NIR atmospheric correction (Table 3.2). The NIR atmospheric correction resulted in negative remote-sensing reflectance at 412 nm from the overcorrection of this band. The modified GSM01 algorithm depends on the 412 nm band; as a result, it was only able to estimate the *chl* concentration for a single NIR corrected pixel with lower $a_{dg}(443)$ absorption.

3.4.2 SWIR Atmospheric Correction Results

The SWIR atmospheric correction combined with the OC3M algorithm only provided *chl* estimates for approximately 21% of the available pixels. This is likely related to the low signal-to-noise ratio (SNR) of the SWIR bands (Wang 2007). Although the adjusted $r^2 = 0.514$ was statistically significant (Fig. 3.5(a) and Table 3.3), the linear slope of 0.386 between measured and estimate *chl* concentrations is slightly lower than recent studies using *in situ* reflectance measurement (Chapter 2) and indicates over- and under-estimation at lower and higher *chl* concentrations, respectively (Fig. 3.6(a)).

Exclusion of points near the Fraser River plume improved the relationship with ferry *chl* measurements (adjusted $r^2 = 0.572$) by removing points at lower and intermediate concentrations (Fig. 3.5(b), Fig. 3.6(b), and Table 3.3). However, the

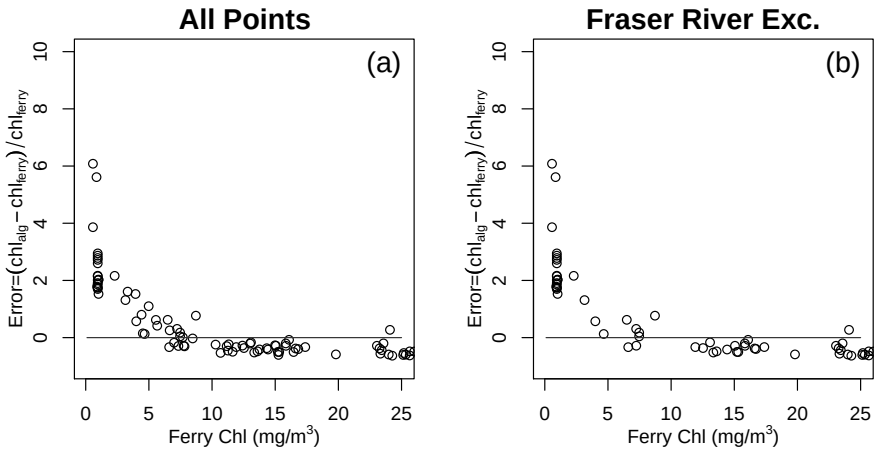

Figure 3.6: Relative error between combined SWIR atmospheric correction and OC3M estimates versus ferry measured *chl* concentrations for (a) all measurements and for (b) measurements outside the Fraser River exclusion region.

Table 3.3: Results of the shortwave infrared (SWIR) atmospherically corrected *chl* estimates compared to ferry *chl* measurements.

	n	Adj. r^2	p-value	$RMSE$	intercept	slope
OC3M	87	0.514	< 0.001	0.347	3.982	0.386
OC3M (Fraser River Exc.)	61	0.572	< 0.001	0.388	3.587	0.415
Modified GSM01	11	0.984	< 0.001	0.342	-0.051	0.878

percentage of total measurements that *chl* concentrations were estimated was still relatively low with 21% of study pixels having *chl* estimates. The linear slope of 0.415 and intercept of 3.587 are similar to those found with *in situ* radiometric and *chl* measurements (Woźniak and Stramski 2004).

The modified GSM01 algorithm was not effective at estimating *chl* concentrations with SWIR atmospherically corrected images (Fig. 3.5(c) and Table 3.3) because *chl* concentration were only estimated for 11 pixels of the study. Although the 412 nm band did not have as significant an overcorrection issues (not shown), as found with the NIR correction, the modified GSM01 algorithm was not able to estimate *chl* concentrations for the majority of the pixels.

3.4.3 MUMM Atmospheric Correction Results

To apply the MUMM atmospheric correction, the aerosol characterization, as defined by $\varepsilon(748, 869)$, and the atmospheric transmittance, as defined by γ, had to be assessed for each image using the estimated NIR aerosol reflectance and atmospheric transmittance from the SWIR atmospheric correction. Examples of $\varepsilon(748, 869)$ values estimated by the NIR atmospheric correction and SWIR correction for the May 3, 2006 image are provided in Fig. 3.7. The histograms show that the SWIR correction (Fig. 3.7(b) and (d)) provides lower estimates of $\varepsilon(748, 869)$ compared to the NIR atmospheric correction (Fig. 3.7(a) and (c)). Also, the SWIR estimated $\varepsilon(748, 869)$ has a bimodal distribution. The slightly higher $\varepsilon(748, 869)$ average in the NIR image is likely associated with *chl* reaching concentrations greater than 20 mg m^{-3} on May 3rd, 2006 (Table 3.1). Consequently, the zero NIR water reflectance assumption of the NIR atmospheric correction is violated (Siegel et al. 2000), and the iterative black pixel correction may not effectively compensate under these higher *chl* concentrations. Difficulties with NIR atmospheric correction $\varepsilon(748, 869)$ estimation may also be related to particles from the Fraser River plume. However, the plume usually does not reach as far north (Johannessen et al. 2006) as the variability in the NIR

estimated $\varepsilon(748, 869)$ shows (Fig. 3.7(a)).

The bimodal distribution of the SWIR estimated $\varepsilon(748, 869)$ may be related to the low signal-to-noise ratio of the SWIR bands causing the atmospheric correction algorithm to switch between two aerosol models. Spatially, the SWIR estimated $\varepsilon(748, 869)$ has lower values in the open portions of the Strait and increases near the coastline (Fig. 3.7(b)), which represents the second small peak at $\varepsilon(748, 869) \approx 1.03$. This is possibly related to land influence on the SWIR bands, which disproportionately increases both the reflectance at 1240 nm and the resulting $\varepsilon(748, 869)$ estimate (Wang 2007). To minimize this possible influence, $\varepsilon(748, 869)$ values were averaged from pixels in only the middle of the Strait (Table 3.4), and when a bimodal distribution was found, the mean of the dominant peak was used. For instance, the mean $\varepsilon(748, 869)$ with the May 3rd, 2006 image was estimated at 1.007 for the lower range $\varepsilon(748, 869)$ peak and is identified by the red dashed line on Fig. 3.7(d). The value of γ was selected in the same manner as the spatially averaged $\varepsilon(748, 869)$ value for each image.

To validate the use of the spatially average SWIR $\varepsilon(748, 869)$ and α values, these ratios were evaluated against variability in the Rayleigh-corrected reflectance at 748 and 869 nm. In Fig. 3.8, scatterplots of Rayleigh-corrected reflectance in the NIR are presented with the solid line representing the SWIR estimated $\varepsilon(748, 869)$ and α represented by the dashed line. Results show that pixels dominated by aerosol reflectance fall close to the $\varepsilon(748, 869)$ slope and pixels dominated by turbid waters have reflectance ratios closer to the α slope (Fig. 3.8). With increasing turbidity, $\rho_w(748)$ is disproportionately increased over $\rho_w(869)$ because of higher water absorption at 869 nm and the $\rho_{rc}(748)/\rho_{rc}(869)$ ratio approaches α. Points that have higher $\rho_{rc}(869)$ values and that fall above the $\varepsilon(748, 869)$ line are mostly land influenced pixels.

Upon evaluating the spatial variability of the SWIR estimated $\varepsilon(748, 869)$, the

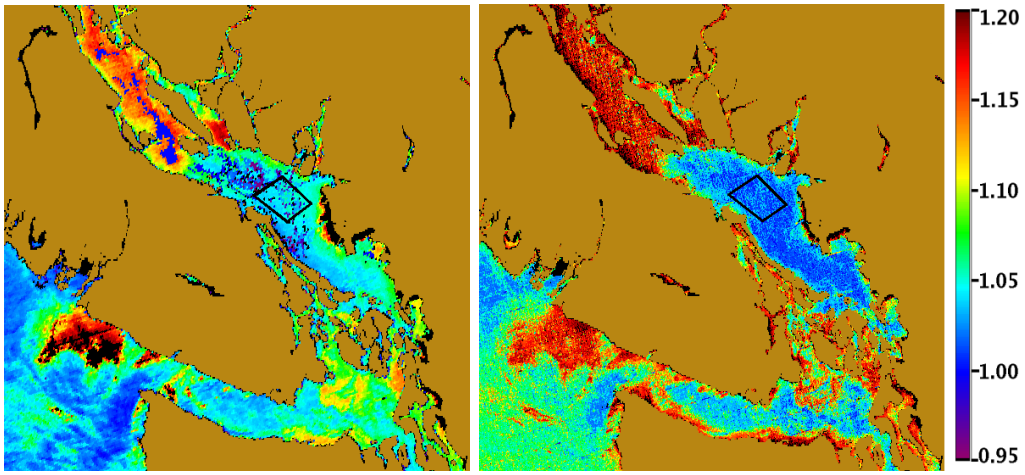

(a) NIR $\varepsilon(748, 869)$ Image (b) SWIR $\varepsilon(748, 869)$ Image

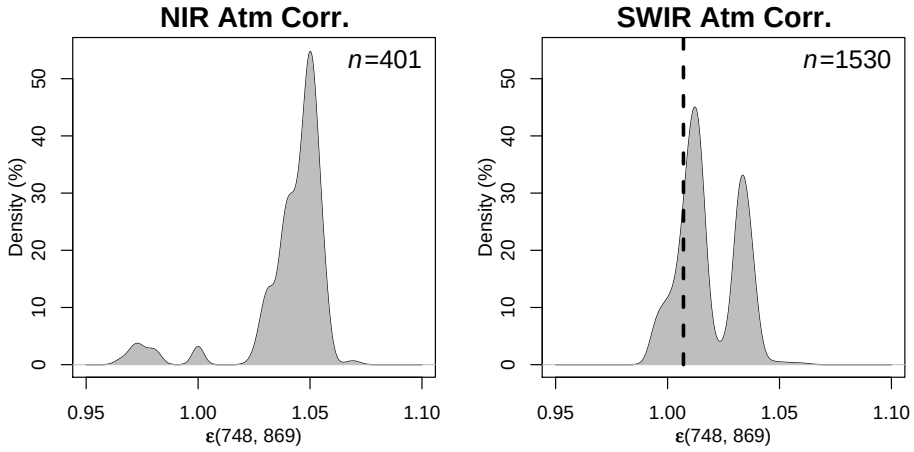

(c) (d)

Figure 3.7: $\varepsilon(748, 869)$ estimates for the May 3, 2006 image using the (a) and (c) NIR and (b) and (d) SWIR atmospheric correction. Differences in population sizes, n, in the two histograms is related to the SWIR bands having a resolution of 500 m and the NIR bands having a resolution of 1 km. The black box on each image shows the area that was used to produce the histograms.

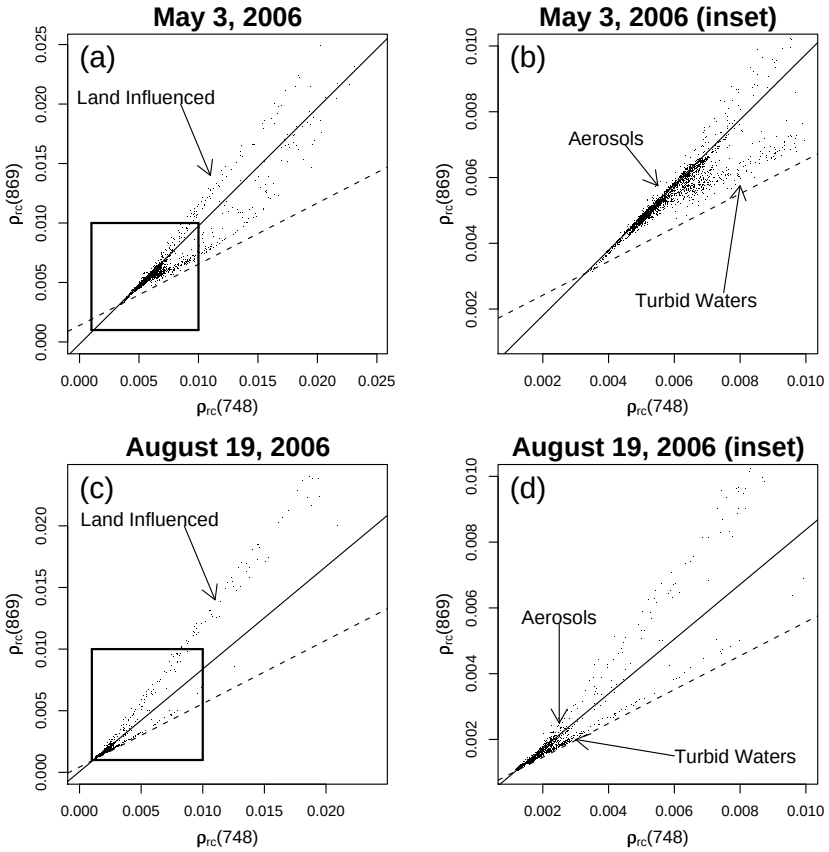

Figure 3.8: Scatterplot of Rayleigh-corrected reflectance at 748 and 869 nm in the central and southern portions of the Strait for (a and b) May 3, 2006 and (c and d) August 19, 2006. The $\varepsilon(748, 869)$ for each day is identified with the solid line and the $\alpha = 1.945$ from Ruddick et al. (2006) is displayed as the dashed line.

Table 3.4: $\varepsilon(748, 869)$ and γ values estimated from SWIR atmospheric correction and used for the MUMM atmospheric correction.

Date	$\varepsilon(748, 869)$	γ
20060320	1.131	0.980
20060422	1.117	0.982
20060424	1.043	0.985
20060501	1.085	0.983
20060503	1.007	0.986
20060508	1.154	0.982
20060627	0.997	0.986
20060812	1.190	0.982
20060819	1.202	0.982

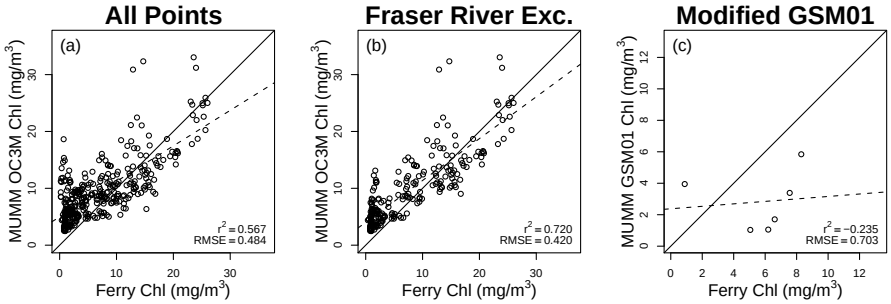

Figure 3.9: Comparison of ferry *chl* measurements with *chl* estimates for MODIS Aqua imagery with the MUMM atmospheric correction using (a) the OC3M algorithm, (b) the OC3M algorithm with measurements in the Fraser River exclusion area removed, and (c) the modified GSM01 algorithm.

Table 3.5: Results of the MUMM atmospherically corrected *chl* estimates compared to ferry measured concentrations.

	n	Adj. r^2	p-value	$RMSE$	intercept	slope
OC3M	373	0.567	< 0.001	0.484	4.970	0.625
OC3M (Fraser River Exc.)	238	0.720	< 0.001	0.420	4.020	0.736
Modified GSM01	6	-0.235	0.839	0.703	2.378	0.078

averaged values of $\varepsilon(748, 869)$ and γ (Table 3.4) were used in conjunction with the MUMM atmospheric correction. The combination of the MUMM correction and the OC3M algorithm was effective at estimating *chl* in a greater range of conditions compared to other two atmospheric correction or the modified GSM01 algorithm, as reflected in the percentage of total pixels with *chl* estimates. While the adjusted r^2 value is slightly lower than for the NIR OC3M *chl* estimates, the $RMSE$ is lower, and the algorithm was able to estimate *chl* concentrations for 89% of the pixels used in this study. Both the intercept and slope were slightly higher than recent evaluations of the OC3M algorithm in the Strait using *in situ* reflectance measurements (Chapter 2). The results show an overestimation at lower *chl* concentrations (Fig. 3.10(a)) and slope lower than one. Some of the difference in the slope and intercept may be related to a consistent overestimation of lower *chl* concentrations in the August 19 image, which is identified in Section 3.4.4.

The observed overestimation at lower *chl* concentrations (Fig. 3.10) may be re-

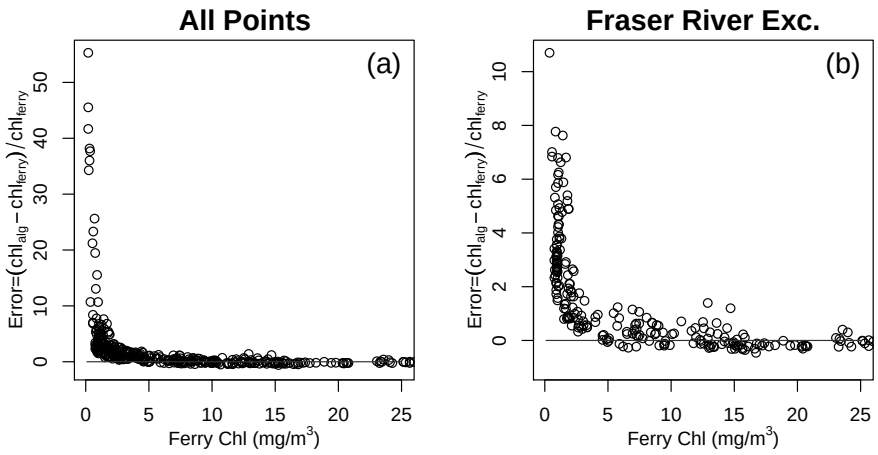

Figure 3.10: Relative error between combined MUMM atmospheric correction and OC3M estimates versus ferry measured *chl* concentrations for (a) all measurements and (b) measurements outside the Fraser River exclusion region.

lated to higher CDOM absorption ($a_{cdom}(443) = 0.36$ m^{-1}) usually found in the Strait (Chapter 2) compared to more open-ocean waters (Morel et al. 2006), for which the OC3M algorithm was developed. The slope being less than one suggests that diatoms, which have a lower specific absorption value compared to more equatorial phytoplankton communties (IOCCG 2000) and are commonly found in the southern portion of the Strait (Harrison et al. 1983, Stuart et al. 1998), may be the dominant bloom phytoplankton in the study images.

Excluding pixels in the immediate vicinity of the Fraser River (Fig. 3.1) slightly improved the adjusted r^2 and $RMSE$ values. Also, the intercept was lowered and slope increased, bringing the linear regression close to a one-to-one relationship with measured *chl* concentrations. The exclusion of Fraser River pixels reduced errors in *chl* estimates in 0 to 5 mg m^{-3} range (Fig. 3.10(b)), suggesting that bloom conditions ($chl > 10$ mg m^{-3}) generally occur outside of the excluded region for the selected dates of this study. This is further indicated by the spatial-temporal patterns discussed in Section 3.4.4.

The modified GSM01 algorithm was ineffective with MUMM atmospherically corrected images with only 6 pixels having *chl* estimates. This was due to negative

412 nm reflectance in the less turbid central portions of the Strait, which is generally where the modified GSM01 algorithm is limited.

3.4.4 Spatial-Temporal *Chl* Patterns

To identify spatial-temporal *chl* patterns using MODIS Aqua imagery, the MUMM atmospheric correction with the OC3M algorithm was used because of the relatively high percentage of total pixels (89%) and lower $RMSE$ that the combination had, compared to the NIR OC3M combination. Using the MUMM atmospheric correction, a selection of OC3M *chl* images and their associated ferry transects are provided in Fig. 3.11 to evaluate spatial and temporal patterns in the Strait of Georgia. Transects in Fig. 3.11 provide ferry *chl* measurements and the corresponding OC3M *chl* estimates based on longitude. A progression of conditions is observed, with lower *chl* concentrations in late winter (Fig. 3.11 (a) and (b)), to *chl* bloom conditions in early May (Fig. 3.11 (c) to (f)) followed by late summer conditions with lower *chl* concentrations (Fig. 3.11 (g) and (h)).

Influence of the Fraser River plume on the OC3M algorithm is visible on both May 1st and 3rd (Fig. 3.11 (c) through (f)), with the algorithm deviating from ferry *chl* measurements at the eastern side of the Strait. This is the time of year with increased Fraser River discharge (Fig. 3.2), and is typically found to have the highest sediment concentrations from the Fraser River into the Strait (Milliman 1980, Kostaschuk et al. 1989, Johannessen et al. 2006). The movement of the plume is, to some degree, visible in how the ferry and OC3M *chl* diverge. For instance, the May 1st transect shows the Fraser River exclusion border (shaded region) lining up with the divergence, while the May 3rd image shows a more westerly divergence at approximately $-123.38°$ longitude. The possible influence of the plume is also visible in the May 3rd transect (Fig. 3.11(f)) with the *chl* concentrations dropping from 25 mg m^{-3} to approximately 15 mg m^{-3} around the Fraser River plume region. This suggests that the Fraser River discharge is influencing phytoplankton distribution

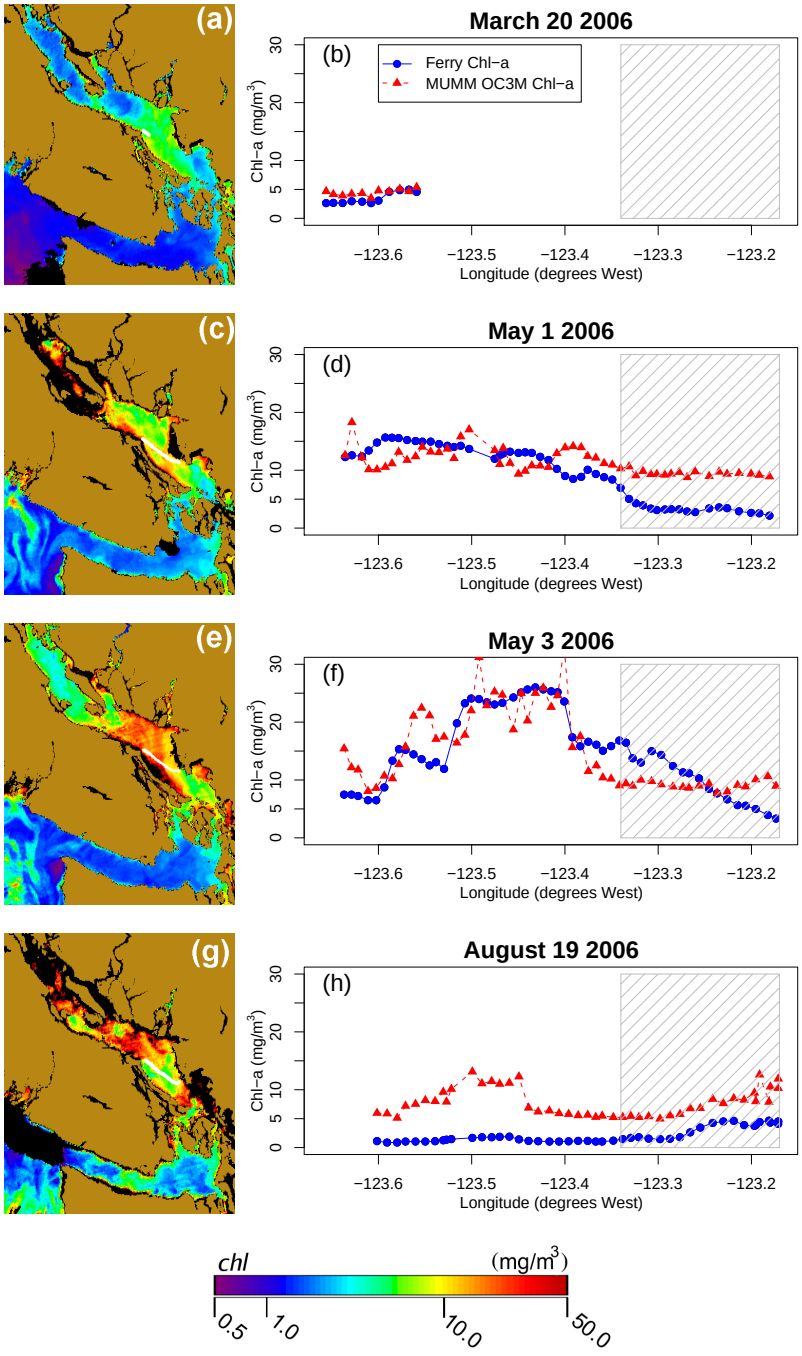

Figure 3.11: Temporal series of OC3M *chl* images using the MUMM atmospheric correction. The ferry path is shown on each satellite image as a white line and the Fraser River exclusion region is represented by the shaded box on each transect graph.

dynamics in the southern portions of the Strait. During lower flow conditions of the Fraser River, in late summer to early winter, the exclusion zone may not need to be applied. This is demonstrated in the August 19th transect (Fig. 3.11(h)) in which no divergence in the transect related to the Fraser River was observed.

Although limited influence from the Fraser River plume was observed in the August 19th image, a consistent offset was observed throughout the transect (Fig. 3.11(h)) that does not appear to be related to the Fraser River discharge. A similar offset was found in the August 12th image (not shown) over a similar range of longitudes. This offset may be related to higher particulate concentrations measured by Johannessen et al. (2006) in autumn that does not appear to be associated with the Fraser River. By December/January the surface layer of higher particle concentrations dissipates (Johannessen et al. 2006), which is possibly why the March 20th image shows improved *chl* agreement between the ferry and OC3M algorithm. Note that the March transect is limited to the Strait's westerly area because of the timing of the ferry in relation to the MODIS Aqua pass and spatially limiting measurements to more open portions of the Strait.

In addition to turbidity influences on the OC3M algorithm, a difficulty with using the spatial average of the $\varepsilon(748, 869)$ from the SWIR atmospheric correction is that atmospheric properties can vary between areas of the Strait. This atmospheric variability is possibly the reason for the large *chl* errors with the August 19th image and transect in the central portion of the Strait (Fig. 3.11(g) and (h)). This is likely related to an inability to differentiate atmospheric variability between the two areas using the SWIR atmospheric correction. As shown in Fig. 3.8, the August 19th image had much lower Rayleigh-corrected reflectance with a median $\rho_{rc}(869)$ of 0.0015 compared to a median $\rho_{rc}(869)$ of 0.0053 in the May 3rd image. With the substantially lower Rayleigh-corrected reflectance in the August 19th, the signal-to-noise ratio of the SWIR bands makes the identification of spatial $\varepsilon(748, 869)$ variability difficult.

Some of the larger *chl* estimation errors in the 0 to 2 mg m^{-3} range (Fig. 3.10) are associated with the August 19th image.

An additional issue encountered was striping within *chl* estimates of the May 3rd image. This is possibly related to detector calibration differences between the blue and green bands, which are enhanced in the image because of the relatively low reflectance in the blue wavelengths due to absorption from higher *chl* concentrations (3.1 to 26.0 mg m^{-3}) (Table 3.1).

3.5 Discussion

The combination of the NIR atmospheric correction and OC3M algorithm was moderately effective for estimating *chl* in the Strait, resulting in an adjusted r^2 of 0.589 and a slope close to one. However, with *chl* concentrations in the Strait reaching as high as 30 mg m^{-3} (Harrison et al. 1983, Li et al. 2000) and varying particulate concentrations from terrestrial sources (Johannessen et al. 2005), the accuracy of the atmospheric correction is diminished. This is shown by the inability of the NIR atmospheric correction to estimate *chl* concentrations > 21 mg m^{-3}. Further, as shown in Fig. 3.7(a), the NIR atmospheric correction algorithm was not able to estimate the $\varepsilon(748, 869)$ in the central portion where the highest *chl* concentrations occurred (Fig. 3.11(e)). A possible solution to this issue is to modify the relationship between *chl* and particulate scattering used by the NIR iterative atmospheric correction to adapt it to bloom conditions in the Strait.

As well as influencing NIR water reflectance, attenuation related to turbidity from the Fraser River was shown to significantly impact the effectiveness of the OC3M algorithm. Although a predefined exclusion region was used to evaluate the Fraser River influence on the OC3M algorithm, a more effective method may be to use a turbidity index, such as the one identified by Shi and Wang (2007). This index uses the SWIR bands to estimate the significance of water reflectance in the NIR bands.

A threshold value of the index may be useful for identifying regions of the Strait that are have high turbidity and that should not be evaluated by the OC3M algorithm.

Just as NIR water reflectance can cause difficulties with the NIR correction, atmospheric constituents typically found in coastal environments can cause the overcorrection of the 412 and 443 nm bands. While identified in all three atmospheric correction algorithms, the overcorrection and the resultant negative reflectance was most prevalent in the NIR and MUMM correction. The 412 nm band is important to semi-analytical algorithms (Carder et al. 1999, Maritorena et al. 2002); therefore, it is critical to isolate the causes of this overcorrection. One possible cause, as identified by Ahmad et al. (2007), is the absorption from atmospheric nitrogen dioxide (NO_2). In the study area, specifically the Lower Fraser Valley, there is substantial urban development resulting in a higher amount of atmospheric NO_2 production (Pisano et al. 1997). Thus, future studies of ocean colour in the Strait may benefit from the NO_2 correction of the 412 and 443 nm bands.

In addition to the possible absorption from NO_2, the presence of absorbing aerosols from dust events and urban environments can cause the overcorrection of the 412 and 443 nm bands (Li et al. 2003a, Schollaert et al. 2003). Absorbing aerosols are not detected well by the standard NIR atmospheric correction algorithms (Bailey and Werdell 2006). Although detection and correction algorithms to address these aerosols exist (Nobileau and Antoine 2005, Ransibrahmanakul and Stumpf 2006), they are based on case 1 water assumptions and are therefore not likely to be effective in the Strait of Georgia. An alternative is to use an absorbing aerosols detection algorithm that utilizes MODIS's SWIR bands (Shi and Wang 2007). However, the authors identified the ineffectiveness of the algorithm in turbid waters. Since there is limited knowledge regarding the presence and properties of absorbing aerosols in the Strait of Georgia, it is unclear if an absorbing aerosol algorithm is necessary. A locally available sunphotometer on Saturna Island may be helpful in identifying

the presence and optical properties of absorbing aerosols in the Strait (Bokoye et al. 2001).

In conjunction with addressing atmospheric correction issues, *chl* estimates may be further improved by using algorithms more applicable to phytoplankton communities found in the Strait of Georgia. As identified in past studies, the absorption properties of the bloom phytoplankton communities in the Strait are significantly influenced by pigment packaging effects (Stuart et al. 1998). Using a more community specific *chl* algorithm that better represents the specific absorption properties of phytoplankton communities in the Strait, such as the one identified by Alvain et al. (2006), may reduce the *chl* underestimation at higher concentrations with the MUMM and SWIR corrected OC3M *chl* estimates (Fig. 3.5 and 3.9). Although the *chl* estimates may approach a one-to-one relationship compared to measured concentrations with a community specific algorithm, an offset is still expected resulting from CDOM absorption (Chapter 2).

Furthermore, the spatial extent of the ferry route, which was limited to the southern portion, reduces the range of conditions sampled in the Strait. With the Fraser River plume and associated particulate dominating the southern Strait, this region represents the most turbid waters found in the Strait (Johannessen et al. 2006). The central portion is typically less turbid and the OC3M algorithm should be more effective in this area, given accurate atmospheric correction of the image. As Fig. 3.11(g) shows, the atmosphere properties can vary between the central and southern portions of the Strait and may require a separate interpretation the of $\varepsilon(748, 869)$ in each region.

3.6 Conclusion

The study objective was to evaluate the use of a NIR, SWIR, and MUMM atmospheric correction to estimate *chl* concentrations in the Strait of Georgia surface

waters. To accomplish this, estimated *chl* concentrations from the empirical OC3M and semi-analytical modified GSM01 algorithms were evaluated against ferry *chl* measurements. Spatial and temporal patterns within the MUMM corrected OC3M *chl* images and the corresponding ferry transects were discussed.

The combination of the NIR atmospheric correction and OC3M algorithm provided *chl* estimates for 75% of the pixels in the study, showed a consistent overestimation of *chl* concentrations, and was limited to pixels with *chl* concentrations $<$ 21 mg m^{-3}. The NIR correction and modified GSM01 approach was not able to estimate *chl* concentrations for any pixels in this study due to consistent negative reflectance in the 412 nm band.

Similar to the NIR correction, the use of the modified GSM01 algorithm was ineffective with the SWIR and MUMM atmospheric corrections due to negative reflectance in the 412 nm band. The overcorrection and noise within the 412 nm band may have been the main reason for the poor performance of the modified GSM01 algorithm. The negative reflectance may be alleviated with an NO_2 absorption correction or accounting for absorbing aerosols.

Atmospherically correcting with SWIR bands was not as effective as using the NIR bands because of the limited number of pixels (21%) that had *chl* estimates using the OC3M algorithm. While the SWIR atmospheric correction did not have as significant of a negative reflectance issue with the 412 nm band, there was considerable noise within the water-leaving reflectance and the OC3M images. Comparison between the ferry and OC3M *chl* concentrations from the SWIR corrected images showed over- and underestimation of *chl* at lower and higher concentrations, respectively. The SWIR correction with the modified GSM01 algorithm was only able to estimate *chl* concentrations for 11 pixels. Much of the difficulty with using SWIR atmospheric correction may have been associated with the low signal-to-noise ratio in the SWIR bands (Wang 2007).

Using a combined MUMM and SWIR approach proved to be effective in the greatest range of conditions, as demonstrated by the relatively high percentage of pixels (89%) that had estimated *chl* concentrations. In addition, the consistent *chl* overestimation found with the NIR correction was removed and the relationship between the OC3M *chl* and ferry *chl* was closer to recent evaluations of the algorithm in the Strait using *in situ* radiometric measurements (Chapter 2).

Limiting *chl* evaluations to pixels outside a predefined region around the Fraser River improved *chl* estimates for all three atmospheric correction approaches. In two May images, the MUMM correction with the OC3M algorithm was insensitive to *chl* fluctuations and estimates were not effective within the Fraser River excluded region. This exclusion region did not appear to have a significant impact outside the freshet periods. However, higher particulate concentrations found throughout the Strait during late summer seems to cause an overestimation of *chl* with the OC3M algorithm.

Although the combined MUMM correction and OC3M algorithm was generally effective outside the more turbid portions of the Strait, spatial averaging of aerosol properties estimated by the SWIR atmospheric correction may not be effective at characterizing the aerosol properties for all regions of the Strait. The August 19th image showed that atmospheric properties may vary between the southern and central portions of the Strait, thus resulting in overestimated *chl* concentrations in the central portions of the Strait. Difficulties in estimating the aerosol properties in the centre of the Strait may have been related to the limited sensitivity of the SWIR bands and the low aerosol reflectance on that day.

The MUMM atmospheric correction in conjunction with the spatially averaged SWIR aerosol properties was the most effective atmospheric correction in the range of conditions found in this study. MUMM corrected images with the OC3M algorithm were effective at identifying spatial and temporal patterns in surface *chl* concen-

trations throughout the Strait. This effectiveness is further improved by limiting the algorithm to pixels outside the immediate vicinity of the Fraser River discharge during freshet conditions.

Chapter 4

Conclusions

The goal of this research was to evaluate remote-sensing techniques for estimating chlorophyll-a (*chl*) in the Strait of Georgia using MODIS Aqua imagery. To meet this goal, two major objectives were addressed:

1. Evaluate *chl* algorithms using ship-based measurements.
2. Evaluate atmospheric correction methods with *chl* algorithms for MODIS Aqua imagery.

As an additional component to these objectives, spatial-temporal *chl* patterns within MODIS imagery were assessed. The first objective was accomplished in Chapter 2 using ship-based radiometric and biophysical measurements collected in April and July of 2006. This data set allowed for the evaluation of the algorithms with limited considerations of atmospheric properties. The second objective was met in Chapter 3 using MODIS Aqua imagery and *chl* measurements from an unattended flow-through fluorometer installed on a BC Ferry ship.

From the ship-based measurements, absorption from chromophoric dissolved organic matter (CDOM) was found to generally be higher than the estimated phytoplankton absorption based on the Devred et al. (2006) Vancouver Island phytoplankton absorption model at 443 nm. Consequently, surface waters of the Strait can generally be classified as a CDOM-dominant case 2 waters (Prieur and Sathyendranath

1981). However, there is no information on particulate absorption properties in the Strait and the proposed classification corresponds to waters away from the Fraser River plume. Surface waters closer to the plume are likely suspended-particulate dominant case 2 waters. Regardless of the dominant optical constituent, the surface waters of the Strait are classified as case 2 waters. For this reason, to accurately estimate *chl* it is important to evaluate and possibly modify algorithms that are based on open-ocean case 1 waters (IOCCG 2000).

In Chapter 2, the empirical OC3M and semi-analytical Garver-Siegel-Maritorena model version 1 (GSM01) were evaluated using ship-based biophysical and radiometric measurements modelled to MODIS Aqua bands. Additionally, a modified version of the GSM01 algorithm was evaluated with a different model for CDOM absorption and a re-interpretation of phytoplankton absorption at 443 nm.

The ship-based radiometric and *chl* measurements showed that the OC3M algorithm could not be indiscriminately used throughout the Strait ($r^2 = 0.345$), due to the influence of turbidity from the Fraser River on the algorithm. When stations in the immediate vicinity of the Fraser River discharge were excluded, the OC3M algorithm was moderately effective with $r^2 = 0.552$.

Similar to the OC3M algorithm, the indiscriminate application of the standard and modified GSM01 algorithm was ineffective at estimating *chl* concentrations with $r^2 = 0.001$ and 0.022, respectively. Although both GSM01 algorithms were not effective at estimating *chl* concentrations, they provided statistically significant estimates of CDOM absorption ($r^2 = 0.584$ and 0.620, respectively) and TSS concentrations ($r^2 = 0.866$ and 0.935, respectively). By limiting *chl* estimates to waters with combined CDOM/particulate absorption lower than 0.8 m^{-1}, which represent waters under the influence of the Fraser River, the modified GSM01 algorithm produced statistically significant *chl* estimates ($r^2 = 0.690$).

Further improvement to the GSM01 *chl* estimates was obtained by re-interpreting phytoplankton absorption coefficients using a two-component phytoplankton model developed by Devred et al. (2006) from Vancouver Island samples. This resulted in an $r^2 = 0.702$ and a slope closer to one. Although the linear relationship improved with the two-component model, the root-mean-squared-error was increased. The reason for this increase is not well understood and may require further investigation of the particle absorption properties in these waters.

In summary, semi-analytical algorithms, such as the GSM01, provide statistically significant *chl* estimates for waters under limited influence of the Fraser River discharge. However, due to the nature of these algorithms, their effectiveness is dependent upon the accurate characterization of the absorption and backscattering properties of the optically significant water constituents, which is not always available. Furthermore, the GSM01 effectiveness is contingent upon the accurate atmospheric correction of the shorter blue wavelengths within satellite imagery. As found with imagery of coastal waters, the overcorrection of the shorter blue wavelengths is a common issue (Bailey and Werdell 2006). This means that the GSM01 effectiveness found in Chapter 2 may not hold when used in conjunction with atmospheric corrected satellite imagery of the Strait. This was investigated in Chapter 3 by evaluating different atmospheric correction methods using *chl* measurements from an unattended fluorometer.

In Chapter 3, the standard near infrared (NIR) correction, a shortwave infrared (SWIR) correction, and a combined SWIR/NIR correction, which was an adaptation of a method developed by Management Unit of the North Sea Mathematical Models (MUMM), were evaluated. To evaluate each of these atmospheric correction methods, the OC3M algorithm and the modified GSM01 algorithm limited to CDOM/particulate absorption less than 0.8 m^{-1} were used.

The standard NIR atmospheric correction was successful under limited circumstances. As expected, under turbid and high *chl* concentration waters the NIR atmospheric correction occasionally failed. Also, an overestimation of *chl* concentrations was found with the OC3M algorithm compared to ferry measurements. This overestimation is likely related to the overcorrection of the blue wavelengths in relation to green because of the NIR reflectance from particulate associated with both the phytoplankton cellular structures and the Fraser River plume. By limiting the evaluations to points outside the immediate vicinity of the Fraser River discharge, the NIR correction with the OC3M algorithm had an adjusted $r^2 = 0.759$, was limited $chl < 21$ mg m^{-3}, and estimated concentrations for 63% of the study pixels. For future study, the bio-optical model used by the iterative NIR correction (Patt et al. 2003) maybe adapted to better represent optical characteristics of suspended particles found at higher *chl* concentrations.

The SWIR atmospheric correction method, implemented in SeaDAS 5.1.3, was not as effective as the NIR correction. The OC3M algorithm estimated *chl* concentrations for a very limited number of pixels (21%), much less than the NIR correction, and the statistical relationship with ferry measurements was not as good as with the NIR correction (adjusted $r^2 = 0.514$).

Using an adapted MUMM correction method, with the spatial characterization of the aerosol properties from the SWIR correction combined with the MUMM correction method, was more effective than the NIR or SWIR correction methods. The MUMM correction with the OC3M algorithm was able to estimate *chl* concentrations over the greatest number of pixels and had a lower root-mean-squared-error compared to the NIR-OC3M combination. While the adapted MUMM method was able to atmospherically correct a greater number of pixels (89%), the OC3M algorithm was not effective in the more turbid regions around the Fraser River. As was found with ship-based measurements, the exclusion of points within 4 km of the shal-

lower portions of the Fraser River discharge improved the statistical relationship with an adjusted $r^2 = 0.702$ and was able to estimate *chl* concentrations for 84% of pixels outside of the Fraser River excluded region.

The adapted MUMM atmospheric correction method has two significant caveats for its general use with Strait of Georgia MODIS imagery. The first caveat is that it is based on the assumption that atmospheric aerosols have limited spatial variability. The second caveat is that the signal-to-noise ratio (SNR) of the SWIR bands on the MODIS Aqua sensor may not be appropriate for accurately estimating aerosol properties in all images. If the Rayleigh corrected reflectance in the SWIR bands is too low, the aerosol properties can be difficult to identify. This difficulty in identifying the aerosol properties and the resulting impact on *chl* estimation was demonstrated with an image of the Strait on August 19, 2006. The OC3M image showed overestimated *chl* concentrations in the central portions of the Strait. This overestimation was possibly related to atmospheric variability between the central and southern portions of the Strait, which was difficult to discern with the lower Rayleigh-corrected reflectance found in the MODIS image.

Although the Fraser River influence on the OC3M algorithm was evaluated with a fixed region around the Fraser River excluded from the analysis, movement of the Fraser River plume from wind and tidal activity may cause the fixed region approach to be ineffective. To improve reliability of the OC3M algorithm, a turbid water algorithm may be used to mask turbid waters from evaluation with the OC3M algorithm. These algorithms may also better identify the limited influence of the Fraser River plume during autumn/winter conditions and identify general turbidity in the central portion of the Strait found in other studies during autumn (Johannessen et al. 2006).

A common issue with the adapted MUMM correction, as well as the NIR and SWIR correction methods, was the overcorrection of the 412 nm reflectance in the

Strait. As the modified GSM01 algorithm is dependent upon the accurate atmospheric correction of the 412 nm band, the algorithm was ineffective with all three atmospheric correction methods. The overcorrection of the 412 nm band is a prevalent issue in atmospherically corrected coastal imagery (Bailey and Werdell 2006) and may be alleviated with a NO_2 correction (Ahmad et al. 2007) or the detection of absorbing aerosols (Nobileau and Antoine 2005, Shi and Wang 2007) possibly discharged from the urbanized Lower Mainland. Future research may study the seasonal variability in absorbing aerosols and NO_2 concentrations in conjunction with ocean-colour imagery of the Strait of Georgia.

In addition to the overcorrection issue with the atmospheric correction methods, results of the *chl* algorithms may be improved by compensating for the bi-directional reflectance distribution function (BRDF) of the water column. As discussed in Chapter 1, remote-sensing reflectance has a angular dependence that is associated with the scattering phase function of the water column. By adjusting to the exact water-leaving radiance (Eq. (1.16)), which has a consistent geometry, the angular dependency can be remove. However, to adjust to exact water-leaving radiance an accurate BRDF that is dependent on the water column inherent optical properties is needed. Future studies may evaluate several different BRDFs identified for both CDOM-dominant and suspended-particulate dominant waters (Loisel and Morel 2001, Morel et al. 2002, Albert and Mobley 2003, Lee et al. 2004, Park and Ruddick 2005).

Furthermore, future studies in the Strait may also look at the use of other MODIS Aqua bands designed for land use that maybe effective in the turbid waters of the Strait. These additional bands in the visible and NIR wavelengths have resolutions of 250 and 500 m and past studies have looked at using them to monitor water quality (Hu et al. 2004, Franz et al. 2006).

As well as identifying directions for future studies, the major contribution of this research was detailed analysis of using freely available MODIS imagery for estimat-

ing *chl* concentrations in the Strait of Georgia. In relation to *chl* algorithms, the OC3M algorithm was identified as being effective at estimating *chl* concentrations in less turbid waters and the use of a semi-analytical algorithm, such as the modified GSM01 algorithm, is more likely effective than the OC3M algorithm given accurate atmospheric correction of the 412 nm band. For atmospheric correction methods, the adapted MUMM correction was shown to be more effective than the standard NIR correction and can be used to provide imagery for distinguishing spatial-temporal *chl* patterns in the Strait of Georgia. The combination of the OC3M algorithm with the adapted MUMM correction can provide accurate images of *chl* concentrations in the surface waters of the Strait.

Bibliography

Ahmad, Z., McClain, C. R., Herman, J. R., Franz, B. A., Kwiatkowska, E. J., Robinson, W. D., Bucsela, E. J., Tzortziou, M., 2007. Atmospheric correction for NO_2 absorption in retrieving water-leaving reflectances from the SeaWiFS and MODIS measurements. Applied Optics 46 (26), 6504–6512.

Albert, A., Mobley, C. D., 2003. An analytical model for subsurface irradiance and remote sensing reflectance in deep and shallow case-2 waters. Optics Express 11 (22), 2873–2890.

Alvain, S., Moulin, C., Dandonneau, Y., Loisel, H., Breon, F. M., 2006. A species-dependent bio-optical model of case I waters for global ocean color processing. Deep-Sea Research Part I-Oceanographic Research Papers 53 (5), 917–925.

Antoine, D., Morel, A., 1999. A multiple scattering algorithm for atmospheric correction of remotely sensed ocean colour (MERIS instrument): principle and implementation for atmospheres carrying various aerosols including absorbing ones. International Journal of Remote Sensing 20 (9), 1875–1916.

Arar, E. J., 1997. Method 447.0. Determination of chlorophylls a and b and identification of other pigments of interest in marine and freshwater algae using High Performance Liquid Chromatography with visible wavelength detection. Tech. rep., National Exposure Laboratory, U.S. Environmental Protection Agency.

Babin, M., Morel, A., Fournier-Sicre, V., Fell, F., Stramski, D., 2003a. Light scatter-

ing properties of marine particles in coastal and open ocean waters as related to the particle mass concentration. Limnology and Oceanography 48 (2), 843–859.

Babin, M., Stramski, D., Ferrari, G. M., Claustre, H., Bricaud, A., Obolensky, G., Hoepffner, N., 2003b. Variations in the light absorption coefficients of phytoplankton, nonalgal particles, and dissolved organic matter in coastal waters around Europe. Journal of Geophysical Research 108 (C7), 3211.

Bailey, S. W., Werdell, P. J., 2006. A multi-sensor approach for the on-orbit validation of ocean color satellite data products. Remote Sensing of Environment 102 (1-2), 12–23.

Baith, K., Lindsay, R., Fu, G., McClain, C. R., 2001. SeaDAS, a data analysis system for ocean-color satellite sensors. EOS Trans. AGU 82, 202.

Bale, A. J., Tocher, M. D., Weaver, R., Hudson, S. J., Aiken, J., 1994. Laboratory measurements of the spectral properties of estuarine suspended particles. Netherlands Journal of Aquatic Ecology 28 (3-4), 237–244.

Bartlett, J. S., Voss, K. J., Sathyendranath, S., Vodacek, A., 1998. Raman scattering by pure water and seawater. Applied Optics 37 (15), 3324–3332.

Behrenfeld, M. J., Falkowski, P. G., 1997. Photosynthetic rates derived from satellite-based chlorophyll concentration. Limnology and Oceanography 42 (1), 1–20.

Blondeau-Patissier, D., Tilstone, G. H., Martinez-Vicente, V., Moore, G. F., 2004. Comparison of bio-physical marine products from SeaWiFS, MODIS and a bio-optical model with in situ measurements from Northern European waters. Journal of Optics A-Pure and Applied Optics 6 (9), 875–889.

Bokoye, A. I., Royer, A., O'Neill, N. T., Cliche, P., Fedosejevs, G., Teillet, P. M., McArthur, L. J. B., 2001. Characterization of atmospheric aerosols across Canada

from a ground-based sunphotometer network: AEROCAN. Atmosphere-Ocean 39 (4), 429–456.

Bowers, D. G., Binding, C. E., 2006. The optical properties of mineral suspended particles: A review and synthesis. Estuarine Coastal and Shelf Science 67 (1-2), 219–230.

Bricaud, A., Morel, A., Babin, M., Allali, K., Claustre, H., 1998. Variations of light absorption by suspended particles with chlorophyll a concentration in oceanic (case 1) waters: Analysis and implications for bio-optical models. Journal of Geophysical Research 103 (C13), 31033–31044.

Bricaud, A., Morel, A., Prieur, L., 1981. Absorption by dissolved organic-matter of the sea (yellow substance) in the UV and visible domains. Limnology and Oceanography 26 (1), 43–53.

Carder, K. L., Chen, F. R., Lee, Z. P., Hawes, S. K., 1999. Semianalytic Moderate-Resolution Imaging Spectrometer algorithms for chlorophyll a and absorption with bio-optical domains based on nitrate-depletion temperatures. Journal of Geophysical Research 104 (C3), 5403–5421.

Carder, K. L., Steward, R. G., Harvey, G. R., Ortner, P. B., 1989. Marine humic and fluvic acids: Their effects on remote sensing of ocean chlorophyll. Limnology and Oceanography 34 (1), 68–81.

Chami, M., 2007. Importance of the polarization in the retrieval of oceanic constituents from the remote sensing reflectance. Journal of Geophysical Research 112 (C5), C05026.

Chami, M., Platel, M. D., 2007. Sensitivity of the retrieval of the inherent optical properties of marine particles in coastal waters to the directional variations and the polarization of the reflectance. Journal of Geophysical Research 112 (C5), C05037.

Clesceri, L. S., Greenberg, A. E., Eaton, A. D., 1998. Standard Methods For The Examination of Water and Wastewater, 20th Edition. APHA,AWWA, WEF, Washington, DC.

Coble, P. G., 2007. Marine optical biogeochemistry: The chemistry of ocean color. Chemical reviews 107 (2), 402–418.

Collins, A., 2005. A 1D ocean mixing model of the Strait of Georgia. Master's thesis, University of British Columbia.

Dall'Olmo, G., Gitelson, A. A., 2006. Effect of bio-optical parameter variability and uncertainties in reflectance measurements on the remote estimation of chlorophyll-a concentration in turbid productive waters: modeling results. Applied Optics 45 (15), 3577–3592.

Darecki, M., Stramski, D., 2004. An evaluation of MODIS and SeaWiFS bio-optical algorithms in the Baltic Sea. Remote Sensing of Environment 89 (3), 326–350.

Darecki, M., Weeks, A., Sagan, S., Kowalczuk, P., Kaczmarek, S., 2003. Optical characteristics of two contrasting case 2 waters and their influence on remote sensing algorithms. Continental Shelf Research 23 (3-4), 237–250.

Defoin-Platel, M., Chami, M., 2007. How ambiguous is the inverse problem of ocean color in coastal waters? Journal of Geophysical Research 112 (C3), C03004.

Devred, E., Sathyendranath, S., Stuart, V., Maass, H., Ulloa, O., Platt, T., 2006. A two-component model of phytoplankton absorption in the open ocean: Theory and applications. Journal of Geophysical Research 111 (C3), C03011.

Doxaran, D., Cherukuru, N., Lavender, S. J., 2006. Apparent and inherent optical properties of turbid estuarine waters: measurements, empirical quantification relationships, and modeling. Applied Optics 45 (10), 2310–2324.

Doxaran, D., Cherukuru, R. C. N., Lavender, S. J., 2005. Use of reflectance band ratios to estimate suspended and dissolved matter concentrations in estuarine waters. International Journal of Remote Sensing 26 (8), 1763–1769.

D'Sa, E. J., Miller, R. L., Castillo, C. D., 2006. Bio-optical properties and ocean color algorithms for coastal waters influenced by the Mississippi River during a cold front. Applied Optics 45 (28), 7410–7428.

Esaias, W. E., Abbott, M. R., Barton, I., Brown, O. B., Campbell, J. W., Carder, K. L., Clark, D. K., Evans, R. H., Hoge, F. E., Gordon, H. R., Balch, W. M., Letelier, R., Minnett, P. J., 1998. An overview of modis capabilities for ocean science observations. IEEE Transactions on Geoscience and Remote Sensing 36 (4), 1250–1265.

Fournier, G., Forand, J. L., 1994. Analytic phase function for ocean water. In: Jaffe, J. S. (Ed.), Ocean Optics XII. Vol. 2258. Proc. SPIE, pp. 194–201.

Franz, B. A., Kwiatkowska, E. J., Meister, G., McClain, C. R., 2007. Utility of MODIS-Terra for ocean color applications. Vol. 6677. SPIE, p. 66770Q.

Franz, B. A., Werdell, P. J., Meister, G., Kwiatkowska, E. J., Bailey, S. W., Ahmad, Z., McClain, C. R., October 9-13 2006. MODIS land bands for ocean remote sensing applications. In: Proc. Ocean Optics XVIII. Montreal, Canada, pp. 1–16.

Gallie, E. A., Murtha, P. A., 1992. Specific absorption and backscattering spectra for suspended minerals and chlorophyll-a in Chilko Lake, British Columbia. Remote Sensing of Environment 39 (2), 103–118.

Gao, B. C., Heidebrecht, K. B., Goetz, A. F. H., 1993. Derivation of scaled surface reflectances from AVIRIS data. Remote Sensing of Environment 44 (2-3), 165–178.

Gao, B. C., Montes, M. J., Ahmad, Z., Davis, C. O., 2000. Atmospheric correction algorithm for hyperspectral remote sensing of ocean color from space. Applied Optics 39 (6), 887–896.

Garcia, C. A. E., Garcia, V. M. T., McClain, C. R., 2005. Evaluation of SeaWiFS chlorophyll algorithms in the Southwestern Atlantic and Southern Oceans. Remote Sensing of Environment 95 (1), 125–137.

Gargett, A. E., 1997. The optimal stability 'window': a mechanism underlying decadal fluctuations in North Pacific salmon stocks? Fisheries Oceanography 6 (2), 109–117.

Gordon, H. R., 1997. Atmospheric correction of ocean color imagery in the Earth Observing System era. Journal of Geophysical Research 102 (D14), 17081–17106.

Gordon, H. R., 2005. Normalized water-leaving radiance: revisiting the influence of surface roughness. Applied Optics 44 (2), 241–248.

Gordon, H. R., Brown, J. W., Evans, R. H., 1988a. Exact Rayleigh scattering calculations for use with the Nimbus-7 Coastal Zone Color Scanner. Applied Optics 27 (5), 862–871.

Gordon, H. R., Brown, O. B., Evans, R. H., Brown, J. W., Smith, R. C., Baker, K. S., Clark, D. K., 1988b. A semianalytic radiance model of ocean color. Journal of Geophysical Research 93 (D9), 10909–10924.

Gordon, H. R., Morel, A. Y., 1983. Remote assessment of ocean color for interpretation of satellite visible imagery: a review. Springer-Verlag, New York.

Gordon, H. R., Wang, M., 1994. Retrieval of water-leaving radiance and aerosol optical thickness over the oceans with SeaWiFS: a preliminary algorithm. Applied Optics 33 (3), 443–452.

Gould, R. W., Arnone, R. A., Martinolich, P. M., 1999. Spectral dependence of the scattering coefficient in case 1 and case 2 waters. Applied Optics 38 (12), 2377–2383.

Gower, J., King, S., Borstad, G., Brown, L., 2005. Detection of intense plankton blooms using the 709 nm band of the MERIS imaging spectrometer. International Journal of Remote Sensing 26 (9), 2005–2012.

Gower, J. F. R., Brown, L., Borstad, G. A., 2004. Observation of chlorophyll fluorescence in west coast waters of Canada using the MODIS satellite sensor. Canadian Journal of Remote Sensing 30 (1), 17–25.

Gower, J. F. R., Doerffer, R., Borstad, G. A., 1999. Interpretation of the 685 nm peak in water-leaving radiance spectra in terms of fluorescence, absorption and scattering, and its observation by MERIS. International Journal of Remote Sensing 20 (9), 1771–1786.

Haigh, R., Taylor, F. J. R., 1991. Mosaicism of microplankton communities in the northern Strait of Georgia, British Columbia. Marine Biology 110 (2), 301–314.

Hale, G. M., Querry, M. R., 1973. Optical constants of water in the 200 nm to 200 μm wavelength region. Applied Optics 39, 3582–3591.

Halverson, M., Pawlowicz, R., Lee, R., 2003. Assessing surface water properties and chlorophyll concentrations with ferry-based instrument.

Harrison, P. J., Clifford, P. J., Cochlan, W. P., Yin, K., Stjohn, M. A., Thompson, P. A., Sibbald, M. J., Albright, L. J., 1991. Nutrient and plankton dynamics in the Fraser River Plume, Strait of Georgia, British Columbia. Marine Ecology Progress Series 70 (3), 291–304.

Harrison, P. J., Fulton, J. D., Taylor, F. J. R., Parsons, T. R., 1983. Review of the biological oceanography of the Strait of Georgia: Pelagic environment. Canadian Journal of Fisheries and Aquatic Sciences 40 (7), 1064–1094.

Hooker, S. B., Morel, A., 2003. Platform and environmental effects on above-water determinations of water-leaving radiances. Journal of Atmospheric and Oceanic Technology 20 (1), 187–205.

Hu, C., Carder, K. L., Muller-Karger, F. E., 2000. Atmospheric correction of SeaWiFS imagery over turbid coastal waters: A practical method. Remote Sensing of Environment 74 (2), 195–206.

Hu, C. M., Chen, Z. Q., Clayton, T. D., Swarzenski, P., Brock, J. C., Muller-Karger, F. E., 2004. Assessment of estuarine water-quality indicators using MODIS medium-resolution bands: Initial results from Tampa Bay, FL. Remote Sensing of Environment 93 (3), 423–441.

IOCCG, 2000. Remote sensing of ocean colour in coastal and other optically complex waters. Tech. Rep. No. 3, International Ocean-Colour Coordinating Group, Dartmouth, Canada.

IOCCG, 2006. Remote sensing of inherent optical properties: Fundamentals, tests of algorithms, and applications. Tech. Rep. No. 5, International Ocean-Colour Coordinating Group, Dartmouth, Canada.

IOCCG, 2007. Ocean-colour data merging. Tech. Rep. No. 6, International Ocean-Colour Coordinating Group, Dartmouth, Canada.

Johannessen, S. C., Macdonald, R. W., Paton, D. W., 2003. A sediment and organic carbon budget for the greater Strait of Georgia. Estuarine, Coastal and Shelf Science 56 (3-4), 845–860.

Johannessen, S. C., Masson, D., Macdonald, R. W., 2006. Distribution and cycling of suspended particles inferred from transmissivity in the Strait of Georgia, Haro Strait and Juan de Fuca Strait. Atmosphere-Ocean 44 (1), 17–27.

Johannessen, S. C., O'Brien, M. C., Denman, K. L., Macdonald, R. W., 2005. Seasonal and spatial variations in the source and transport of sinking particles in the Strait of Georgia, British Columbia, Canada. Marine Geology 216 (1-2), 59–77.

Kirk, J. T. O., 1994. Light and Photosynthesis in Aquatic Ecosystems. Cambridge University Press.

Kostadinov, T. S., Siegel, D. A., Maritorena, S., Guillocheau, N., 2007. Ocean color observations and modeling for an optically complex site: Santa Barbara Channel, California, USA. Journal of Geophysical Research 112 (C07011).

Kostaschuk, R. A., Luternauer, J. L., Church, M. A., 1989. Suspended sediment hysteresis in a salt-wedge estuary: Fraser River, Canada. Marine Geology 87 (2-4), 273–285.

Kostaschuk, R. A., Stephan, B. A., Luternauer, J. L., 1993. Suspended sediment concentration in a buoyant plume: Fraser River, Canada. Geo-Marine Letters 13 (3), 165–171.

Kowalczuk, P., Olszewski, J., Darecki, M., Kaczmarek, S., 2005. Empirical relationships between coloured dissolved organic matter (CDOM) absorption and apparent optical properties in Baltic Sea waters. International Journal of Remote Sensing 26 (2), 345–370.

Lavender, S. J., Pinkerton, M. H., Moore, G. F., Aiken, J., Blondeau-Patissier, D., 2005. Modification to the atmospheric correction of SeaWiFS ocean colour images over turbid waters. Continental Shelf Research 25 (4), 539–555.

LeBlond, P. H., 1983. The Strait of Georgia: functional anatomy of a coastal sea. Canadian Journal of Fisheries and Aquatic Sciences 40 (7), 1033–1063.

Lee, Z., Carder, K. L., Du, K. P., 2004. Effects of molecular and particle scatterings on the model parameter for remote-sensing reflectance. Applied Optics 43 (25), 4957–4964.

Lee, Z. P., Carder, K. L., Arnone, R. A., 2002. Deriving inherent optical properties from water color: a multiband quasi-analytical algorithm for optically deep waters. Applied Optics 41 (27), 5755–5772.

Lee, Z. P., Carder, K. L., Mobley, C. D., Steward, R. G., Patch, J. S., 1999. Hyperspectral remote sensing for shallow waters: 2. deriving bottom depths and water properties by optimization. Applied Optics 38 (18), 3831–3843.

Lee, Z. P., Darecki, M., Carder, K. L., Davis, C. O., Stramski, D., Rhea, W. J., 2005. Diffuse attenuation coefficient of downwelling irradiance: An evaluation of remote sensing methods. Journal of Geophysical Research 110 (C2), C02017.

Li, L. P., Fukushima, H., Frouin, R., Mitchell, B. G., He, M. X., Uno, I., Takamura, T., Ohta, S., 2003a. Influence of submicron absorptive aerosol on sea-viewing wide field-of-view sensor (SeaWiFS)-derived marine reflectance during Aerosol Characterization Experiment (ACE)-Asia. Journal of Geophysical Research 108 (D15), 4472.

Li, M., Gargett, A., Denman, K., 2000. What determines seasonal and interannual variability of phytoplankton and zooplankton in strongly estuarine systems? Application to the semi-enclosed estuary of Strait of Georgia and Juan de Fuca Strait. Estuarine, Coastal and Shelf Science 50 (4), 467–488.

Li, R.-R., Kaufman, Y. J., Gao, B.-C., Davis, C. O., 2003b. Remote sensing of

suspended sediments and shallow coastal waters. IEEE Transactions on Geoscience and Remote Sensing 41 (3), 559–566.

Li, Y., 2003. Atmospheric correction of SeaWiFS imagery for turbid coastal and inland waters: comment. Applied Optics 42 (6), 893–895.

Liedtk, J., Roberts, A., Luternauer, J., 1995. Practical remote sensing of suspended sediment concentration. Photogrammetric Engineering and Remote Sensing 61 (2), 167–175.

Loisel, H., Morel, A., 2001. Non-isotropy of the upward radiance field in typical coastal (case 2) waters. International Journal of Remote Sensing 22 (2-3), 275–295.

Loisel, H., Nicolas, J. M., Sciandra, A., Stramski, D., Poteau, A., 2006. Spectral dependency of optical backscattering by marine particles from satellite remote sensing of the global ocean. Journal of Geophysical Research 111 (C9), C09024.

Loos, E. A., Costa, M. P. F., submitted. Influence of the Fraser River plume on the optical and bio-physical properties of surface waters of the Strait of Georgia, British Columbia, Canada.

Magnuson, A., Harding, L. W., Mallonee, M. E., Adolf, J. E., 2004. Bio-optical model for Chesapeake Bay and the Middle Atlantic Bight. Estuarine Coastal and Shelf Science 61 (3), 403–424.

Mann, K. H., 1993. Physical oceanography, food chains, and fish stocks: a review. ICES Journal of Marine Science 50 (2), 105–119.

Maritorena, S., Siegel, D. A., Peterson, A. R., 2002. Optimization of a semianalytical ocean color model for global-scale applications. Applied Optics 41 (15), 2705–2714.

Martin, S., 2004. An Introduction to Ocean Remote Sensing. Cambridge University Press, United Kingdom.

Masson, D., 2006. Seasonal water mass analysis for the Straits of Juan de Fuca and Georgia. Atmosphere-Ocean 44 (1), 1–15.

Milliman, J. D., 1980. Sedimentation in the Fraser River and its estuary, Southwestern British Columbia (Canada). Estuarine and Coastal Marine Science 10 (6), 609–633.

Mobley, C. D., 1994. Light and Water radiative transfer in natural waters. Academic Press, Inc., San Diego, California.

Mobley, C. D., 1999. Estimation of the remote-sensing reflectance from above-surface measurements. Applied Optics 38 (36), 7442–7455.

Mobley, C. D., Gentili, B., Gordon, H. R., Jin, Z. H., Kattawar, G. W., Morel, A., Reinersman, P., Stamnes, K., Stavn, R. H., 1993. Comparison of numerical-models for computing underwater light fields. Applied Optics 32 (36), 7484–7504.

Mobley, C. D., Sundman, L. K., Boss, E., 2002. Phase function effects on oceanic light fields. Applied Optics 41 (6), 1035–1050.

Morel, A., Antoine, D., Gentili, B., 2002. Bidirectional reflectance of oceanic waters: accounting for Raman emission and varying particle scattering phase function. Applied Optics 41 (30), 6289–6306.

Morel, A., Belanger, S., 2006. Improved detection of turbid waters from ocean color sensors information. Remote Sensing of Environment 102 (3-4), 237–249.

Morel, A., Gentili, B., 1993. Diffuse-reflectance of oceanic waters .2. bidirectional aspects. Applied Optics 32 (33), 6864–6879.

Morel, A., Gentili, B., 1996. Diffuse reflectance of oceanic waters .3. implication of bidirectionality for the remote-sensing problem. Applied Optics 35 (24), 4850–4862.

Morel, A., Gentili, B., Chami, M., Ras, J., 2006. Bio-optical properties of high chlorophyll case 1 waters and of yellow-substance-dominated case 2 waters. Deep-Sea Research Part I-Oceanographic Research Papers 53 (9), 1439–1459.

Morel, A., Maritorena, S., 2001. Bio-optical properties of oceanic waters: A reappraisal. Journal of Geophysical Research 106 (C4), 7163–7180.

Mueller, J. L., 2003. Ocean optics protocols for satellite ocean color sensor validation, Revision 4, Volume IV, Err.1: Inherent optical properties: Instruments, characterizations, field measurements and data analysis protocols. Tech. Rep. NASA/TM-2003-211621/Rev4-Vol.IV (ERRATUM 1), NASA, Goddard Space Flight Center.

Mueller, J. L., Austin, R. W., Morel, A., Fargion, G. S., McClain, C. R., 2003a. Ocean optics protocols for satellite ocean color sensor validation, Revision 4, Volume I: Introduction, background and conventions. Tech. Rep. NASA/TM-2003-21621/Rev4-Vol I, Goddard Space Flight Space Center.

Mueller, J. L., Fargion, G. S., McClain, C. R., Pegau, S., Zaneveld, J. R. V., Mitchell, B. G., Kahru, M., Wieland, J., Stramska, M., 2003b. Ocean optics protocols for satellite ocean color sensor validation, Revision 4, Volume IV: Inherent optical properties: Instruments, characterizations, field measurements and data analysis protocols. Tech. Rep. NASA/TM-2003-211621/Rev4-Vol.IV, NASA, Goddard Space Flight Center.

Mueller, J. L., Morel, A., Frouin, R., Davis, C., Arnone, R., Carder, K., Lee, Z. P., Steward, R. G., Hooker, S., Mobley, C. D., McLean, S., Holben, B., Miller, M., Pietras, C., Knobelspiesse, K. D., Fargion, G. S., Porter, J., Voss, K., 2003c. Ocean optics protocols for satellite ocean color sensor validation, Revision 4, Volume III:

Radiometric measurements and data analysis protocols. Tech. rep., Goddard Space Flight Center NASA.

Muller-Karger, F. E., Varela, R., Thunell, R., Luerssen, R., Hu, C. M., Walsh, J. J., 2005. The importance of continental margins in the global carbon cycle. Geophysical Research Letters 32 (1), L01602.

Nobileau, D., Antoine, D., 2005. Detection of blue-absorbing aerosols using near infrared and visible (ocean color) remote sensing observations. Remote Sensing of Environment 95 (3), 368–387.

O'Reilly, J. E., Maritorena, S., Mitchell, B. G., Siegel, D. A., Carder, K. L., Graver, S. A., Kahru, M., McClain, C., 1998. Ocean color chlorophyll algorithms for SeaWiFS. Journal of Geophysical Research 103 (C11), 24937–24953.

O'Reilly, J. E., Maritorena, S., O'Brien, M. C., Siegel, D. A., Toole, D., Menzies, D., Smith, R. C., Mueller, J. L., Mitchell, B. G., Kahru, M., Chavez, F. P., Strutton, P., Cota, G. F., Hooker, S. B., McClain, C. R., Carder, K. L., Muller-Karger, F., Harding, L., Magnuson, A., Phinney, D., Moore, G. F., Aiken, J., Arrigo, K. R., Letelier, R., Culver, M., 2000. Volume 11, SeaWiFS postlaunch calibration and validation analyses, part 3. Tech. Rep. NASA Technical Memorandum 2000-206892, Volume 11, NASA.

Park, Y. J., Ruddick, K., 2005. Model of remote-sensing reflectance including bidirectional effects for case 1 and case 2 waters. Applied Optics 44 (7), 1236–1249.

Parsons, T. R., Kessler, T. A., 1987. An ecosystem model for the assessment of plankton production in relation to the survival of young fish. Journal of Plankton Research 9 (1), 125–137.

Patt, F. S., Barnes, R. A., Eplee, Robert E., J., Franz, B. A., Feldman, G. C., Bailey, S. W., Gales, J., Werdell, P. J., Wang, M., Frouin, R., Stumpf, R. P., Arnone,

R., Gould, R. W., Martinolich, P. M., Ransibrahmanakul, V., O'Reilly, J. E., Yonder, J. A., 2003. Volume 22, algorithm updates for the fourth SeaWiFS data reprocessing. Tech. Rep. NASA Technical Memorandum 2000-206892, Volume 22, NASA.

Pegau, S., Zaneveld, J. R. V., Mitchell, B. G., Kahru, M., Wieland, J., Stramska, M., 2003. Ocean optics protocols for satellite ocean color sensor validation, Revision 4, Volume IV: Inherent optical properties: Instruments, characterizations, field measurements and data analysis protocols. Tech. Rep. NASA/TM-2003-211621/Rev4-Vol.IV, NASA Goddard Space Flight Space Center.

Pegau, W. S., Gray, D., Zaneveld, J. R. V., 1997. Absorption and attenuation of visible and near-infrared light in water: dependence on temperature and salinity. Applied Optics 36 (24), 6035–6046.

Pernetta, J. C., Milliman, J. D., 1995. Land-ocean interactions in the coastal zone implementation plan. Tech. Rep. No. 33, IGBP, Stockholm.

Petzold, T. J., 1972. Volume scattering functions for selected ocean waters. Tech. Rep. Tech. Rep. SIO 72-78, Scripps Institution of Oceanography, San Diego, Calif.

Pisano, J. T., McKendry, I., Steyn, D. G., Hastie, D. R., 1997. Vertical nitrogen dioxide and ozone concentrations measured from a tethered balloon in the Lower Fraser Valley. Atmospheric Environment 31 (14), 2071–2078.

Pope, R. M., Fry, E. S., 1997. Absorption spectrum (380-700 nm) of pure water .2. integrating cavity measurements. Applied Optics 36 (33), 8710–8723.

Prieur, L., Sathyendranath, S., 1981. An optical classification of coastal and oceanic waters based on the specific spectral absorption curves of phytoplankton pigments, dissolved organic-matter, and other particulate materials. Limnology and Oceanography 26 (4), 671–689.

Radi, T., Pospelova, V., de Vernal, A., Barrie, J. V., 2007. Dinoflagellate cysts as indicators of water quality and productivity in British Columbia estuarine environments. Marine Micropaleontology 62 (4), 269–297.

Ransibrahmanakul, V., Stumpf, R. P., 2006. Correcting ocean colour reflectance for absorbing aerosols. International Journal of Remote Sensing 27 (9-10), 1759–1774.

Ruddick, K. G., Cauwer, V. D., Park, Y. J., Moore, G., 2006. Seaborne measurements of near infrared water-leaving reflectance: The similarity spectrum for turbid waters. Limnology and Oceanography 51 (2), 1167–1179.

Ruddick, K. G., Gons, H. J., Rijkeboer, M., Tilstone, G., 2001. Optical remote sensing of chlorophyll a in case 2 waters by use of an adaptive two-band algorithm with optimal error properties. Applied Optics 40 (21), 3575–3585.

Ruddick, K. G., Ovidio, F., Rijkeboer, M., 2000. Atmospheric correction of SeaWiFS imagery for turbid coastal and inland waters. Applied Optics 39 (6), 897–912.

Sathyendranath, S., Cota, G., Stuart, V., Maass, H., Platt, T., 2001. Remote sensing of phytoplankton pigments: a comparison of empirical and theoretical approaches. International Journal of Remote Sensing 22 (2-3), 249–273.

Sathyendranath, S., Platt, T., 2007. Spectral effects in bio-optical control on the ocean system. Oceanologia 49 (1), 5–39.

Sathyendranath, S., Platt, T., Irwin, B., Horne, E., Borstad, G., Stuart, V., Payzant, L., Maass, H., Kepkey, P., Li, W. K. W., Spry, J., Gower, J., 2004a. A multispectral remote sensing study of coastal waters off Vancouver Island. International Journal of Remote Sensing 25 (5), 893–919.

Sathyendranath, S., Watts, L., Devred, E., Platt, T., Caverhill, C., Maass, H., 2004b.

Discrimination of diatoms from other phytoplankton using ocean-colour data. Marine Ecology Progress Series 272, 59–68.

Schollaert, S. E., Yoder, J. A., O'Reilly, J. E., Westphal, D. L., 2003. Influence of dust and sulfate aerosols on ocean color spectra and chlorophyll a concentrations derived from SeaWiFS off the U. S. east coast. Journal of Geophysical Research 108 (C6), 3191.

Shettle, E. P., Fenn, R. W., 1979. Models for the aerosols of the lower atmosphere and the effects of humidity variations on their optical properties. Tech. rep., Air Force Geophysics Laboratory, Hanscomb AFB, MA.

Shi, W., Wang, M., 2007. Detection of turbid waters and absorbing aerosols for the MODIS ocean color data processing. Remote Sensing of Environment 110 (2), 149–161.

Siegel, D. A., Maritorena, S., Nelson, N. B., Behrenfeld, M. J., McClain, C. R., 2005. Colored dissolved organic matter and its influence on the satellite-based characterization of the ocean biosphere. Geophysical Research Letters 32 (20), L20605.

Siegel, D. A., Wang, M. H., Maritorena, S., Robinson, W., 2000. Atmospheric correction of satellite ocean color imagery: the black pixel assumption. Applied Optics 39 (21), 3582–3591.

Smith, R. C., Baker, K. S., 1981. Optical-properties of the clearest natural-waters (200-800 nm). Applied Optics 20 (2), 177–184.

Stamnes, K., Li, W., Eide, H., Stamnes, J. J., 2005. Challenges in atmospheric correction of satellite imagery. Optical Engineering 44 (4), 041003.

Stramski, D., Boss, E., Bogucki, D., Voss, K. J., 2004. The role of seawater constituents in light backscattering in the ocean. Progress in Oceanography 61 (1), 27–56.

Stramski, D., Woźniak, S. B., 2005. On the role of colloidal particles in light scattering in the ocean. Limnology and Oceanography 50 (5), 1581–1591.

Stuart, V., Sathyendranath, S., Platt, T., Maass, H., Irwin, B. D., 1998. Pigments and species composition of natural phytoplankton populations: effect on the absorption spectra. Journal of Plankton Research 20 (2), 187–217.

Stumpf, R. P., 2001. Applications of satellite ocean color sensors for monitoring and predicting harmful algal blooms. Human and Ecological Risk Assessment 7 (5), 1363–1368.

Sullivan, J. M., Twardowski, M. S., Zaneveld, J. R. V., Moore, C. M., Barnard, A. H., Donaghay, P. L., Rhoades, B., 2006. Hyperspectral temperature and salt dependencies of absorption by water and heavy water in the 400-750 nm spectral range. Applied Optics 45 (21), 5294–5309.

Thuillier, G., Herse, M., Labs, D., Foujols, T., Peetermans, W., Gillotay, D., Simon, P. C., Mandel, H., 2003. The solar spectral irradiance from 200 to 2400 nm as measured by the SOLSPEC spectrometer from the ATLAS and EURECA missions. Solar Physics 214 (1), 1–22.

Tilstone, G. H., Smyth, T. J., Gowen, R. J., Martinez-Vicente, V., Groom, S. B., 2005. Inherent optical properties of the Irish Sea and their effect on satellite primary production algorithms. Journal of Plankton Research 27 (11), 1127–1148.

Twardowski, M. S., Boss, E., Sullivan, J. M., Donaghay, P. L., 2004. Modeling the spectral shape of absorption by chromophoric dissolved organic matter. Marine Chemistry 89 (1-4), 69–88.

Twardowski, M. S., Donaghay, P. L., 2001. Separating in situ and terrigenous sources of absorption by dissolved materials in coastal waters. Journal of Geophysical Research 106 (C2), 2545–2560.

Ulloa, O., Sathyendranath, S., Platt, T., 1994. Effect of the particle-size distribution on the backscattering ratio in seawater. Applied Optics 33 (30), 7070–7077.

van der Woerd, H., Pasterkamp, R., 2004. Mapping of the North Sea turbid coastal waters using SeaWiFS data. Canadian Journal of Remote Sensing 30 (1), 44–53.

Voss, K. J., Morel, A., 2005. Bidirectional reflectance function for oceanic waters with varying chlorophyll concentrations: Measurements versus predictions. Limnology and Oceanography 50 (2), 698–705.

Waldichuk, M., 1983. Pollution in the Strait of Georgia: a review. Canadian Journal of Fisheries and Aquatic Sciences 40 (7), 1142–1167.

Wang, M. H., 2004. Extrapolation of the aerosol reflectance from the near-infrared to the visible: the single-scattering epsilon vs multiple-scattering epsilon method. International Journal of Remote Sensing 25 (18), 3637–3650.

Wang, M. H., 2005. A refinement for the Rayleigh radiance computation with variation of the atmospheric pressure. International Journal of Remote Sensing 26 (24), 5651–5663.

Wang, M. H., 2006a. Aerosol polarization effects on atmospheric correction and aerosol retrievals in ocean color remote sensing. Applied Optics 45 (35), 8951–8963.

Wang, M. H., 2006b. Effects of ocean surface reflectance variation with solar elevation on normalized water-leaving radiance. Applied Optics 45 (17), 4122–4128.

Wang, M. H., 2007. Remote sensing of the ocean contributions from ultraviolet to near-infrared using the shortwave infrared bands: simulations. Applied Optics 46 (9), 1535–1547.

Wang, M. H., Gordon, H. R., 1994. A simple, moderately accurate, atmospheric correction algorithm for SeaWiFS. Remote Sensing of Environment 50 (3), 231–239.

Wang, M. H., Knobelspiesse, K. D., McClain, C. R., 2005. Study of the Sea-Viewing Wide Field-of-View Sensor (SeaWiFS) aerosol optical property data over ocean in combination with the ocean color products. Journal of Geophysical Research 110 (D10), D10S06.

Wang, M. H., Shi, W., 2005. Estimation of ocean contribution at the MODIS near-infrared wavelengths along the east coast of the US: Two case studies. Geophysical Research Letters 32 (13), L13606.

Wang, M. H., Tang, J. W., Shi, W., 2007. MODIS-derived ocean color products along the China east coastal region. Geophysical Research Letters 34 (6), L06611.

Warrick, J. A., Mertes, L. A. K., Siegel, D. A., Mackenzie, C., 2004. Estimating suspended sediment concentrations in turbid coastal waters of the Santa Barbara Channel with SeaWiFS. International Journal of Remote Sensing 25 (10), 1995–2002.

Whitmore, A. L., Boss, E., Cowles, T. J., Pegau, W. S., 2007. Spectral variability of the particulate backscattering ratio. Optics Express 15 (11), 7019–7031.

Woźniak, S. B., Stramski, D., 2004. Modeling the optical properties of mineral particles suspended in seawater and their influence on ocean reflectance and chlorophyll estimation from remote sensing algorithms. Applied Optics 43 (17), 3489–3503.

Yang, H. Y., Gordon, H. R., 1997. Remote sensing of ocean color: assessment of water-leaving radiance bidirectional effects on atmospheric diffuse transmittance. Applied Optics 36 (30), 7887–7897.

Yin, K., 1997. Importance of wind and river discharge in influencing nutrient dynamics and phytoplankton production in summer in the central Strait of Georgia. Marine Ecology Progress Series 161, 173–183.

Yin, K., Harrison, P. J., Goldblatt, R. H., St. John, M. A., Beamish, R. J., 1997. Factors controlling the timing of the spring bloom in the Strait of Georgia estuary, British Columbia, Canada. Canadian Journal of Fisheries and Aquatic Sciences 54 (9), 1985–1995.

Zhang, X. D., Lewis, M., Johnson, B., 1998. Influence of bubbles on scattering of light in the ocean. Applied Optics 37 (27), 6525–6536.

Zibordi, G., Mélin, F., Berthon, J. F., 2006. Comparison of SeaWiFS, MODIS and MERIS radiometric products at a coastal site. Geophysical Research Letters 33 (6), L06617.

Appendix A

Moderate Resolution Imaging Spectroradiometer (MODIS) Aqua

The Moderate Resolution Imaging Spectroradiometer (MODIS) is a multi-spectral Earth imaging sensor with 36 spectral bands ranging from 0.4 to 14.4 μm. The first MODIS sensor was launched with NASA's Terra satellite and has been operating since December 1999. In addition to the Terra satellite, a second MODIS sensor was launched with NASA's Aqua satellite and has been operating since May 2002. Although both MODIS sensors have ocean-colour bands, the MODIS Aqua sensor is currently the main platform for ocean-colour imagery because of radiometric calibration and stability issues with the MODIS Terra sensor (Franz et al. 2007). The MODIS Aqua sensor continues and expands on the heritage of the Coastal Zone Color Scanner (CZCS) and Sea-viewing Wide Field-of-view Sensor (SeaWiFS) by providing improve signal-to-noise ratios for the ocean-colour bands and improve placement of band centres (Esaias et al. 1998). Although the MODIS Aqua has 9 ocean-colour bands with 1 km resolution at nadir, the sensor also has additional bands at 500 and 250 m resolution that were original designed for land and atmospheric remote sensing. An expanded list of bands used with MODIS high resolution (HIRES) ocean-colour processing is provided in the table below (Franz et al. 2006).

Table A.1: Expanded list of MODIS bands used for high resolution (HIRES) ocean-colour image processing (Franz et al. 2006).

Band Number	Wavelength (nm)	Spatial Resolution (m)	Notes
8	412	1000	Standard ocean-colour band
9	443	1000	Standard ocean-colour band
3	469	500	
10	488	1000	Standard ocean-colour band
11	531	1000	Standard ocean-colour band
12	551	1000	Standard ocean-colour band
4	555	500	
1	645	250	
13	667	1000	Standard ocean-colour band
14	678	1000	Standard ocean-colour band
15	748	1000	Standard ocean-colour band
2	859	250	
16	869	1000	Standard ocean-colour band
5	1240	500	
6	1640	500	Not functional on MODIS Aqua
7	2130	500	

Appendix B

Ship Measured Stations

Station	Latitude	Longitude
S1	48.91667	123.25417
S1-1	48.96667	123.21667
S1-2	48.95500	123.26833
S2-1	48.98000	123.48750
S2-2	49.02500	123.42500
S2-3	49.08333	123.35000
S2-4	49.05000	123.51667
S2-5	49.06667	123.43333
S3	49.12500	123.55833
S3-1	49.15000	123.43333
S3-2	49.20000	123.30833
S3-3	49.16667	123.50000
S4-1	49.25000	123.74833
S4-2	49.23333	123.58333
S4-3	49.25000	123.38333
S4-4	49.26667	123.66667
S4-5	49.26667	123.50000
S5	49.35833	123.85000
S5-1	49.36117	123.69033
S5-2	49.42417	124.03333
S5-3	49.55000	124.10000
S5-4	49.41667	123.90000
S6	49.40333	124.33633
S6-1	49.50000	124.50000
S6-2	49.63667	124.64583
S6-3	49.58333	124.50000
S6-4	49.43333	124.43333

Appendix C

Remote-Sensing Reflectance Measurements

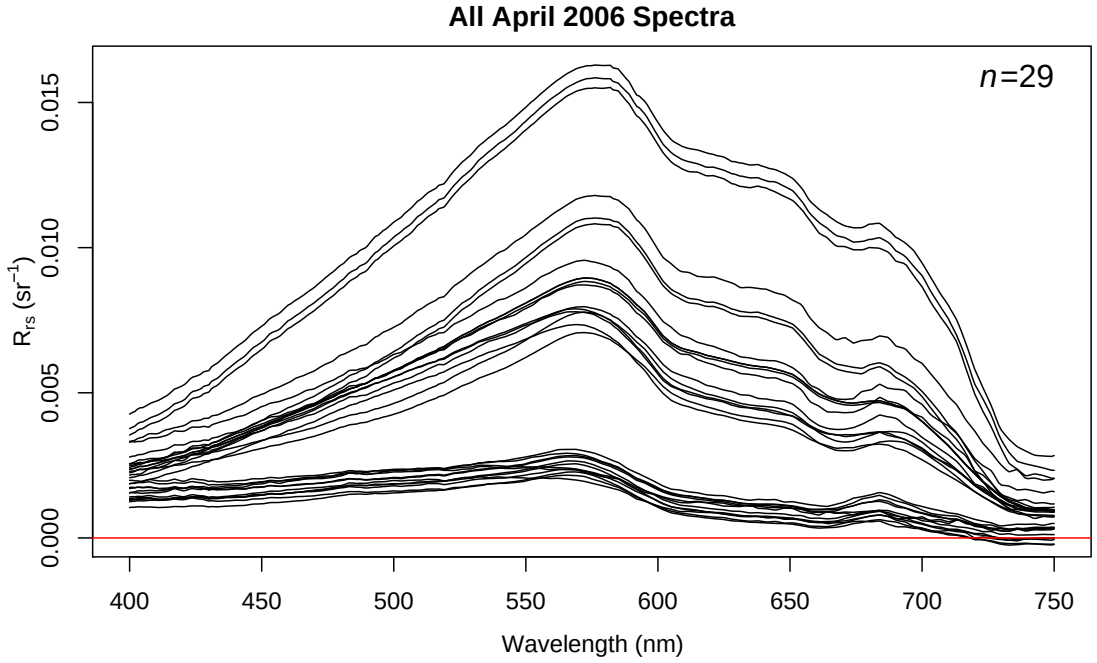
All April 2006 Spectra
n=29
0.000
0.005
0.010
0.015
R_rs (sr^-1)
400
450
500
550
600
650
700
750
Wavelength (nm)

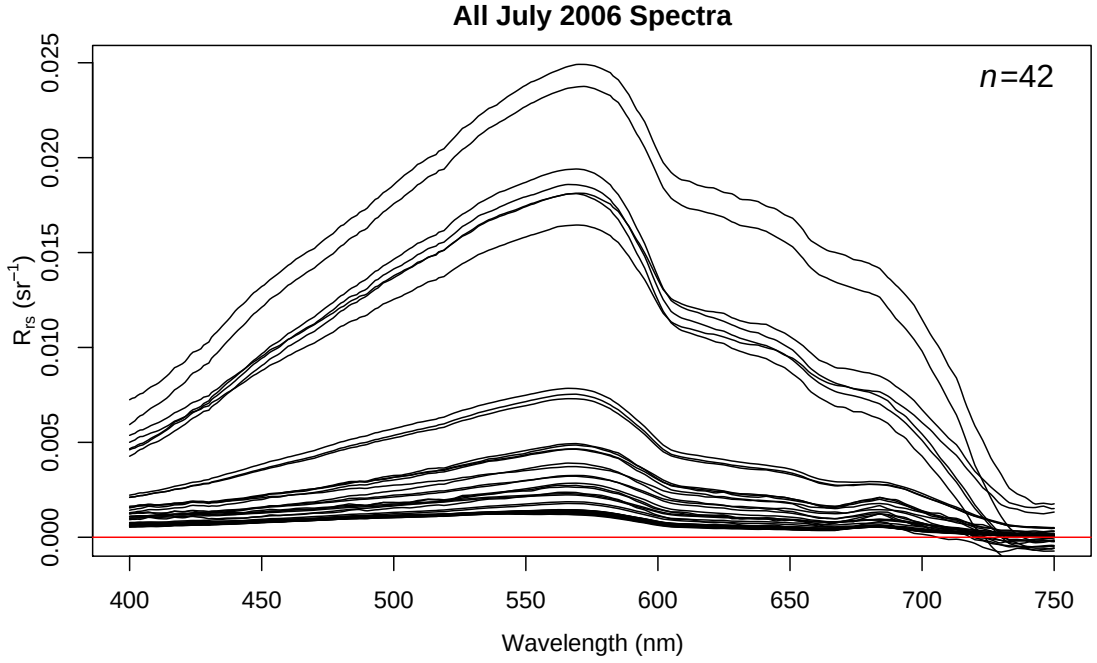
All July 2006 Spectra
n=42
0.000
0.005
0.010
0.015
0.020
0.025
R_rs (sr^-1)
400
450
500
550
600
650
700
750
Wavelength (nm)

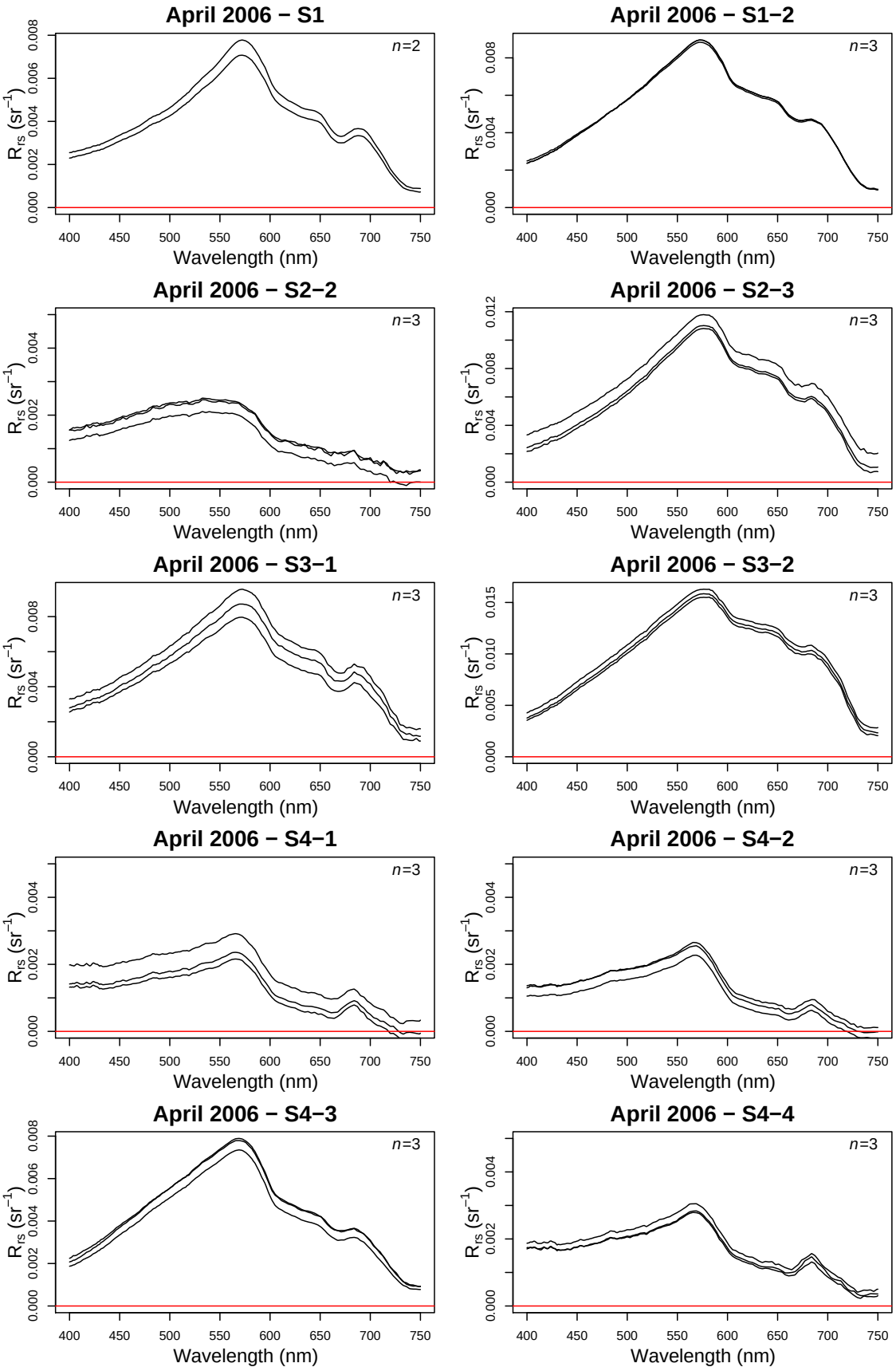
April 2006 − S1
n=2
April 2006 − S1−2
n=3
April 2006 − S2−2
n=3
April 2006 − S2−3
n=3
April 2006 − S3−1
n=3
April 2006 − S3−2
n=3
April 2006 − S4−1
n=3
April 2006 − S4−2
n=3
April 2006 − S4−3
n=3
April 2006 − S4−4
n=3
R_rs (sr^−1)
Wavelength (nm)

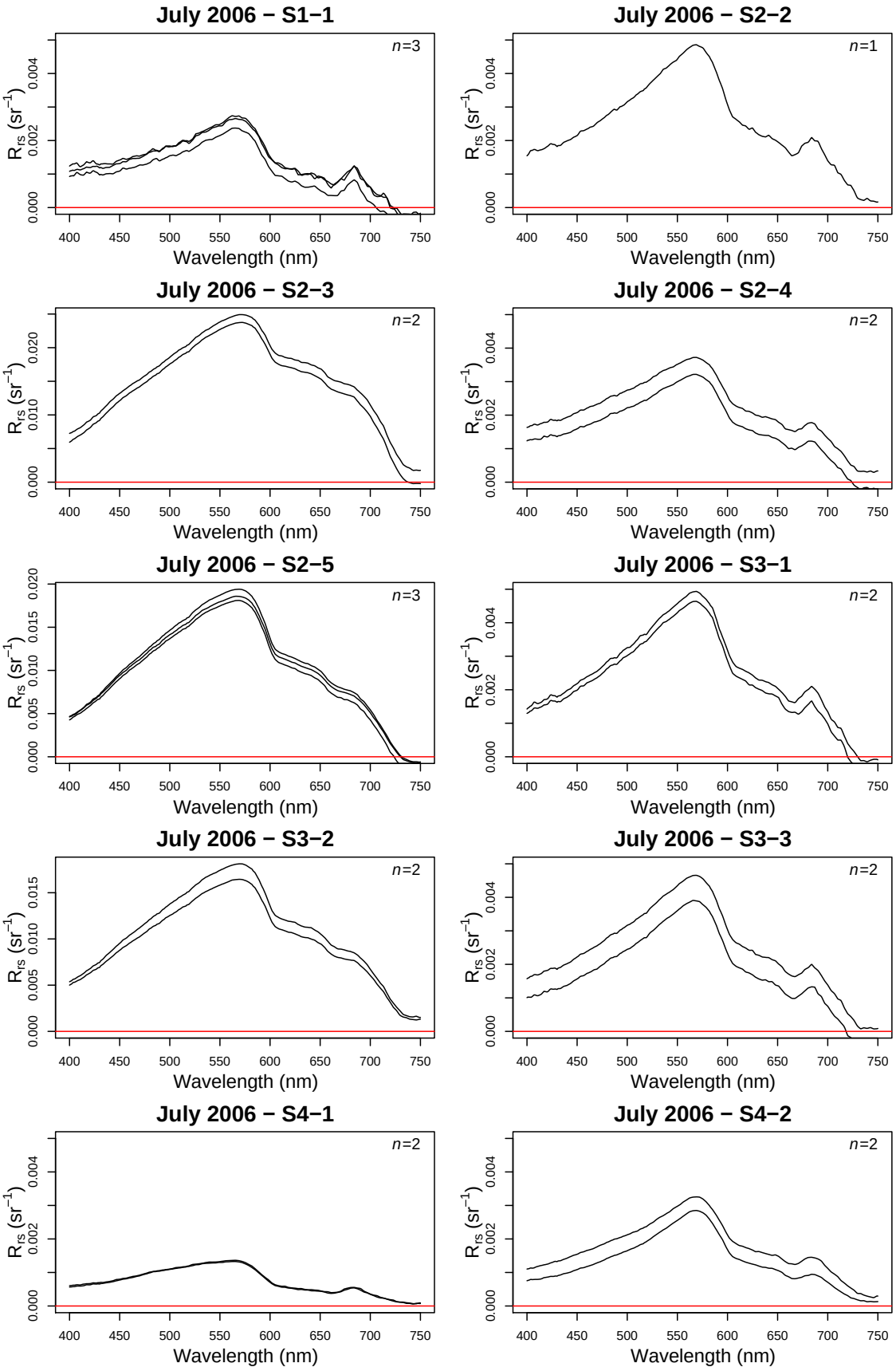
July 2006 − S1−1
n=3
July 2006 − S2−2
n=1
July 2006 − S2−3
n=2
July 2006 − S2−4
n=2
July 2006 − S2−5
n=3
July 2006 − S3−1
n=2
July 2006 − S3−2
n=2
July 2006 − S3−3
n=2
July 2006 − S4−1
n=2
July 2006 − S4−2
n=2
Rrs (sr−1)
Wavelength (nm)

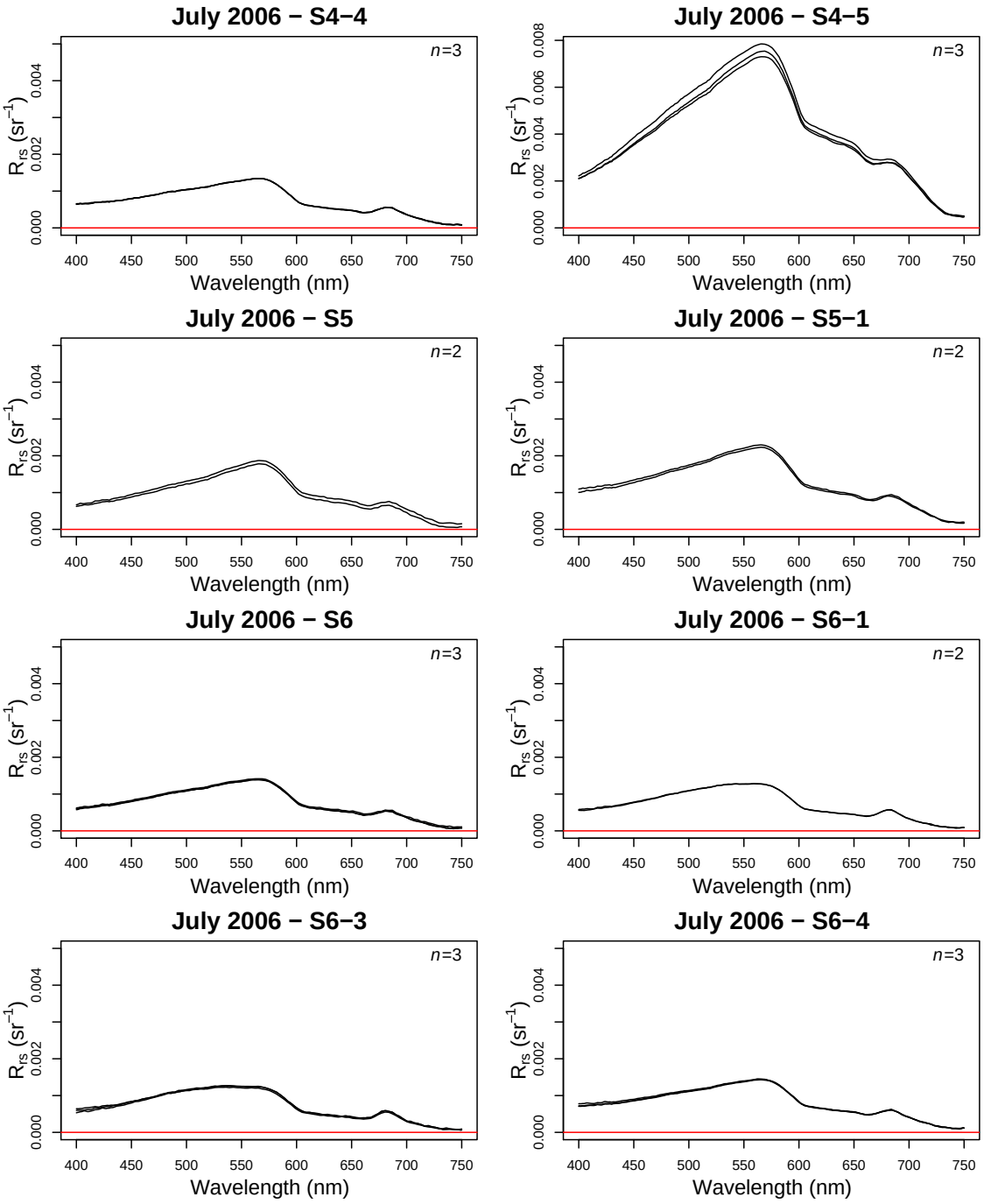
July 2006 − S4−4
n=3
July 2006 − S4−5
n=3
July 2006 − S5
n=2
July 2006 − S5−1
n=2
July 2006 − S6
n=3
July 2006 − S6−1
n=2
July 2006 − S6−3
n=3
July 2006 − S6−4
n=3
R_rs (sr^−1)
Wavelength (nm)
400 450 500 550 600 650 700 750
0.000 0.002 0.004 0.006 0.008

Appendix D

Chromophoric Dissolved Organic Matter Measurements

Date (YYYYMMDD)	**Station**	$a_{cdom}(443)$ (m^{-1})			**Mean** (m^{-1})	**Std.** (m^{-1})
		1	**2**	**3**		
20060425	S1-1	0.4111	NA	NA	NA	NA
20060425	S1-2	0.6535	NA	NA	NA	NA
20060425	S1	0.4595	NA	NA	NA	NA
20060425	blank1	0.0461	NA	NA	NA	NA
20060426	S2-3	0.7823	NA	NA	NA	NA
20060426	S2-2	0.3424	0.3202	0.2903	0.3176	0.0261
20060426	S2-1	0.2994	NA	NA	NA	NA
20060426	blank2	0.0865	0.1235	0.0264	0.0788	0.0490
20060427	S3	0.1944	NA	NA	NA	NA
20060427	S3-1	0.3636	NA	NA	NA	NA
20060427	S3-2	0.7845	0.7313	0.5448	0.6869	0.1259
20060427	blank3	0.0472	0.0661	0.0049	0.0394	0.0313
20060428	S4-3	0.3783	NA	NA	NA	NA
20060428	S4-2	0.2156	NA	NA	NA	NA
20060428	S4-1	0.2511	0.1937	0.1839	0.2095	0.0363
20060428	blank4	0.0423	0.0978	0.1174	0.0858	0.0390

Date	**Station**	$a_{cdom}(443)$ (m^{-1})
20060712	S1-1	0.4012
20060712	S1-2	0.3845
20060712	S1	0.3146
20060712	blank0712	0.0253
20060713	S2-5	0.3048
20060713	S2-4	0.3767
20060713	S2-3	0.3149
20060713	S2-2	0.2865
20060713	S2-1	0.2676
20060713	blank0713	0.0272
20060714	S3	0.3899
20060714	S3-1	0.3512
20060714	S3-2	0.3255
20060714	S3-3	0.3015
20060714	blank0714	0.0621
20060715	S4-5	0.3057
20060715	S4-4	0.2941
20060715	S4-3	0.3567
20060715	S4-2	0.3230
20060715	S4-1	0.2202
20060715	blank0715	0.0211
20060716	S6	0.3700
20060716	S6-1	0.2545
20060716	S6-2	0.2628
20060716	S6-3	0.2362
20060716	S6-4	0.3383
20060716	blank0716	0.0275
20060717	S5	0.4019
20060717	S5-1	0.2792
20060717	S5-2	0.4035
20060717	S5-3	0.4658
20060717	S5-4	0.3593
20060717	blank0717	0.0329

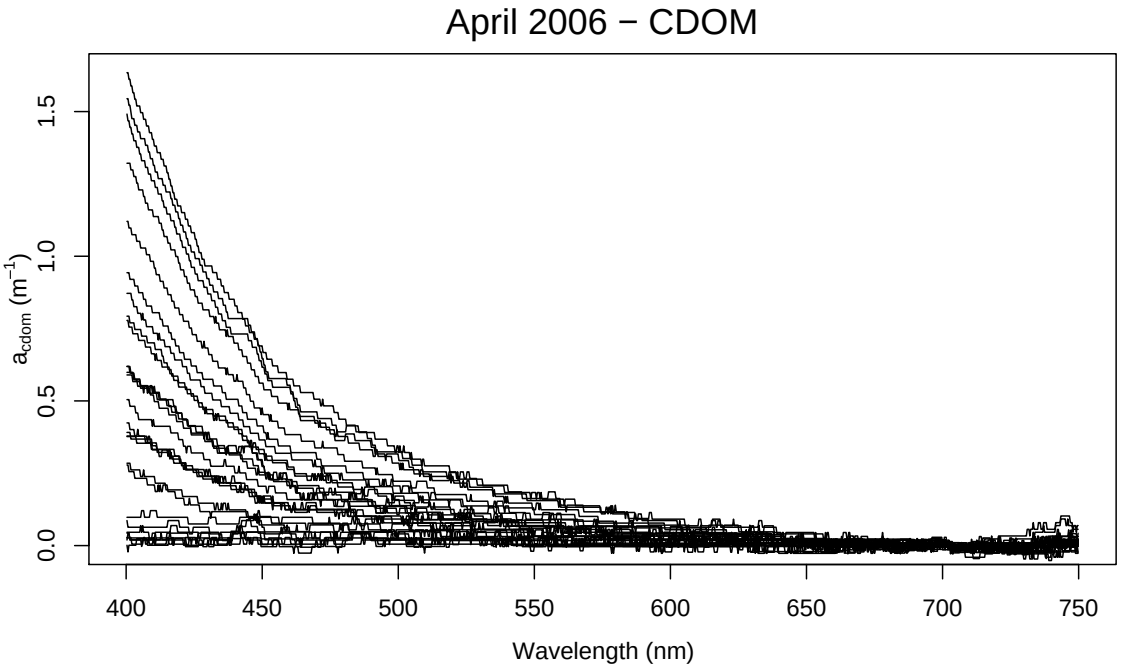

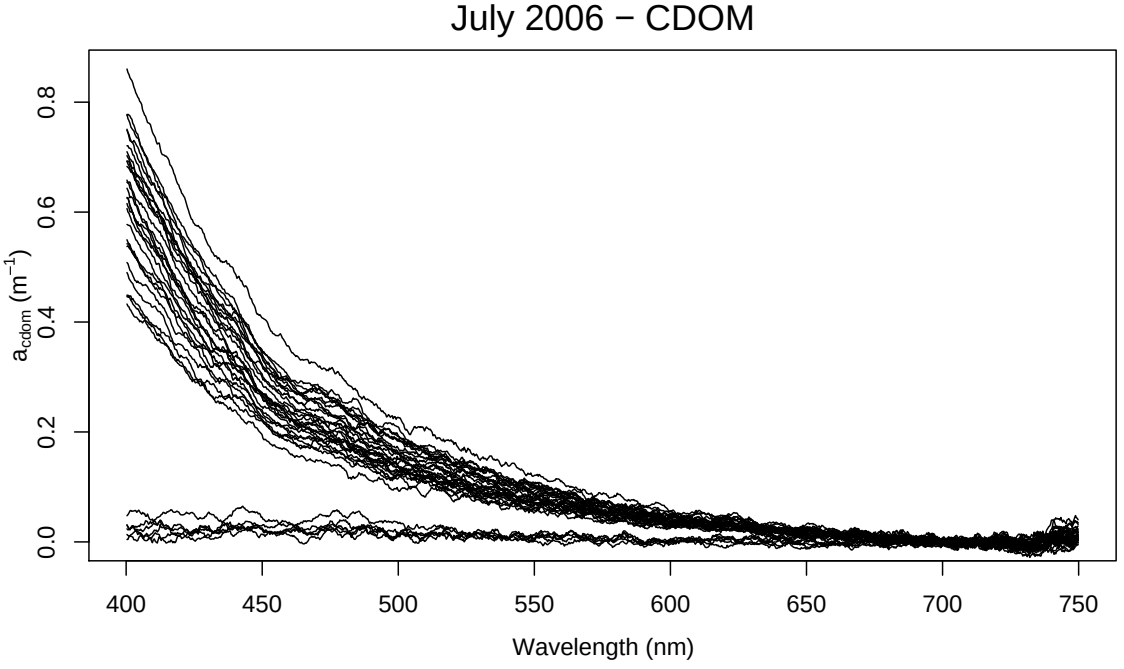

Note: The blank samples are also plotted and are represented by the spectra with the lowest absorption ∼400 nm

Appendix E

Chlorophyll-a Measurements

Date (YYYYMMDD)	**Station**	**Sample** (mg m^{-3})			**Mean** (mg m^{-3})	**Std.** (mg m^{-3})	**Vol.** (l)
		1	**2**	**3**			
20060425	S1-1	3.55	5.19	3.53	4.09	0.95	1.0
20060425	S1-2	3.10	5.11	3.59	3.93	1.05	1.0
20060425	S1	5.13	NA	NA	NA	NA	1.0
20060425	Blank0425	0.00	0.00	0.00	0.00	0.00	2.0
20060426	S2-3	2.16	NA	NA	NA	NA	1.0
20060426	S2-2	0.36	0.35	0.39	0.37	0.02	2.5
20060426	S2-2 (Cast 2)	0.76	0.72	0.71	0.73	0.03	2.5
20060426	S2-1	0.58	NA	NA	NA	NA	3.0
20060426	Blank0426	0.00	0.00	0.00	0.00	0.00	2.0
20060427	S3	0.65	NA	NA	NA	NA	3.0
20060427	S3-1	1.83	NA	NA	NA	NA	3.0
20060427	S3-2	3.74	1.64	4.53	3.30	1.49	1.0
20060427	S3-2 (Cast 2)	6.64	2.24	8.39	5.76	3.17	1.0
20060427	Blank0427	0.00	0.00	0.00	0.00	0.00	2.0
20060428	S4-3	1.45	NA	NA	NA	NA	1.0
20060428	S4-2	2.86	NA	NA	NA	NA	1.0
20060428	S4-1	2.50	0.82	1.43	1.58	0.85	1.0
20060428	S4-4	2.08	NA	NA	NA	NA	1.0
20060428	Blank0428	0.00	0.00	0.00	0.00	0.00	2.0

Date (YYYYMMDD)	**Station**	**Sample** (mg m^{-3}) **1**	**2**	**3**	**Mean** (mg m^{-3})	**Std.** (mg m^{-3})	**Vol.** (l)
20060712	S1-1	3.94	6.20	5.06	5.07	1.13	1.0
20060712	S1-2	5.11	4.59	5.90	5.20	0.66	1.0
20060712	S1	2.96	NA	NA	NA	NA	1.0
20060712	S1 (Lab Dup.)	2.95	NA	NA	NA	NA	1.0
20060712	Blank0712	0.00	0.00	0.00	0.00	0.00	2.0
20060713	S2-1	2.34	NA	NA	NA	NA	1.0
20060713	S2-2	8.46	NA	NA	NA	NA	1.0
20060713	S2-3	0.32	0.49	0.37	0.39	0.09	1.0
20060713	S2-4	6.87	NA	NA	NA	NA	1.0
20060713	S2-5	4.36	NA	NA	NA	NA	1.0
20060713	Blank0713	0.00	0.00	0.00	0.00	0.00	1.0
20060714	S3	5.02	5.31	9.01	6.45	2.22	1.0
20060714	S3-1	6.17	NA	NA	NA	NA	1.0
20060714	S3-2	1.31	NA	NA	NA	NA	1.0
20060714	S3-2 (Lab Dup.)	1.30	NA	NA	NA	NA	1.0
20060714	S3-3	6.03	NA	NA	NA	NA	1.0
20060714	Blank0714	0.00	0.00	0.00	0.00	0.00	2.0
20060715	S4-1	2.53	NA	NA	NA	NA	1.0
20060715	S4-2	6.46	NA	NA	NA	NA	1.0
20060715	S4-3	1.13	NA	NA	NA	NA	1.0
20060715	S4-4	1.93	NA	NA	NA	NA	1.0
20060715	S4-5	3.44	NA	NA	NA	NA	1.0
20060715	Blank0715	0.00	0.00	0.00	0.00	0.00	2.0
20060716	S6	1.98	NA	NA	NA	NA	1.0
20060716	S6-1	1.01	NA	NA	NA	NA	1.0
20060716	S6-2	1.85	NA	NA	NA	NA	2.0
20060716	S6-3	1.49	NA	NA	NA	NA	2.0
20060716	S6-4	2.22	1.73	2.58	2.18	0.43	1.0
20060716	Blank0716	0.00	0.00	0.00	0.00	0.00	2.0
20060717	S5	2.92	NA	NA	NA	NA	1.0
20060717	S5-1	4.67	NA	NA	NA	NA	1.0
20060717	S5-2	3.44	NA	NA	NA	NA	1.0
20060717	S5-3	3.44	NA	NA	NA	NA	1.0
20060717	S5-3 (Lab Dup.)	3.47	NA	NA	NA	NA	1.0
20060717	S5-4	3.18	2.37	3.08	2.88	0.44	1.0
20060717	Blank0717	0.00	0.00	0.00	0.00	0.00	1.0

Appendix F

Total Suspended Solids Measurements

Date (YYYYMMDD)	**Station**	**Sample** (g m^{-3})			**Mean** (g m^{-3})	**Std.** (g m^{-3})	**Vol.** (l)
		1	**2**	**3**			
20060425	S1	5.78	NA	NA	NA	NA	1.0
20060425	S1-1	3.95	NA	NA	NA	NA	1.0
20060425	S1-2	5.33	5.88	5.23	5.48	0.35	1.0
20060425	S1-2 (Cast 2)	6.08	5.49	5.24	5.60	0.43	1.0
20060425	Blank0425	0.04	0.08	0.06	0.06	0.02	2.0
20060426	S2-1	1.14	NA	NA	NA	NA	3.0
20062426	S2-2	5.55	1.15	1.24	2.65	2.51	3.0
20060426	S2-3	7.57	NA	NA	NA	NA	1.0
20060426	Blank0426	0.05	0.08	0.10	0.08	0.03	2.0
20060427	S3-1	4.30	NA	NA	NA	NA	1.9
20060427	S3-2	12.21	11.93	11.52	11.88	0.35	1.0
20060427	S3	1.49	NA	NA	NA	NA	3.0
20060427	Blank0427	0.07	0.07	0.07	0.07	0.00	2.0
20060428	S4-1	3.19	2.41	2.40	2.67	0.45	1.0
20060428	S4-2	3.30	NA	NA	NA	NA	1.0
20060428	S4-3	3.46	NA	NA	NA	NA	1.0
20060428	S4-4	3.47	NA	NA	NA	NA	1.0
20060428	Blank0428	0.08	0.02	0.09	0.06	0.04	2.0

Date (YYYYMMDD)	**Station**	**Sample** (g m^{-3})			**Mean** (g m^{-3})	**Std.** (g m^{-3})	**Vol.** (l)
		1	**2**	**3**			
20060712	S1-1	2.44	1.24	0.91	1.53	0.80	1.0
20060712	S1-2	2.43	2.10	1.60	2.04	0.42	1.0
20060712	S1	2.01	NA	NA	NA	NA	1.0
20060712	Blank0712	0.15	0.10	0.11	0.12	0.03	2.0
20060713	S2-1	2.49	NA	NA	NA	NA	1.0
20060713	S2-2	2.79	NA	NA	NA	NA	1.0
20060713	S2-3	4.34	20.76	20.61	15.24	9.44	1.0
20060713	S2-4	2.83	NA	NA	NA	NA	1.0
20060713	S2-5	5.98	NA	NA	NA	NA	1.0
20060713	Blank0713	0.26	0.11	0.12	0.17	0.08	2.0
20060714	S3	3.73	3.82	4.11	3.89	0.20	1.0
20060714	S3-1	3.22	NA	NA	NA	NA	1.0
20060714	S3-2	6.72	NA	NA	NA	NA	1.0
20060714	S3-3	2.75	NA	NA	NA	NA	1.0
20060714	Blank0714	0.13	0.17	0.16	0.15	0.02	2.0
20060715	S4-1	3.04	NA	NA	NA	NA	1.0
20060715	S4-2	2.87	NA	NA	NA	NA	1.0
20060715	S4-3	1.55	NA	NA	NA	NA	2.0
20060715	S4-4	1.76	NA	NA	NA	NA	2.0
20060715	S4-5	3.06	NA	NA	NA	NA	1.0
20060715	Blank0715	0.14	0.10	0.14	0.13	0.02	2.0
20060716	S6	2.90	NA	NA	NA	NA	1.0
20060716	S6-1	2.50	NA	NA	NA	NA	1.0
20060716	S6-2	1.78	NA	NA	NA	NA	2.0
20060716	S6-3	2.74	NA	NA	NA	NA	2.0
20060716	S6-4	2.44	2.33	3.06	2.61	0.39	1.0
20060716	Blank0716	0.13	0.18	0.17	0.16	0.02	2.0
20060717	S5	2.50	NA	NA	NA	NA	1.0
20060717	S5-1	2.84	NA	NA	NA	NA	1.0
20060717	S5-2	14.17	NA	NA	NA	NA	1.0
20060717	S5-3	2.77	NA	NA	NA	NA	1.0
20060717	S5-4	2.17	1.66	2.42	2.08	0.39	1.0
20060717	Blank0717	0.12	0.16	0.15	0.15	0.02	2.0

University of Victoria

Partial Copyright License

Title of Thesis: Remote Sensing Chlorophyll-a in the Strait of Georgia.

Author: _____

Nicholas M. Komick

December 10, 2007